AN ABSTRACT OF THE DISSERTATION OF

Nicole J. Hams for the degree of Doctor of Philosophy in Biochemistry and Biophysics presented on November 30, 2017

Title: Single-molecule *in vitro* Characterization of Otoferlin

Abstract Approved:

Colin P. Johnson

Congenital hearing loss is a common disorder and over 60 mutations in the sensory hair cell protein, otoferlin, have been linked to pre-lingual deafness. Although otoferlin is essential for hearing, the large size and low solubility of the protein have limited approaches to study its function on a molecular-level. To overcome these challenges, we have developed single-molecule fluorescence assays which have allowed us to quantitatively probe otoferlin function. Based upon our findings, we have shown that otoferlin acts as a calcium-sensitive scaffold for other membrane-fusion proteins at the plasma membrane. The ability to localize fusion proteins at the site of calcium-influx would reduce synaptic delay and allow for rapid neurotransmitter release in response to a sound stimulus. Second, we have directly shown that otoferlin inserts into lipid-bilayers. This finding is significant because insertion into the membrane bilayer has been demonstrated to be a crucial step for mediating the fusion of synaptic vesicles to the plasma membrane.

©Copyright by Nicole J. Hams
November 30, 2017
All Rights Reserved

Single-molecule *in vitro* Characterization of Otoferlin

by
Nicole J. Hams

A DISSERTATION

submitted to

Oregon State University

in partial fulfillment of
the requirement for the
degree of

Doctor of Philosophy

Presented November 30, 2017
Commencement June 2018

Doctor of Philosophy dissertation of Nicole J. Hams presented on November 30, 2017.

APPROVED:

Major, Professor, representing Biochemistry and Biophysics

Chair of the Department of Biochemistry and Biophysics

Dean of the Graduate School

I understand that my dissertation will become part of the permanent collection of Oregon State University libraries. My signature below authorizes release of my dissertation to any reader upon request.

Nicole J. Hams, Author

ACKNOWLEDMENTS

First and foremost, I would like to acknowledge my mom, Vicky. Your moral, emotional and financial support has been crucial to my success not only in graduate school, but throughout my entire life. My debt to you is immeasurable. Similarly, I want to thank my fiancé, Tyler, who has been a constant supporter and source of encouragement. Both of you have been a backbone of this journey for me.

I truly wish to express my sincerest gratitude and appreciation to my graduate advisor, Dr. Colin Johnson. Without his guidance and encouragement in developing my capabilities as a scientist, educator and mentor I would not be as prepared as I am to enter into the next phase of my career. He was a guide and voice of reason when I was frustrated, but allowed me to venture in my own creativity and ideas when they came. In doing so, he allowed me the greatest freedom and independence of thought and discovery in his lab and for this I will forever be grateful.

I would like to thank my committee members, Dr. Elisar Barbar, Dr. Kate Schilke, Dr. Victor Hsu and Dr. Weihong Qiu, as well as Dr. Ryan Mehl for their guidance and technical help in my research. I would also like to thank faculty in the Biochemistry and Biophysics department that I was fortunate enough to work with in various teaching laboratories and classes as well as all the GTA's and UTA's who I worked with.

I would like to finally thank my mentors. Ms. Wanda Crannell, Dr. Dwaine Plaza, Mr. Frederick J. Edwards, Dr. Jennifer Brown and Dr. Charlene Alexander. Although you all came into my life at various stages, the time that I spend with you all has been invaluable. Each of you has played an instrumental role in not only my professional development, but also my personal growth. With all my gratitude and sincerity, I thank you.

CONTRIBUTION OF AUTHORS

Chapter 2

Nicole J. Hams collected the data. Nicole J. Hams, Dr. Weihong Qiu and Dr. Colin Johnson were involved in experiment design. Nicole J. Hams and Dr. Colin Johnson wrote the manuscript.

Chapter 3

Shauna Otto preformed the preliminary experiments. Nicole J. Hams performed experiments and collected the data. Nicole J. Hams and Dr. Colin Johnson were involved in experiment design. Nicole J. Hams and Dr. Colin Johnson interpreted the data and wrote the manuscript.

TABLE OF CONTENTS

Page

TABLE OF CONTENTS (CONTINUED)

Page

TABLE OF CONTENTS (CONTINUED)

Page

LIST OF FIGURES

LIST OF SUPPLEMENTAL FIGURES

LIST OF TABLES

Chapter 1

Introduction and literature review

Nicole Hams

1.1 Lipids and membranes

Compartmentalization is one of the fundamental principles of eukaryotic cells. Sub-compartmentalization by membrane-bound organelles within the cell enables segregation of specific chemical reactions to increase biochemical efficiency. Eukaryotic organisms must be able to maintain the integrity of membrane-bound organelles while simultaneously transporting cargo from one compartment to another, in and out of the cell. To do so, eukaryotes must undergo continuous fission and fusion of organelles and whole cells without disrupting intracellular contents. Membranes provide the strong and flexible barriers that mediate this process and thus play an important role in all these essential functions[1,2]. Membranes enclosing cells and organelles are defined by a series of flat and curved regions[3]. These regions arise as a result of asymmetric distribution of lipids between the leaflets[4,5].

Lipids are the basic unit of all membranes and are responsible for membrane features such as curvature, thickness, fluidity and pressure[1,6–8]. Phospholipids, the most abundant lipids in membranes, consists of hydrophobic head groups and at least one hydrophobic fatty acid hydrocarbon tail[1]. Variations in the type of head group and the number and length of the hydrocarbon tail directly affect membrane packing[9]. Major structural phospholipids of eukaryotic membranes include phosphatidylcholine (PC), phosphatidylethanolamine (PE), phosphatidylserine (PS), and phosphatidylinositides (PI). Phosphatidic acid, a pre-cursor to phospholipids, is also found in high abundance in eukaryotic membranes[4]. PC accounts for more than 50% of lipids in all biological membrane types[4], while, lipids PE and PS are enriched in the cytosolic leaflets of the endoplasmic reticulum, Golgi body, plasma membranes and early endosomal membranes[3,10–13]. PS is an anionic lipid and as a result, membrane electrostatics depend largely on the amount PS present, which ranges from a low percentage in the endoplasmic reticulum to more than 10% in plasma membrane[6].

PIs are another class of lipids found in eukaryotic membranes. The PIs and PIPs (PI derivatives), play an important role in membrane homeostasis[4,14,15]. PIPs located on the cytosolic surface of cells often recruit organelle-specific proteins involved in vesicle trafficking and signal transduction[16,17]. For example, phosphatidylinositol 4,5-bisphosphate ($PI(4,5)P_2$) is found on the inner leaflet of the plasma membranes where it plays a role in G protein receptor signaling, cytokinesis, endocytosis and apoptosis[16,18–21]. Both $PI(4,5)P_2$ and phosphatidylinositol 4-phosphate (PI4P) are concentrated at membranes involved in exocytotic pathways[22].

Additionally, PI4P can be found in the trans-Golgi network[4]. Phosphatidylinositol 3-phosphate (PI3P) is found primarily in late endosomes and is a precursor to phosphatidylinositol 3,4-bisphosphate ($PI(3,4)P_2$), phosphatidylinositol 3,5-bisphosphate ($PI(3,5)P_2$), and phosphatidylinositol 3,4,5-triphosphate ($PI(3,4,5)P_3$)[4]. PI3P and its three derivatives all have distinctive subcellular localization and are key regulators of membrane trafficking events that occur at those location[17,22,23]. For example, $PI(3,4)P_2$ plays a regulator role during the late stages of clathrin-mediated endocytosis[24]. $PI(3,5)P_2$ is present on late endosomes and plays an autophagy and lysosome function[25]. At the plasma membrane, $PI(3,5)P_2$ and $PI(3,4,5)P_3$ act as secondary messengers that are required for cell growth and survival[26,27].

1.2 Calcium mediates C2 domain interactions with membranes

C2 domains are one of three major classes of calcium sensing motifs, along with EF hands and annexin folds[28]. However, C2 domains are unique in that they directly regulate calcium-mediated cell signaling and membrane trafficking. C2 domains were originally identified as one of two conserved regulatory domains in several isoforms of calcium-dependent protein kinase C (PKC)[15,29–35]. The first regulatory domain, C1, interacts with phorbol esters and diacylglycerols[29]. The second regulatory domain, C2, was found to bind calcium. PKC isoforms lacking the C2 domain were not regulated by calcium, and thus C2 domains were thought to regulate calcium in their local environment[29,36,37]. Most C2 domain-containing proteins have a role in calcium-dependent signal transduction or membrane trafficking events, and studies of isolated C2 domains have confirmed this notion[15,31,32,36,38–49]. Some C2 domains have lost the ability to bind calcium, and instead specialize in protein-protein interactions, calcium coordination, and small molecule binding[36,50,51]. C2 domain containing proteins are widely distributed in eukaryotes, but very rare in prokaryotes, where calcium signaling is less widely used as a form of signal transduction[15,36]. Genome analyses indicates there are 99 human proteins that contain 149 C2 domains. However, this is considered a conservative estimate given there is only 20-30% sequence conservation between C2 domains[52,53]. Excluding the ferlin family, the majority of C2 domain-containing proteins only have one or two C2 domains[36].

C2 domains are independently folded motifs that are roughly 130 residues in length (Figure 1.1)[28–30,36,54,55]. They consist of conserved beta sandwiches with variable surface loops that directly interact with calcium and membranes[15,28,36,56,57]. The structure has been solved for

some C2 domain-containing proteins, including members of the synaptotagmin family and phosphoinositide-specific phospholipase C[58,59]. There are two types of C2 domain topologies. In Type I topology, the first beta-strand occupies the same spot as the eight beta-strand in Type II topology[15,28,57]. A sequence alignment of 65 C2 domain-containing proteins revealed that while C2 domains at the C-terminus of proteins contained both topology types, those located on the N-terminus were primarily Type II topology[36].

Many C2 domains regulate calcium-activated events by binding calcium in a negatively charged binding pocket. Calcium is thought to regulate C2 domains function by facilitating a changed in electrostatic potential that is important for regulating interactions[28,56,60–63]. For example, the crystal structure of the PKCα C2 domain complexed with phospholipids revealed calcium acts as an electrostatic bridge between the lipid and protein[64]. Lipid binding and NMR studies have been used to determine that C2 domain can bind 2 to 3 calcium ions[15,62,65]. In C2 domains that bind calcium, the ions cluster exclusively at the top loops between beta-sheets two and three or six and seven, and are primarily coordinated by negatively charged aspartic and glutamic acid residues (Figure 1.1)[15,28,36,50,51,57]. In fact, the majority of sequence conservation among C2 domains are found in acidic amino acids that coordinate calcium[57]. Asparagine, glutamine, serine and threonine are sometimes substituted in the absence of aspartic and glutamic acid. It's suggested that these single amino acid substitutions are a result of small evolutionary changes needed to optimize calcium binding requirements for protein function[36,50]. Although calcium binding does not induce global conformational changes, it can influence local structure changes. Structural analysis via NMR of C2 domains suggests that calcium does not induce a conformational change in the beta sheet, but instead stabilizes the calcium binding regions of the loop[57,65]. Comparison of calcium-bound and -free forms of synaptotagmin, phospholipase C and protein kinase C reveal subtle rotations of side chains near the calcium binding regions, but no drastic conformational changes[64–67].

Calcium binding by the loops of C2 domains is a method of facilitating lipid coordination, however that binding mechanism that precedes this outcome is unclear. One model suggests that calcium ions act as an ionic bridge in which they bind the C2 domain and phospholipids simultaneously[68,69]. Alternatively, a different model implicates calcium as an electrostatic neutralizer that once bound, allows the C2 domain to bind phospholipids[70]. The sequence of the binding loop is thought to play a role in lipid preference. For example, synaptotagmins and

classical protein kinases interact with membranes via anionic lipid head groups, while C2 domains in cyclic phospholipase A bind neutral lipid head groups[48,67,71–78]. This difference may be due to the presence of two extra acidic residues in loops one and three[57]

Beside binding lipids via the loops, C2 domains can also interact with membranes via a cationic beta groove[28]. The X-ray crystal structure of various C2 domains showed it was able to complex with PS in the calcium binding loops and $PI(4,5)P_2$ via lysines in the polybasic cluster of beta strands three and four[64,67,72,73]. Lysine, as well as aromatic amino acids tyrosine and tryptophan, form direct interactions with the lipid moieties. Further, residues Y195, K197 and K209 were all found to be conserved in rabphilin 3A and isoforms of synaptotagmin, RIM and protein kinase C[15].

1.3 Synaptic-vesicle fusion is a form of membrane trafficking

Unlike organelles that are able to synthesize lipids, the plasma membrane, endosomes and lysosomes depend entirely on membrane trafficking events to supplement the lipids in their membranes. Membranes involved in secretory or endocytotic pathways are often trafficked through budding and fusion events. Budding, fusion and fission are required for cellular functions such as intracellular communication, cytokinesis, viral propagation, mitochondrial division and the generation of the endoplasmic reticulum network[79–86].

Neurotransmission is a special type of fusion event that allows for rapid communication and coordination of multiple cells, simultaneously. Neurotransmission is mediated by synaptic vesicles, spherical lipid bilayers approximately 40-100 nm in diameter, which function in the uptake and release neurotransmitter molecules[87–89]. The release of neurotransmitters is mediated by fusion, which is the process of two separate membrane bilayers merging into a single bilayer. Synaptic fusion, is a form of heterotypic fusion, in which two dissimilar membranes, such as the plasma membrane and a synaptic vesicle, merge into a single bilayer. This is in contrast to homotypic fusion, in which two similar compartments merge, such as the case in endosomal fusion events[51]. Purified synaptic vesicles are composed primarily of PC, PE, PS, PI, and cholesterol[90]. Synaptic vesicles often have protein associated with them, either peripherally or integrally, to mediate the fusion process. Additionally, there are also important proteins located on the plasma membrane, where fusion occurs. These areas are known as active zones (AZs)[91]. The AZ is defined as an electron-dense area located at the presynaptic

plasma membrane directly opposite the synaptic cleft[89]. It is there that synaptic vesicles are captured and organized for fusion[92–95]. Neurotransmission occurs when an action potential triggers neurotransmitter release from a presynapse. The action potential causes the opening of voltage-gated calcium channels that result in calcium-dependent fusion events. Thus, calcium triggers the fusion of synaptic vesicles that contain neurotransmitters to the presynaptic plasma membrane, an event that occurs on the sub-millisecond timescale and in a spatially and temporally precise manner [9,61,89,96,97].

Physically, fusion is mediated by both protein-protein and protein-lipid interactions. Once the vesicle arrives at the plasma membrane, soluble NSF (N-ethylmaleimide sensitive fusion protein) attachment protein receptor (SNARE) proteins work to physically restrain the vesicle as a method to keep it from diffusing away, in a step is known as "tethering" (Figure 1.2). This is followed by the "docking" phase where individual SNARE proteins located on either membrane form a SNARE complex. Once the SNAREs form a stable complex, the vesicle is considered "primed" and upon the introduction of calcium, the vesicle fuses to the plasma membrane in a process mediated by synaptic-fusion proteins[89,98,99].

Although some fusion pathways have specialized attributes, all fusion events have a common underlying mechanism that describes the way in which the membranes rearrange, known as the stalk hypothesis[9,51]. It essentially states that when two phospholipid bilayers that are closely opposed, but separate, begin to merge the outer leaflets of either bilayer form a transitional state referred to as hemifusion (Figure 1.2). It is thought that the majority of fusion events involve a hemifusion intermediate, where only the outer leaflets of either membrane merge, but not the inner leaflets[100]. From there, a fusion pore is formed, in which both outer and inner leaflets of one membrane joins with outer and inner leaflets of the opposing membrane. The fusion pore begins as lipidic, however it is unclear whether transmembrane proteins, such as SNARE, localize there to exert a mechanical force on the bilayers that facilitates pore formation[101]. Finally, the pore expands, thereby completing the fusion process. Although the stalk hypothesis describes a transition state during membrane fusion, reports have been published in which fusion between a liposome and a planar membrane resulted in "flickering" before the formation of the fusion pore[102,103]. These events are likely a result of improper protein interactions that fail to overcome energy barriers that prohibit fusion. This finding is important because it highlights the significance of proper protein interactions that provide both

membranes to overcome the repulsive forces of opposing phospholipid-bilayers. The energy barriers associated with fusion include (1) repulsive charges, the result of two membranes together, (2) membrane deformation and rearrangement during stalk formation or fusion pore opening, and (3) transmembrane protein rearrangement[51,100,104]. Fusion transition states, in which phospholipid membranes are arranged in highly curved monolayers, is energetically unfavorable and thus require a strong yet transiently stable interaction to drive both membranes towards fusion.

1.4 Synaptotagmin-I: A calcium-sensor for synaptic vesicle fusion in neurons

Synaptotagmins are a class of vesicle-localized proteins that contain an N-terminal transmembrane domain with two cytoplasmic C2 domains, C2A and C2B[43,45,51,67,89]. The 17 members of the synaptotagmin family all have a different calcium affinity and are suggested to mediate calcium-dependent fusion in specific tissues[55,57,89,105–107]. For example, synaptotagmin-V is involved in insulin exocytosis while synaptotagmin-VI is involved in spermatozoa maturation[108–110]. Both isoforms are predicted to bind phospholipids and induce membrane curvature in a calcium-dependent manner[67,89,108,109]. Synaptotagmin-VII is mediates fusogenic events at the plasma membrane and lysosome in a wide variety of tissue types. In pancreatic islet cells it fuses insulin or glucagon-containing vesicles to the plasma membrane[51,111]. Additionally, it is predicted to bind membranes in a calcium-sensitive manner and induce membrane curvature[112].

Synaptotagmin-I (Syt-I) is the calcium sensor for exocytosis at neuronal synapses. This protein plays a crucial rule in neuronal development, and in mice, a homozygous knock-out is lethal[113–117]. Syt-I is localized to synaptic vesicles where it mediates fusion in nerve synapses via interactions with SNAREs and anionic phospholipids at the plasma membrane[55,57,73,118]. In synapses where Syt-I is not expressed, isoforms II or IX, which are predicted to induce membrane curvature, have been suggested to act as functional substitutes[107,119,120]. The two C2 domains of Syt-I are separated by a flexible nine-residue linker that adopts a variety of orientations[121–124]. Multiple structure resolution techniques such as X-ray crystallography, NMR and EPR have demonstrated different orientations of the Syt-I C2 domains[125–129]. Since C2 domains do not undergo large conformational changes, it has been proposed that the relative

orientation of these domains is what drives the different functional states of C2-domain containing proteins[43,45]. During neurotransmitter release, for example, it is crucial for both Syt-I C2 domains to be pointed in the same direction to facilitate membrane interactions, a prerequisite for fusion[61]. However, at a resting state, both C2 domains point in different directions, and thus synaptic vesicle release is inhibited[61,130–132].

NMR and X-ray crystal structures of the Syt-I C2A domain revealed a canonical C2 domain fold: a compact beta-sandwich composed of two, 4-stranded beta sheets and calcium binding loops[57]. Loops I and III of Syt-I C2A domain coordinates three calcium ions using electrostatic side chains contributed by aspartic acid and serine residues[51,89,131]. Calcium coordination occurs in a cooperative manner where each site has a different affinity for calcium (120μM, 465μM and 1.7mM)[133]. In contrast, the calcium binding loops in the C2B domain coordinate two calcium ions via conserved aspartic acid residues that bind calcium with equimolar affinity[51,55,133–135]. In addition to synaptotagmin-I, isoforms II III,V-VII, IX and X have also been shown to bind calcium[136,137].

In response to calcium, both C2 domains of Syt-I interact with PS-containing lipids[48,104,130,135,138–141]. Studies using isolated C2A domains revealed that the interaction with phospholipids only occurs in the presence of calcium, but not other divalent ions such as magnesium, barium or strontium[57]. These results suggest that Syt-I membrane interactions are driven by calcium signaling specifically and not the presence of any ion. The Syt-I calcium complex (Syt-I•Ca^{2+}) is essential for stimulating membrane fusion and Syt-I will not bind liposomes when calcium binding residues are mutated[123,133,142,143]. Further, in vitro fusion assays revealed that mutating Syt-I calcium coordinating residues decreased its ability to fuse giant unilaminar vesicles[144]. The positive charge from the calcium neutralizes the negatively charged loops on the C2 domains to facilitate interactions with the negatively charged phospholipid[55]. This “electrostatic switch” model was originally proposed by Shao et al[62]. Both C2 domains contribute essential lipid coordination residues. Specifically, mutations of D230 (C2A), N232 (C2A), D363 (C2B) and N365 (C2B) abolish Syt-I lipid aggregation activity, entirely[144]. Mutations of these residues in either C2 domain cause a significant decrease in membrane interactions. Further, simultaneous mutations did not induce a greater decrease in membrane affinity. These findings suggest that the C2 domains cooperate to penetrate membranes[61,124,144]. The C2A and C2B domains have different lipid-biding properties[57]. Where the C2A domain preferentially binds

PS-containing membranes, the C2B domain prefers PI(4,5)P_2-containing membranes[51,143]. Additionally, synaptic proteins such as AP2, calcium channels and the lipid PI(4,5)P_2 bind C2B, but not C2A[143,145–149]. Taken together, these results support the hypothesis that each C2 domain of Syt-I has evolved specialized functions at the neuronal synapse.

Syt-I•Ca^{2+} interacts with PS lipids by inserting neutralized calcium binding loops into the lipid bilayer[113,124,130,138,143,147,149–153]. The omission of PS from binding studies abrogates the ability of Syt-I to regulate fusion, further highlighting the importance of Syt-I•Ca^{2+} -membrane interactions[123]. Syt-I has been shown to regulate fusion by bending the target membrane[144]. Hydrophobic insertion could cause the outer leaflet to bend and create a dimple, presumably as a method overcome fusogenic energy barriers[55,109,109,154–157]. Indeed, the ability of Syt-I to insert into membranes has been directly tested. Syt-I residues M173, F234, V304 and I367 were found to be directly involved in membrane penetration and have been calculated to penetrate ⅓ of the monolayer depth[109,150]. In the absence of calcium, Syt-I interacts with membranes independent of liposome size. However, upon the introduction of calcium into the system, Syt-I preferentially penetrates smaller liposomes. In fact, the reduction of liposome diameter from 252nm to 105nm caused a 9.3-fold increase in binding affinity[144,155]. Further, membrane penetration activity seems to be cooperative. Hui *et al*. found that the C2B domain was able to insert into membranes to a greater degree when tethered to a "dead" C2A domain, a mutant that could not coordinate calcium ions, as compared to the membrane penetration activity of an isolated C2B domain[155]. This experiment demonstrates C2 domain cooperativity, and also suggests that the presence of C2A, and not its ability to bind calcium, is more essential for C2B domain-mediated membrane penetration. Further, it was concluded that Syt-I curvature "sensing" is likely a passive function of its membrane-insertion activity[144,155].

Following membrane penetration, membrane bilayer bending and rearrangement are required to achieve fusion. Membrane bending and rearrangement would potentially accelerate fusion by 1) creating a dimple that drives out water thereby increasing lipid-lipid interactions and reducing lipid-buffer interactions and 2) increasing tension in the plasma membrane to allow hydrophobic interactions to form between the acyl chains of either membrane outer leaflet. To test the ability of Sty-I to rearrange membranes, Hui *et al.* incubated liposomes with vesicles, and using electron microscopy, found that Syt-I tubulates liposomes in the presence of calcium. When the tubulation ability of each C2 domain was tested, it was observed that only

C2B was able to tubulate membranes. These findings raised the question of whether the membrane tubulation activity of C2B was dependent upon the presence of C2A. To this end it was shown that while C2AA (two Syt-I C2A domains separated by the native linker) still did not tubulate, C2BB (two Syt-I C2B domains separated by the native linker) sent Syt-I tubulation activity into overdrive, resulting in lipid fragmentation[155]. These results suggest that while C2B is directly responsible for membrane remodeling activity, the C2A domain regulates this function by driving remodeling towards fusion while avoiding "pinching off" which results in fragmentation. The fact that C2A penetrates lipids, but does not drive tubulation, suggests that penetration alone is not sufficient for membrane bending and remodeling. Further, it provides more support for the idea that each C2 domain has a specialized function. Site-directed mutagenic studies of Syt-I have been used to determine whether either C2 domain of Syt-I engage membranes simultaneously or with distinct kinetics. Surprisingly, they are all in agreement that both C2A and C2B domains rapidly penetrate bilayers with similar kinetics[124,143]. These findings support a previous model in which the C2 domains of Syt-I must point in the same direction to facilitate fusion[43,48,61,130,131].

Not all Syt-I lipid-binding interactions are mediated by calcium. The C2B domain of Syt-I bind PI4, PI5 and PI6, as well as PI(4,5)P_2, independent of calcium via a polybasic region on the beta sandwich[15,129,143,158–160]. The polybasic region of Syt-I consists of a lysine-rich patch that involves K313, H315, K326 and K327[133]. A K326E mutation did not alter the rate at which fusion was accelerated, suggesting that the polybasic stretch is not required for fusion in vitro[109]. The polybasic region on Rabphillin-3A is required from plasma membrane localization[161]. The polybasic region on Syt-I has a similar function. Several studies demonstrated that PI(4,5)P_2 is required at the plasma membrane for calcium-dependent exocytosis [15,143,158,162,163]

Besides lipids, Syt-I must also directly interact with SNAREs in order to facilitate fusion[121,123,130,157,164,165]. *In vitro* fusion assays demonstrated that fusion is accelerated when Syt-I is in the presence of SNAREs. Specifically, Syt-I was found to enhance the speed of forming a stable SNARE complex, thus facilitating fusion pore opening and accelerating fusion[73,109,122,166,167]. Syt-I C2 domain linker length is essential for SNARE interactions. Not only must both C2 domains be tethered together, but altering linker length results in changes of C2 domain orientation which alters SNARE binding[122,130,138,153,156,168]. Syt-I C2AB shows weak calcium-independent SNARE binding that is enhanced in the presence of calcium[169]. However, individual domain

assays reveal that C2A binds neuronal t-SNARES (syntaxin1A and synaptosomal associated protein 25, SNAP-25) in a calcium-dependent manner while C2B binds t-SNAREs independent of calcium[48,57,166,170]. Binding between SNAREs and Syt-I can be abrogated by salt, suggesting the interaction is electrostatic[168,169]. In addition, the polybasic region of C2B Syt-I has been shown to mediate syntaxin1A interactions[15,51,171].

Mutations that affect the membrane bending activity also affect t-SNARE interactions, and therefore, may serve a dual purpose at neuronal synapses. The membrane aggregation activity of Syt-I would promote the association of v-SNAREs in vesicles with t-SNAREs at the plasma membrane, which is is supported by the observation that Syt-I does not bind v-SNAREs[152]. Martens and McMahon suggested a model for Syt-I and SNARE interactions during fusion where, upon calcium influx and binding, the C2A and C2B domains are targeted to the plasma membrane via $PI(4,5)P_2$, and there, rapidly penetrate membranes to induce curvature. This activity results in membrane buckling, and the resultant stress is thought to reduce the energy barrier for fusion. During this time, synaptic vesicles containing v-SNAREs would form a stable SNARE complex with t-SNAREs on at the plasma membrane to promote fusion[109].

1.5 The Ferlin protein family mediates calcium-dependent membrane interactions

Ferlins are a large family of proteins (200-240kDa) classified for having five to seven tandem C2 domains with a single-pass transmembrane domain on the C-terminus (Figure 1.3). Little is known about the benefit of multiple C2 domains, but it has been proposed that they create a synergistic effect that is necessary for preferential lipid recognition or conferring calcium thresholds[50,124,165,172]. Similar to the 13 different isoforms of synaptotagmins, each ferlin may mediate vesicle trafficking or fusion events in specific tissues or subcellular locations.

All ferlins have a FerI motif between the C2B and C2C domains[47,50,55,56,173,174]. Outside of ferlins, only multiple C2 domain and transmembrane region proteins (MCTPs) and extended synaptotagmins have more than two C2 domains[28,174–177]. In humans, ferlins play an indispensable role in membrane trafficking, and are commonly linked to pathologies involving defects in calcium-dependent vesicle fusion[55,56]. The ferlin family was named based off their homology to the first ferlin gene discovered, Fer1, a *Caenorhabditis elegans* spermatogenesis factor[178]. Fer1 mutants are infertile due to their inability to fuse with the spermatozoon plasma membrane. As a result, spermatozoa have reduced motility compared to wild-type samples[179].

Drosophila melanogaster possess a ferlin paralog, misfire, that plays an important role in fertilization and embryonic development. Misfire mutations in male fruit flies causes defects in calcium-dependent degradation of spermatozoon plasma membranes[180,181].

Ferlin and ferlin-paralogs are widespread among eukaryotes. Sequence analysis of these proteins suggest they all arose from a common ancestor and then evolved to perform specialized functions[56]. The FerI domain in mammalian ferlins is found in protozoan ferlin-like proteins, suggesting that particular motif may have a function that is conserved throughout evolution. Further, unicellular plankton possess a ferlin-like gene that is structurally similar to the ferlins found in mammals. Mammals have six ferlins; Fer1L1 (dysferlin), Fer1L2 (otoferlin), Fer1L3 (myoferlin), Fer1L4, Fer1L5 and Fer1L6. Five ferlin paralogs have been found in sharks whereas only two are found in lamprey. These results are reported to suggest the ferlin family expansion from two to six members occurred around the same time that vertebrates developed a lower jaw. The mammalian ferlins are further classified by the presence of a DysF domain, Type I (with a DysF) and Type II (without a DysF). The sub-classification of ferlins suggest that the family likely originated from two ancestral ferlins[50]. DysF is present in dysferlin, myoferlin and Fer1L5. Structural analysis results of myoferlin DysF revealed two antiparallel beta-strands (Figure 1.3). Although the function of this domain in the ferlin family remains unknown, in yeast vacuoles it has been shown to regulated peroxisome size and number[182]. Even though there are six ferlins found in mammals, the family varies in whether members contain a C2A domain, a FerA domain or a C2DE domain (Figure 1.3)[50,56]. So far, there is no known function or interaction attributed to the DysF or Fer domains despite being conserved across the ferlin family. The C2E and C2F domains are the most conserved amongst the family, especially at calcium binding residues[50].

1.5.1 Dysferlin

Dysferlin has a total of six C2 domains that bind phospholipids in a calcium-dependent manner[183,184]. The majority of its C2 domains are predicted to possess calcium binding residues. Structural analysis of its C2A domain suggests it binds phospholipids and indeed has been physically shown to bind PS and PI(4,5)P_2 in a calcium-dependent manner[50,55]. Mutations in dysferlin are responsible for a group of disorders known as dysferlinopathies. These include limb-girdle muscular dystrophy (LGMD) type 2A, as well as a distal form of muscular dystrophy

called Miyoshi myopathy. Both LGMD 2A and Miyoshi myopathy are autosomal recessive disorders characterized by a reduction or absence of dysferlin in skeletal muscle[55,56,178,185–187]. Those suffering from dysferlinopathies have unique types of muscular dystrophy in which repair, and not the structure, of the plasma membrane is disrupted[169].

In healthy skeletal muscle dysferlin localizes cytoplasmic vesicles and the plasma membrane[188–190]. Techniques such as immunofluorescence, 3D-SIM and flow cytometry have also been used to validate the cellular localization of dysferlin[55]. Further, dysferlin RNA transcripts can be found in the skeletal, brain, heart and placental tissues and too a less degree in liver, lung kidney and pancreas tissue[56,178,186,191]. In tissues effected by dysferlinopathies, dysferlin is instead distributed more in the cytoplasm of skeletal muscle[56]. Dysferlin null-mice develop slow, progressing muscular dystrophy, and by eight months exhibit pathological characteristics associated with muscular dystrophy, such as regenerating fibers, split fibers, muscle necrosis and macrophage infiltration[192]. Finally, tissues harboring dysferlinopathies have an accumulation of vesicles at the plasma membrane and in affected mice, despite localizing to the site of injury, vesicles don't fuse to the plasma membrane[55,111,184,189,190,192]. These findings strongly suggest that dysferlin primarily plays a direct role calcium-activated membrane repair.

The mechanism that dysferlin uses to mediate calcium-activated membrane repair is not well characterized. It's thought that calcium influx recruits dysferlin to the injury site where it interacts with vesicles and other membrane repair proteins to create a hydrophobic "patch" at the wound site[193,194]. Though a series of events that have yet to be elucidate, dysferlin is proposed to facilitate the docking and fusion of these vesicles to the plasma membrane in a process similar to exocytosis[188,192,195]. Indeed, *in vivo* and *in vitro* assays have revealed dysferlin interacts with proteins involved in membrane fusion, including syntaxin4 and SNAP-23[195–198].

Dysferlin may also have secondary functions in the cell, as it has been implicated in other membrane trafficking pathways[199–202]. For example, dysferlin-null mice have twice as many lysosomes as wild-type mice, suggesting that dysferlin might be important for lysosomal homeostasis. Additionally, dysferlin-null myoblasts have an accumulation of IGFR, suggesting an unknown role for dysferlin in receptor trafficking, perhaps via an endo-lysosomal pathway[55]. However, the exact role for dysferlin in these pathways remains poorly characterized.

1.5.2 Myoferlin

Myoferlin is most closely related to dysferlin and along with Fer1L5, share a common structural motif, the DysF domain[50,203]. Myoferlin C2A domain crystal structure putatively supports its ability to bind calcium[56]. Upon mutation of the C2A domain, myoferlin loses its ability to form calcium-dependent phospholipid interactions[203]. Physiologically, myoferlin RNA transcript is found in skeletal and cardiac muscle, as well as placental, brain, lung, liver, kidney and pancreatic tissue, but to a lesser extent[56]. However, it is primarily expressed in myoblast that are about to undergo cellular differentiation[203].

Myoferlin mediates myoblast fusion to generate mature, multinucleated skeletal muscle. Myoblast from myoferlin-null mice displayed significantly fewer multinucleated myotubes suggesting they were unable to efficiently fuse. Myoferlin-null mice also have smaller muscle fibers and are unable to regenerate skeletal muscle after injury, further highlighting the importance of myoferlin in muscle development and homeostasis[173,203]. Once myoblast fuse to become myotubes, the expression of myoferlin is significantly reduced. However, small amounts of myoferlin can still be found on the plasma membrane of myotubes[204].

Besides muscle development and maintenance, myoferlin is associated with other, less defined roles within and outside the cell. For example, confocal data shows myoferlin localizes to late endosomes where it has a role in endosomal recycling[55]. Additionally, myoferlin has been identified in oncogenic pathways where its expression is upregulated in cancerous tissues[55]. Although the exact mechanism is unknown, it has been associated with cancer progression pathways involving growth factor signaling and exosome transport[205–212].

1.5.3 FER1L4, FER1L5 and FER1L6

The exact function of Fer1L4, Fer1L5 and Fer1L6 have yet to be determined, however the tissues they are expressed in and their cellular locations have been well summarized by Redpath et. al. In humans, high levels of *FER1L4* mRNA were found in stomach tissue compared to other tissue samples. However, FER1L4 is unique among ferlin because it is a non-coding protein whose function remains unknown. *FER1L5* was found primarily in the pancreas, and flow cytometry and 3D-SIM data demonstrated that it localizes intracellularly. *FER1L6* is expressed rather ubiquitously across multiple tissue types, including the heart, kidney, stomach, lung, liver, pancreas, thymus and colon. Flow cytometry and confocal data suggests FER1L6 acts on the

plasma membrane, trans-Golgi network, endosomal recycling pathway and perinuclear regions[55].

1.5.4 Otoferlin

Otoferlin is primarily expressed in the brain and cochlea[55,56,213]. Within the cochlea, otoferlin is found on vesicles docked at the plasma membrane of cochlear inner hair cells (IHCs)[47,51,56,213,214]. Otoferlin is inserted into synaptic vesicles via the transmembrane recognition complex pathway. In this pathway, the protein ,Trc40, binds the C-terminal transmembrane domain (TMD) of otoferlin as it's coming off the ribosome and transfers it to the endoplasmic reticulum. There, the otoferlin/Trc40 complex is targeted to the Cml/Wrb complex which mediates the insertion of otoferlin's TMD into the membrane bilayer. Next, vesicles containing otoferlin a trafficked to the PM via the ER budding process. Trc40 has been found to be critical for normal otoferlin abundance in IHCs. Further, mutations of proteins in this pathway lead to reduced otoferlin levels and synaptic hearing impairment in mice[215].

Otoferlin is thought to be the calcium sensor for exocytosis in IHCs for multiple reasons. First, mutations in otoferlin always result in a deaf phenotype. For example, otoferlin KO mice are profoundly deaf compared to WT littermates. ABR recordings of WT mice show a lack of brainstem response despite normal otoacustic emissions[55,216–220]. Similarly in humans, those suffering from mutations in otoferlin have highly abnormal brainstem response to acoustic input despite normal mechanotransduction[218,219,221–224]. Mutations in otoferlin generally underlie a pre-lingual autosomal recessive form of non-syndromic deafness, DFNB9[216,225–234]. However, not all mutations in otoferlin cause pre-lingual deafness. The I515T mutation causes temperature sensitive hearing loss during periods of physical activity or high fever. Patients harboring this mutation also are affected by moderate age-progressive hearing loss[221–223,230,235–238]. Heat induced protein unfolding provide a candidate mechanism for temperature-sensitive hearing loss mutations in otoferlin. In mice with I515T mutations the levels of otoferlin are significantly lower than that of wild-type littermates. These findings suggest that the lower otoferlin levels are likely a result of the protein being degraded in IHCs[230].

Second, otoferlin binds lipids and associates with synaptic vesicles. Five of six otoferlin C2 domains bind lipids in a calcium-sensitive manner[56,216,231,234,239]. Additionally, otoferlin has been shown to interact with the plasma membrane-specific lipid, $PI(4,5)P_2$[239]. The C2A domain

of otoferlin does not interact with lipids. The crystal structure of this domain supports its inability to bind calcium due to shorter loops that lack of calcium-coordinating aspartates[239,240]. Lipid binding for otoferlin C2B-C2F domains is cooperative, but is enhanced in the presence of calcium[231]. Otoferlin has also been shown to not only aggregates liposomes in a calcium-dependent manner, but is also able to perturb liposome structure[47]. In IHCs, otoferlin localizes to ribbon associated vesicles[234]. Otoferlin KO mice are not able to synchronously release synaptic vesicles in response to calcium, despite having the normal numbers of ribbon-associated and docked vesicles[216,225,233]. Further, similar to otoferlin, mutations in other members of the ferlin family underlie vesicle-fusion and membrane trafficking issues in cells. Taken together, these results suggest that otoferlin is involved in the later stages of synaptic vesicle exocytosis at the ribbon synapse.

Third, otoferlin promotes calcium-dependent fusion in the presence of SNAREs. Otoferlin has been demonstrated to bind the (i) neuronal SNARE complex (syntaxin1A/SNAP-25/VAMP-2), (ii) the t-SNARE dimer (syntaxin1A/SNAP-25), and (iii) individual SNAREs, SNAP-25 and syntaxin1A, but not VAMP-2[56,99,216,231,234]. Further, immunofluorescene and western blotting have been used to verify the presence of t-SNAREs in IHCs[241,242]. In vitro, otoferlin, SNAREs and calcium must be present to mediate homotypic fusion. The C2B, C2C, C2D, C2F and C2DEF domains were able to fuse liposomes the fastest. While the C2ABC and C2E domains showed slower fusion kinetics. C2A displayed fusion kinetics that were barely detectable[231].

Finally, otoferlin shares structural and functional similarities to Syt-I. The ability of both proteins to bind SNAREs, calcium and calcium channels suggest that otoferlin acts as the calcium-sensor for fusion in IHCs[216,243,244]. Interestingly, immature IHCs express several synaptotagmins and are able to release neurotransmitter independent of otoferlin; in day old mice, Syt-I, -VI, and –VII are present [231,245]. However, by the time IHCs are mature, 21 days old, synaptotagmins are no longer detectable and all synaptic secretion is mediated by otoferlin[136,245–249]. Thus, there is a yet unknown maturation step that begins to occur around day four in mice in which exocytosis becomes otoferlin-dependent. Despite their structural similarities, Syt-I is not sufficient to produce a brainstem response in otoferlin KO mice. Conversely, otoferlin can not rescue rescue exocytosis in Syt-I null hippocampal or chromaffin cells[250].

Although the exact role of otoferlin during synaptic transmission is unknown, comparative studies between otoferlin mutants suggests that it plays a role in multiple steps in the vesicle fusion process. For example, in otoferlin KO mice, synchronous release is completely abrogated. But, in IHCs with otoferlin D1767G mutation, vesicles in the RRP were able to rapidly fuse to the plasma membrane at the same rate and amplitude as wild-type IHCs, but were not able to maintain that rate or amplitude for sustained periods. Further, in vivo studies with mice harboring this mutation show that mutants have much smaller RRPs than wild-type mice[233]. These results suggest that not only does otoferlin fuse vesicles in response to calcium, it also has a role in replenishing the RRP. However, these findings are difficult to interpret because synaptic function and sound encoding depend upon the amount of otoferlin present at the plasma membrane. For example, in D1767G mutants, otoferlin levels are 3% of wild-type, whereas in I515T mutants are 34% of wild-type[230,233]. Thus, the D1767G phenotype could simply be a result of enough otoferlin being present in the cell to facilitate immediate release, but not sustained release.

Additionally, otoferlin may also play an important role in synaptic vesicle recycling. For example, although otoferlin is primarily localized at the presynaptic membrane, it does not exclusively localize with synaptic ribbons suggesting it plays more than one role in IHCs[251]. Further, confocal data shows otoferlin localizes to the trans-Golgi network and interacts with myosin VI and Rab8, both are which play a role in clatherin-mediated endocytosis[252–254]. These findings are consistent with roles for otoferlin in synaptic vesicle exocytosis as well as membrane recycling.

1.6 Essential proteins for auditory neurotransmission

1.6.1 Synaptic ribbon

Hearing gives us the ability to discriminate and recognize complex auditory signals that span six orders of magnitude. Inner hair cells (IHCs) encode auditory information in a temporal and magnitudinous manner by transforming mechanical stimuli into glutamate release at the synapse[244,255–257]. Force-sensitive stereocilia on the apical surface of the hair cell directly mediate mechanical stimuli on the outside of the cell (Figure 1.4). A single hair cell is estimated to have 63 cylindrical stereocilia of varying lengths distributed along the apical surface. Deflection of the stereocilia open mechanically gated ion channels that allow potassium to rush into the cell[258].

Changes in membrane potential triggers a calcium influx from voltage gated calcium channels. Unlike neurotransmitter release in neuronal synapses that is triggered by action potentials, secretion at sensory synapses, such as IHCs or photoreceptor cells, is controlled by graded exocytosis[259–262]. As a result, sensory synapses are hypersensitive to minute changes in presynaptic membrane potential that arise from sound stimuli[263]. For example, in relative silence, IHCs release glutamates at varying rates, resulting in spontaneous spiking activity in auditory post-synaptic spiral ganglion neurons. This observation arises from IHC response to soft, low pressure sounds that make up background noise[264–268].

IHC synapses are designed to transmit acoustic vibrations with sub-millisecond precision over sustained periods of time[136,269]. Further, exocytosis at sensory synapses occurs within 0.5ms or less after calcium influx. To accomplish such a rapid and sustained response, sensory cells such as IHCs have a synaptic ribbon[91,269,270]. All ribbon synapses are glutamatergic, meaning they release glutamine at high and sustained rates. Ribbon-containing synapse are unique to sensory systems where an extraordinary secretion rate is required to maintain the fidelity and precision of neurotransmission[136,271,272]. Synaptic-ribbons are electron-dense organelles that are often laden with synaptic vesicles (Figure 1.4 A). Ribbons facilitate rapid exocytosis by first binding vesicles from the cytoplasm and then guiding them to the plasma membrane where they are docked near calcium channels[271–273]. Synaptic vesicles are tethered to ribbons with 20nm filaments of an unknown molecular composition[271,274]. Ribbons constrain vesicle to two dimensions, thus increasing the probability of interacting with the plasma membrane[272]. The ribbon was initially thought to be a “conveyor-belt” for vesicle delivery to the PM. However, EM images and modeling studies suggest that it actually functions to slow down vesicles at the fusion site[275]. The molecular diversity between vertebrate AZ proteins of different cell types are thought to underlie specific types of neurotransmitter release. For example, despite being found in neuronal synapses, there are no complexin isoforms found in IHCs[242,276]. Further, nearly all AZ proteins at invertebrate synapses can be found at vertebrate synapses except Piccolo and Bassoon, suggesting the latter two evolved to perform vertebrate-specific functions[93,277]. Immuno-EM images of mouse IHCs suggest Bassoon localizes to the density under the ribbon[278]. These findings are in agreement with immuno-EM images of photoreceptor ribbon synapses in which bassoon localizes to a similar region[279]. Bassoon is required for localizing the ribbon at the active zone[262,272]. This was established after it was found that rapid and precise exocytosis in

response to cellular depolarization is diminished in hair cell synapses lacking bassoon[280]. Other components of synaptic ribbons include Kif3A and RIM1[271,281–284]. Kif3A is a component of the motor protein, kinesin II, that is responsible for moving cargo along microtubules. However, it's function at ribbons remain unknown because the remaining kinesin components, Kif3B and KAP3 are not detectable at the ribbon[284]. RIM1 (Rab3-interacting molecule I) localizes to the synaptic ribbon where it promotes SV priming and docking[46,285].

Ribeye is specific to synaptic ribbons and also happens to be their main constituent. It consists of an N-terminal A domain and a C-terminal B domain. The A domain contains an abundance of serine and proline residues. The B domain is identical to C-terminal binding protein 2 (CtBP2) found in adenoviruses sans the last 20 C-terminal residues[244,271,286]. The structure of the ribeye gene suggests it is a chimer of CtBP2 that is fused to a different N-terminal domain resulting in a novel function. CtBP2 is a transcription repressor found in invertebrates. RIBEYE is thought to evolve from a large exon being fused to the CtBP2 exon[271]. This is considered to be evolutionarily advantageous since CtBP2 acts on nuclear proteins and thus would not be expected to influence secretion. In general, ribbon synapse demand is couple to the size of the synaptic ribbon, a direct effector of the ribbon-vesicle tethering capacity[91,287,288]. For example, ribbons in cone photoreceptor cells tether around 3000 vesicles while 600 are docked at plasma membrane[289,290]. Whereas ribbons found in rod photoreceptor cells tether 640 vesicles and docks 130[272,274]. In six-day old mice, immature ribbons resemble electron-dense spheres surrounded by synaptic vesicles[253,291]. Between six- and ten-day old mice, IHC ribbons begin to acquire their oval shape and by day twelve, they reach morphological maturity in which they resemble oblong spheres that tether vesicles to their outer surface[136]. Piccolino, a short isoform of Piccollo found that is found in the eye and ear, is required for proper ribbon development. Piccollino loss-of-function results in dramatic changes in ribbon shape[292].

Ribbon synapses have three pools of vesicles, 1) a readily releasable pool (RRP) 2) a recycling pool and 3) a cytoplasmic pool[245,293–295]. The readily releasable pool consists of vesicles that are docked at the plasma membrane near calcium channels and thus are the first to fuse mere microseconds after calcium influx[91,296]. These vesicles are proposed to cluster within 100nm of the AZ[297,298]. The RRP of Gerbil IHCs was calculated to be 28 vesicles per active zone which correlates well with other studies that estimate 30 vesicles/AZ in mice and 12 vesicles/AZ

in rats[220,247,251]. The recycling pool consists of vesicles tethered to the ribbon but not docked at the plasma membrane. Vesicles tethered to ribbons are mobile, while those in the cytoplasmic pool are not[299–302]. Further, vesicles tethered to the ribbon do not exchange with cytoplasmic vesicle pools[91,92,296]. Mammalian IHCs have between 100-200 ribbon-associated vesicles. Vesicles tethered to the ribbon can undergo homotypic fusion with vesicles that are in the process of fusing to the PM. This "piggyback" model is consistent with previous EM work which also suggested the existence of compound exocytosis at the PM[289]. The recycling pool exists to replenish the RRP and sustained release is directly linked to this process[293,303,304]. The spatial separation between vesicle release and replenishment motivates a model where vesicles that fuse to the membrane create space for vesicles tethered to the ribbon to dock at the plasma membrane. More simply put, vesicle at the membrane-distal end of the ribbon move in a "conveyor belt"-like formation towards the plasma membrane[92,296]. IHCs can replenish vesicles in the RRP at a rate of 1000 vesicles/second. Specifically, mouse IHCs were found to only require seven seconds to replenish the RRP. This is in contrast to the 12 seconds required in vestibular hair cells or the 1-2s required in retinal bipolar cells. Differences in pool replenishment is thought to arise from differences in the size of their synaptic ribbons[261,305].

Ribbons synapses have two distinct vesicle-release kinetics. The first stage corresponds to the release of the RRP, which occurs roughly 50 μS after calcium influx. The second stage consists of a slower release of vesicles that correspond to the reserve pool[89,247,251,261,294,306–315]. From the viewpoint of experimental setup, RRP depletion rate heavily depends on the strength of the depolarization impulse[316,317]. However, it is important to keep in mind that vesicle release in IHCs is graded and thus the two kinetics pools may be experimental artifacts. In mammals, each IHC has a dedicated spiral ganglion neuron which forms a variable number of synapses via its dendrites. Each synapse is dedicated to a single AZ, which average ~30 per IHC[99,136,258,290,317–319]. Since there is only one ribbon per active zone, it can be estimated that if there are 30 vesicles on an IHC ribbon, then there is roughly 900 vesicles/AZ. These finding support a different study in which mouse IHCs were found to release roughly 700 vesicles/AZ/second, a stark contrast to hippocampal synapses that have a maximal release rate of 20 vesicles/second[233,271]. Thus, it's unclear how targeting, tethering, docking, priming and fusion fit the release kinetics required by IHCs. The speed of exocytosis measured by Sun et. al. 2002 suggests that vesicle recycling is very rapid[320]. Using living bipolar neurons, it was shown that

ribbon-associated vesicles were preferentially endocytosed and recycled at the active zone[299,302,321]. This observation likely arises from the proteinaceous nature of the active zone preventing vesicle-associated proteins that are necessary for fusion from diffusing across the plasma-membrane. Simply stated, all the necessary fusion machinery can be rapidly endocytosed to form another synaptic vesicle. Since there is evidence that docked ribbon-associated vesicles are preferential recycled, it is possible that vesicles farther up the ribbon (un-docked) slowly work their way into the mixture of docked vesicles thus generating the sustained-release component.

Clatherin-mediated endocytosis is thought to be responsible for AZ clearing and membrane recycling[322]. Specifically, AP-2, which has previously to be a component of clatherin-mediated endocytosis in neurons, has been shown to interact with otoferlin. The μ domain of AP-2 was found to mediate otoferlin interactions. In IHCs, AP-2 colocalizes with myosin VI, which is essential for clatherin-mediate endocytosis. Results from auditory brainstem response (ABR) assays suggest AP-2 KO mice are deaf compared to their WT littermates. Further, patch-clamp recordings of endocytotic and exocytotic events in murine organs of Corti show that disruption of AP-2 effects exocytotic events but does not significantly disrupt endocytosis[269,322]. When RRP replenishment was studied, AP-2 KO mice had a significant reduction in vesicle replenishment and fusion kinetics compared to wild-type mice despite a consistent number of membrane-proximal vesicles between both groups. Taken together, these results suggest that AP-2 plays a role in vesicle replenishment via clatherin-mediated exocytosis.

1.6.2 SNAREs

SNAREs are a family of small membrane-fusion proteins that are widespread across prokaryotic and eukaryotic cells. For example, there are 25 types of SNAREs found in *Saccharomyces cerevisiae*, 36 types in *Homo sapiens* and 54 types in *Arabidopsis thaliana* (Figure 1.5). SNAREs, which commonly associate with membranes via a C-terminal, single pass transmembrane domain, play an indispensable role in cellular membrane trafficking[323]. As a result, SNAREs are often shuttled between different subcellular compartments and thus ae widely distributed in cells[9,51,323–327]. SNAREs can be sub-classified into two groups, t-SNAREs (which are localized to the target membrane) and v-SNAREs (localized to the membrane unit that is being trafficked)[9]. During fusion the v-SNARE forms a complex with the t-SNAREs thereby

placing both membranes into close juxtaposition and in doing so creates an unstable membrane environment[51,89]. Once SNAREs interact, they begin a process known as "zippering". SNARE zippering refers to a dynamic state in which the SNAREs form a stable complex. This complex is thought to exert a mechanical force on the membrane that drives lipid rearrangement into a more favorable conformation. In doing so, SNAREs directly reduce the energy barrier associated with fusion[51,89,328]. It was hypothesized that the linker between the SNARE transmembrane domain and SNARE motif is ridged in order to ensure that the energy released from SNARE assembly would directly be transferred to the membranes. However, the introduction of glycine or proline residues in this region had little effect on fusion rates *in vitro* or *in vivo*, suggesting that the linker plays little role in membrane destabilization[329,330].

In neurons, the most common SNAREs include t-SNAREs, SNAP-25 and syntaxin1A and v-SNARE, vesicle-associated membrane protein-2 (VAMP-2). SNAP-25 consists of two cytoplasmic helices that fold in a "bobby pin"-like structure and has been shown to form interactions with Syt-I and calcium channels (Figure 1.5)[121,331]. Unlike most SNAREs, SNAP-25 does not contain a transmembrane domain, and instead associated with the membrane via a palmitoylated cysteine residue[332]. Syntaxins consists of a single cytoplasmic alpha helix that has been shown to directly bind Syt-I, calcium channels and otoferlin[231,234]. VAMP-2, also referred to as synaptobrevin 2, is the most abundant of all three neuronal SNARE, with an estimated 70 VAMP-2 molecules per synaptic vesicle[333,334].

SNAREs alone are monomeric and unstructured, however, upon bind the correct number and type of other SNARE, they form an extremely stable complexes[335]. This complex consists of three SNAREs forming a four-helix bundle, also known as a "SNAREpin"[51,89,328,336–338]. X-ray crystallography, circular dichroism and site-specific labeling support the SNAREpin as being a 12nm-long, four-helix[336,338–342]. The alpha helix in the individual SNAREs that contribute to the SNAREpin are known as a SNARE motif. The residues in this region are highly conserved and single amino-acid substitutions generally result in loss or severe impairment of SNARE function[336,343]. At neuronal synapses, both VAMP-2 and syntaxin1A contribute one helix to the bundle while SNAP-25 contributes two helices[9,101,336,344–346]. The contributed helices come from one of the four classes of SNARE motifs (R, Qa, Qb and Qc)[51,89,343,347–350]. SNARE helices are amphiphilic and as a result, SNAREs form promiscuous complexes with other SNAREs that do not

result in a stable SNAREpin. Stable SNAREpins only form when the bundle contains one helix from each class[351–354].

SNARE "zippering" is the process in which t-SNAREs forms a stable SNAREpin with v-SNAREs thereby forcing the vesicle closer to the plasma membrane[337,355,356]. In fact, once the SNAREpin has been fully assembled there would only be an estimated 4nm gap between the opposing membrane; enough space to accommodate a SNAREpin[51,328]. Zippering occurs directionally, starting at the N-terminal and proceeding towards the membrane-proximal C-terminal[356–362]. SNARE zippering is essential for fusion because it's thought to facilitate the formation of the fusion pore (Figure 1.2)[327]. In support of this, it was found that the energy accumulated during SNAREpin folding (35kBT) is in very close approximation to the energy needed to drive fusion pore formations that lead to fusion (40-50kBT)[328,363]. Further, reconstitution assays using syntaxin1A, SNAP-25 and VAMP-2 show the ability for SNAREs to mediate mixing of the two opposing membrane outer leaflets[337]. Due to its stability, the SNAREpin can only be dissociated using specialized chaperones. N-ethyl maleimide sensitive fact (NSF) and soluble NSF attachment proteins (SNAPs) work together to disassemble the SNARE complex using ATP hydrolysis. SNAP first binds the assembled SNARE complex, which triggers the ATPase activity of NSF. The hydrolysis of ATP mediates a conformational change in NSF to allow for core complex disassembly. However, the exact mechanism as well as other players involved in this process are still poorly understood[51,364–368].

During exocytosis, vesicle docking is enhanced by SNARE interactions with Syt-I[67,73,132]. Additionally, other proteins have been found to interact with SNAREs during fusion, as well. For example, Munc-18, in its unphosphorylated state, is necessary for exocytosis at presynaptic terminals[369,370]. Specifically, during tethering Munc18 binds syntaxin1A thereby inhibiting its interactions with SNAP-25 and VAMP-2[371]. The association of Munc-18 with syntaxin1A prevent promiscuous SNARE binding that lead to unstable SNAREpins[372–374]. However, upon phosphorylation by PKC, Munc-18 dissociates from syntaxn1A thus allowing a SNARE pin to form[371,375,376]. Further, there is new evidence suggesting that Munc-18 may also dually acts as a chaperone that targets synataxin1A to the plasma membrane[376]. Complexins have also been implicated in SNARE binding as well. Complexin forms a tripartite complex with Syt-I and a partially-assembled SNARE complex during the priming phase of exocytosis. It's this interaction that allows Munc-18 to bind syntaxin1A[343,377–380]. It's not entirely understood how SNAREs,

Munc-18, complexin and Syt-I work together to mediate exocytosis. However, it's proposed that the presence of $PI(4,5)P_2$ targets Syt-I to the plasma membrane where Syt-I binds the partially-assembled SNARE complex, displacing complexin and Munc-18. The displacement of complexin allows the SNARE complex to fully form and create a fusion pore[157,169,380,381]. Unfortunately, this model is further convoluted by SNAREs interactions with calcium channels. Co-IP and immunofluorescence have demonstrated the association between t-SNAREs and calcium channels[382–392]. Syntaxin1A modulates the rates of activation and inactivation of calcium channels found in neuronal and cardiac muscle. Similarly, SNAP-25 has been shown to affect the rate of inactivation of calcium channels found in cardiac muscle. Further, changes in channel kinetics as a result of syntaxin1A or SNAP-25 differed significantly from the combined effects of the t-SNARE complex, suggesting the t-SNARE complex interacts with the channels, as well[393].

1.6.3 Calcium channels

Voltage gated calcium channels trigger fast neurotransmitter release in response to changes in membrane potential. Calcium channels have evolved unique physiological and pharmacological properties to support a wide range of electrical signaling events in different cell types[394]. For example, in endocrine cells they mediate secretion of hormones[395]. In skeletal, cardiac and smooth muscle, they activate calcium-sensitive calcium release pathways by binding RyR recepters[396–400]. At the synapses of neuronal and sensory cells, they interact with membrane-fusion mediators in response to nerve impulses[399,401–403].

Voltage-gated calcium channels have a 10nm diameter and are composed of five subunits- $\alpha1$, $\alpha2$, β,δ and γ (Figure 1.6 A)[404]. The $\alpha1$ subunit is a pore-forming, 190kDa protein the consists of four-repeated domains that are comprised of 6 transmembrane alpha helices (Figure 1.6 B)[405,406]. This subunit is responsible for calcium transport through the membrane. Mutagenic studies have established that it can facilitate calcium transport without the presence of the $\alpha2$, β,δ and γ domains, but with abnormal kinetic properties[407–409]. S4 (the 4^{th} helix of the 6-helical bundle on the $\alpha1$ subunit) acts as the voltage sensor. Its rotation initiates a conformational change that opens the pore[394]. S6 acts as the binding site for calcium channel antagonists[410]. The δ subunit is a 33kDa, four-helix bundle that extends across the membrane. Its encoded by the 3' end of the same coding sequence as the $\alpha1$ subunit. The mature δ subunit is proteolytically processed and forms a disulfide bridge with the $\alpha1$ subunit[411,412]. The $\alpha2$

subunit is an extracellular, 170kDa dimer that is directly attached to the γ subunit[412–414]. Although the exact function of the α2γ subunits remains to be explored, a recent study showed it plays a role in modulating the opening of the calcium channel[415]. Mutations in the gene encoding the γ subunit underlies "stargazer" epilepsy in mice, characterized by frequent seizures that include head-tossing and ataxic gait[416]. The β subunit is 55kDa and consists of four intracellular alpha helices that binds the N-terminal α1 subunit via non-covalent interactions[417]. Variations in β subunit isoforms between calcium channel types underlies the differences in kinetics properties and activation voltage[394].

Calcium channels are distinguished by their pharmacological properties, such as the inhibitors that affect them and the effect inhibitors have on channel kinetics[394]. L-type channels show very little calcium-dependent inactivation compared to N-type channels[99]. L-type channels include Ca_v1 channels 1.1, 1.2, 1.3 and 1.4. $Ca_v1.1$ channels are found in skeletal muscle where they participate in calcium homeostasis and muscle contraction[394]. $Ca_v1.2$, 1.3 and 1.4 channels can be found in cardiac muscle, neuroendocrine cells and sensory synapses[99,418,419]. Calcium channels with properties different from those of L-type were first found in electrophysiological studies of calcium currents in starfish eggs and dorsal root ganglion neurons[420–423]. These studies revealed the presence of Ca_v2 channels which include N-,P-,Q- and R-type. Calcium influx in most synapses is mediated by $Ca_v2.1$ (P-/Q-type), $Ca_v2.2$ (N-type) and $Ca_v2.3$ (R-type)[89,99,394,419]. N-type Ca^{2+} channels are localized in nerve terminals and participate in neurotransmitter release in central and peripheral synapses[402,424–427]. N-type channels are activated at more negative potentials than L-type and less negative potentials than T-type, while they are inactivated at rates that are faster than L-type and slower than T-type[423]. P- and Q-type channels are primarily found in purkinje neurons where they are required for inter- and intracellular neuronal signaling. Mutations to P-type channels underlies hereditary migraines and cerebellar ataxia[394]. R-type channels participate in inter- and intracellular calcium release in cerebellar granule neurons[428]. Finally, Ca_v3 channels consists of T-type channels 3.1 and 3.2 that are primarily found in pacemaking cells. These channels are activated at more negative potentials and inactivated rapidly[394].

Calcium channels are required for AZ development in IHCs[264]. Before hearing onset in mice exocytosis in IHCs is evoked by calcium potentials but with low and imprecise transmission[429–431]. However around day six, IHCs start to display more vesicle release that is

synchronous with calcium influx[245]. Fluorescence imaging of calcium influx has revealed localized calcium domains in mature hair cells of mice, but less spatial confined calcium influx for immature hair cells[15]. Calcium channels commonly co-immunoprecipitate with synaptic proteins such as SNAREs and synaptotagmin[382,383,432–434]. The coupling of calcium channels with calcium-sensors for membrane fusion positions vesicles at the site of calcium influx and play a direct role in synaptic fidelity[435]. For example, the C2B domain of Syt-I binds N-type calcium channels in a calcium-dependent manner in neurons during synaptic exocytosis. The $\alpha 1$ subunit facilitates the interaction with Syt-I via a region of the intracellular loop between $\alpha 1$ domains II-III (Figure 1.6 B) called the synaptic protein interaction (synprint) site[146]. Proteomic screens, yeast two-hybrid and co-immunoprecipitation experiments provided evidence for interactions between the synprint site and t-SNARE dimers as well as t-SNARE constituents[146,387–389,418,436–438]. There are two N-type calcium channel splice variants that both lack the synprint site[439]. These variants target the axon of cultured hippocampal neurons but not the presynaptic membrane further highlighting the importance of the synprint site during synaptic exocytosis[440].

L-type calcium channels are required for neurotransmitter release at IHC synapses where they mediate 90% of calcium current[258,300,441]. Calcium influx in retinal and inner hair cells occurs preferentially beneath synaptic ribbons, where calcium channel cluster[247,258,297,301,317,442,443,443–454]. For example, multiple calcium imaging studies indicate that calcium current "hotspots" localize with synaptic ribbon-specific markers[258,443,455–457]. Additionally, ribbons fail to colocalize to IHC synapses in $Ca_v1.3$ KO mice[278]. These findings further highlight the importance of calcium channels during synaptic development, in which ribbon size and shape in the lateral line of *Danio rerio* is directly shaped by calcium current through $Ca_v1.3$ channels[458]. Indeed, the clustering of calcium channels at AZs is a feature unique to sensory cells and has long been thought to play a role in synchronizing calcium influx with vesicle release[258]. In IHCs, the ribbon may act as an impermeable structure that clusters calcium beneath it as a method physically concentrating calcium[263]. Both *in vivo* and *in vitro* studies have established that synaptic secretion in IHCs occurs between 15-75uM calcium[97,213,429,459–461].

Ribbons is mammalian IHCs associate with 100-200 calcium channels. Further, the probability of the channel being open was estimated to be 0.85[271,279,284,317,462]. If there are roughly 30 AZ/IHC then, assuming calcium channels are evenly distributed between AZs, each AZ should have around 5 calcium channels. This result suggests that only a few calcium channels

need to be open to promote synaptic vesicle exocytosis. These calculations support immunofluorescence and electrophysiology results which suggest that the AZs are surrounded by 3-5 calcium channels[463,464]. For reference, the ribbons synapse of gold-fish bipolar cells contain between 5-7 calcium channels per AZ[308].

The tight clustering of calcium channels at the presynaptic membrane facilitate simultaneous opening of other channels within a small radius of calcium influx current, as well as reducing the time between depolarization and exocytosis thereby reducing synaptic delays[465,466]. The coupling distance between calcium channels and fusion machinery is often probed using calcium chelators that have the same calcium binding affinity but different binding kinetics. If calcium channels are in close proximity to calcium sensors, then the fast chelator, BAPTA, would bind calcium while the slow chelator, EDTA, would not have enough time to interact. By contrast, if coupling distances are longer, then both BAPTA and EDTA would have time to bind calcium. Results of calcium chelation studies in different cell types suggest a wide distribution of distances between calcium channels and calcium sensors. Immature calyx of Held cells have coupling distances between 30 to 300nm while hippocampal cells have a coupling distance of 10-20nm [467,468]. IHCs treated with a fluorescent calcium indicator revealed that calcium influx occurs in "hotspots" spanning hundreds of nanometers termed microdomains. These are different from nanodomains, which only span tens of nanometers[454]. The presence of microdomains would facilitate the fusion of vesicles that are farther away from calcium current[469]. However, exocytosis in response to physiological depolarizations can be facilitated by opening only a few (<10) calcium channels, which is sufficient to create nanodomains[258,317,470–472]. Further, synaptic release in IHCs is graded, and therefore nanodomain coupling would prevent calcium-signal saturation. Indeed, previous studies have demonstrated that a linear relationship exists between calcium influx and neurotransmitter release[271,287,402,444–447]. Additionally, the probability of a calcium channel being open also supports the presence of calcium nanodomains at the presynapse[476]. It's likely a combination of calcium micro- and nanodomains are present at ribbon synapses to allow them to operate in a larger dynamic range[263]. Further, Frank et. al. have proposed that IHCs adjust the number of calcium channels at their synapses[463]. This finding could explain the existence of hetergenous calcium domains that drive different exocytotic rates[477]. Overlapping calcium domains (microdomain) would facilitate

the release of multiple vesicles whereas non-overlapping domains (nanodomains) facilitate the release of a single or very few vesicles[478–481].

1.7 Single-molecule TIRF as a method to study protein function

Single-molecule microscopy experiments offer a complementary perspective to understanding molecular processes. These types of experiments allow scientist to track individual molecules in a biomolecular process to get a clearer insight of the system properties. This is opposed to traditional bulk biochemical assays where the molecules in a given system are averaged together. As a result, single-molecule experimentalist can measure distributions describing certain molecular properties, characterize the kinetics of biomolecular reactions and observe possible intermediates that would be difficult to obtain in bulk experiments.

The two most common single-molecule imaging experimental setups are confocal microscopy and total internal reflection fluorescence (TIRF) microscopy. In confocal microscopy, a laser is focused through the objective lens of a microscope thereby only exciting a small portion of fluorophores. The emission can be split into multiple channels to image many sets of molecules. In TIRF microscopy, an evanescent wave is created that only excites molecules within a few hundred nanometers of the interface. The fluorescence emission is then sent through the objective and is recorded on a CCD camera. A benefit of TIRF over confocal microscopy is a smaller optical section thickness in the z-plane. Confocal methods have a minimum optical section thickness of 600nm, which is considerably more than the 100nm sections typical of TIRFM. As a result, most TIRFM methods have a much higher signal to noise ratio. Since the plasma membrane is only 7-10nm thick, TIRF is ideal for studying fluorophores at the adherent cell surface while minimizing fluorescence from intracellular regions.

1.7.1 Basis and configuration

The physical phenomenon that allows TIRF to work is the generation of a thin-layer illuminated field called an “evanescent wave”. The evanescent wave is generated when a light with an angle of incidence (θ) passes through an interface at an angle large enough that all of the light is totally internally reflected at the surface. The minimum angle for this to occur at, known as the critical angle, is given by Snell’s law (Eq. 1) where η_1 and η_2 are the refractive

indices of the sample and the cover slip, respectively, and θ is the angle of the light source to the normal.

$$\eta_1 \sin\theta_1 = \eta_2 \sin\theta_2 \quad \text{(Eq. 1)}$$

The intensity (I) of the evanescent field decays exponentially with as its distance (z) from the interface increases where I_0 is the intensity of the evanescent field at z=0 (Eq.2). The depth (d) refers to the distance from the coverslip at which the intensity is 37% ($\frac{1}{e}$) of the intensity at I_0.

$$I_z = {I_0}^{-z/d} \quad \text{(Eq. 2)}$$

Therefore, a fluorophore that is closer to the interface will be excited more strongly than a fluorophore that is farther away. The typical depth of an evanescent field ranges from 60-200nm and is affected by several parameters. These include incidence angle, wavelength and the refractive index of both the coverslip and the sample[482–489].

There are two methods for configuring a total internal reflection setup. In prism-type (pTIRF) a prism mediates the light-source interaction with the sample (Figure 1.9). To do so, the prism must be positioned directly on top of the sample chamber thereby creating the largest draw-back of pTIRF; sample accessibility. However, since most pTIRF systems sit on specialized optical "bread-board" tables, this setup allows for a more customized optical emission set-up. The ability to freely adjust mirrors and filters lets the experimenter easily add or subtract light sources and filters. Objective-type TIRF (oTIRF) is the most popular type of TIRF due to its ease of use. In oTIRF, all light propagation occurs though an objective on an inverted microscope. Compared to pTIRF, oTIRF has the fastest learning curve, is safer, and as a result, more convenient. One major drawback of oTIRF is that since the objective must mediate exication and emission photons (Figure 1.10), special precautions must be made to eliminate signal interference. Generally, the use of a suitable dichroic beam splitter is sufficient to reduce the majority of cross-talk. More recently, modified set-ups have been used to remove all interference[490,491].

The most important feature of oTIRF setups is the numerical aperture (NA) of the objective. The NA is a measure of an optical system's ability to gather light and resolve sample

details. When a fluorescent molecule is highly magnified, it resembles a central spot (diffraction disk) surrounded by diffraction rings. The resolving power of the objective, that is the minimum distance (d) that must separate two objects in order to distinguish them from one another, is dependent upon Abbe's law (Eq. 3), in which the wavelength of light used to probe the sample divided twice the NA is proportional to the diffraction limit.

$$d = \frac{\lambda}{2NA} \qquad \text{(Eq. 3)}$$

Since most NA for TIRF objectives are 1.45 or 1.49, then most oTIRF setups can resolve molecules that are as little as 140nm (0.14μm) apart. This number is small compared to most biological cells which range in size from 1μm to 100μm, but large compared to viruses, protein and peptides which average 100nm, 10nm and 1nm, respectively. Using intensity measurements, it's possible to determine the number fluorophores in a given area. Once an isolated fluorophore is targeted, the photons forming the image can be fit to the point-spread-function (PSF) for that given microscope. The PSF characterizes how an, image source appears upon detection and thus varies by microscope setup. The number of individual fluorophores within a given viewing area can be determined with a PSF which allow the reconstruction of oTIRF images with nanometer resolution[488,492–494].

1.7.2 TIRF applications to biological systems

The use of TIRF to study protein localization and spatial dynamics dates back over 30 years ago[495]. For example, the epidermal growth factor (EGF) and its receptor (EGFR) were some of the first interactions visualized using TIRF[496–498]. TIRF has also been used to visualize different types intracellular signaling events. For example, many signal transduction events, especially those across membranes, rely on receptors forming a physical interaction. TIRF assays have been developed to test protein oligomerization and even determine interaction partners[499–504]. Additionally, TIRF has been instrumental in visualizing the recruitment and the spatial distribution of membrane-trafficking and signaling molecules at the plasma membrane[505–507]. In the context of this thesis, endocytotic and exocytotic proteins have particularly benefited from investigation by TIRF. Insight into the formation of vesicles and the proteins involved in the different stages of this dynamic process were gained as a direct result of TIRF measurements[508–

[512]. Events in the opposite direction, endocytosis, are detectable by TIRF, as well. PSF-fitting has been applied to a few different studies that tracked individual secretory vesicles at the plasma membrane[513–516]. Additionally, *in vitro* TIRF assays have been used to characterize the molecular mechanism of different fusion events[125,130,154,168,517–521]. Calcium channel imaging using TIRF has provided information that could not be gained from electrophysiology measurements, alone. The TIRF data not only showed unequal channel distribution, but also a diversity in activation-voltages[522]. The study of cytoskeletal proteins near the plasma membrane using TIRF has led to new insights about the structural proteins that mediate cellular movement and rigidity. For example, information about the directionality of microtubule polymerization, actin dynamics and actin-associated proteins have all had a TIRF component in their discoveries[512,513,523–525]. TIRF also allows for the determination of single-molecule kinetics from an ensemble of molecules near equilibrium. The ability to follow distinct binding and dissociation events allow experimentalist to not only detect discrete states that would be averaged out in bulk ensembles, but to also probe biologically relevant events that range from occurring on the ms timescale (biomolecular reactions) to those to occur over a period of hours (cellular maturation events). The characterization of the kinetic properties of antibody binding has benefited greatly from TIRF and was often the subject of early TIRF kinetic studies[526–532] . Among others include protein folding kinetics and ion-channel gating kinetics[522,533,534].

TIRF is often combined with other techniques to create single-molecule hybrid assays that provide greater insight into the properties of the molecular system at hand. For example, TIRF is often combined with Förster Radius Energy Transfer (FRET) to investigate inter- and intramolecular interactions either within the plasma membrane or via surface-tethered molecules. FRET occurs when excitation energy from a donor molecule is transferred to the acceptor via an induced dipole-dipole interaction between both fluorophores (Figure 1.11). FRET depends on the orientation of the donor and acceptor relative to each other and the distance between the donor and acceptor, known as the Förster radius. The efficiency of energy transfer, E, is given by Eq.4 where R is the distance between the donor and acceptor and R_o is the distance at which 50% of the energy is transferred to acceptor.

$$E = \frac{1}{1+\frac{R^6}{Ro^6}} \qquad \text{(Eq. 4)}$$

FRET can be used to measure distances that range from 10-75Å. Additionally, since efficiency is distance dependent, FRET is often used as a spectroscopic ruler that is capable of detecting minute changes in orientation relative to the donor and acceptor fluorophores. TIRF-FRET has been used extensively to map protein interactions[535–545]. Specifically, the assemblies and interaction partners of dozens ion channels have been characterized using this method. These channels include nicotinic channels, voltage-dependent channels, transient receptor potential channels, large-conductance ion channels and G-protein coupled channels, to name a few[533,546–555]. Besides FRET, photobleaching is the second most common TIRF-hybrid assay. Single-molecule photobleaching is a method of determining the stoichiometry of biocomplexes. Stoichiometry is determined by the number of stochastic bleaching events that result from prolonged, high-intensity exposure from the excitation source. G-protein coupled receptors[496,556–560] and ion channels[561–575] are examples of protein families that have been extensively characterized using single-molecule photobleaching.

1.8 Significance

Congenital hearing loss is a common disorder and over 60 mutations in the sensory hair cell protein, otoferlin, have been linked to pre-lingual deafness. Although otoferlin is essential for hearing, the large size and low solubility of the protein have limited approaches to study its function on a molecular-level. To overcome these challenges, we have developed single-molecule fluorescence assays which have allowed us to quantitatively probe otoferlin function. Based upon our findings, we have shown that otofelrin acts as a calcium-sensitive scaffold for other membrane-fusion proteins at the plasma membrane. The ability to localize fusion proteins at the site of calcium-influx would reduce synaptic delay and allow for rapid neurotransmitter release in response to a sound stimulus. Second, we have directly shown that otoferlin inserts into lipid-bilayers. This finding is significant because insertion into the membrane bilayer has been demonstrated to be a crucial step for mediating the fusion of synaptic vesicles to the plasma membrane.

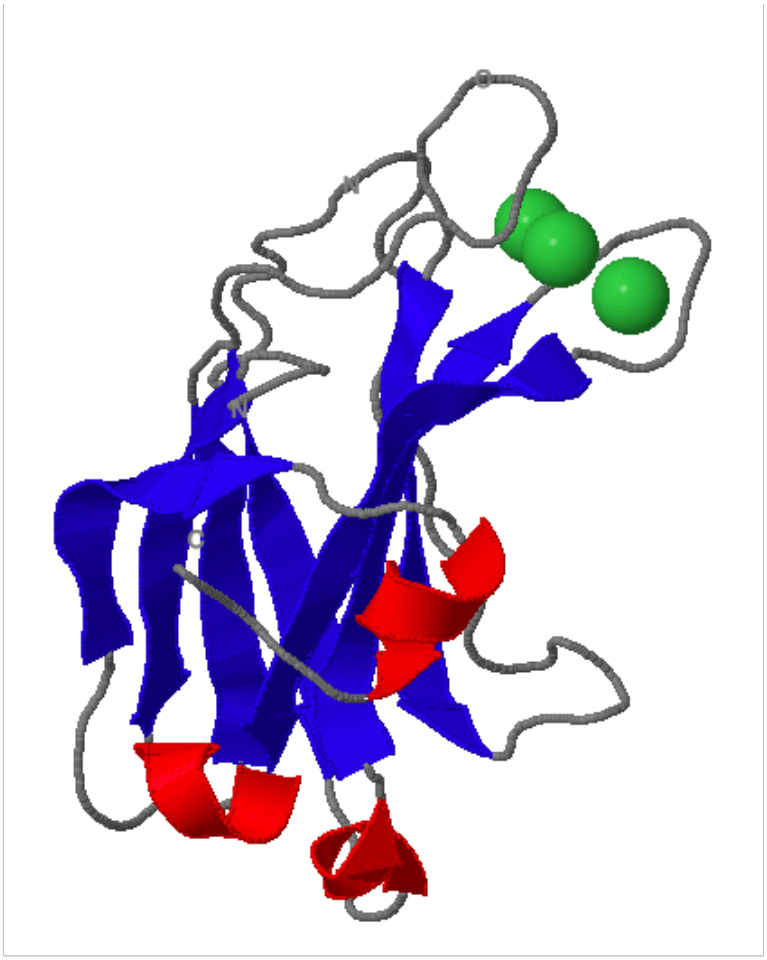

Figure 1.1: A C2 domain
The C2 domain is composed of two, four-stranded β-sheets (blue) that form a β sandwich. Conserved aspartic acid residues on the loops coordinate three calcium ions (green). PDB: 1A25

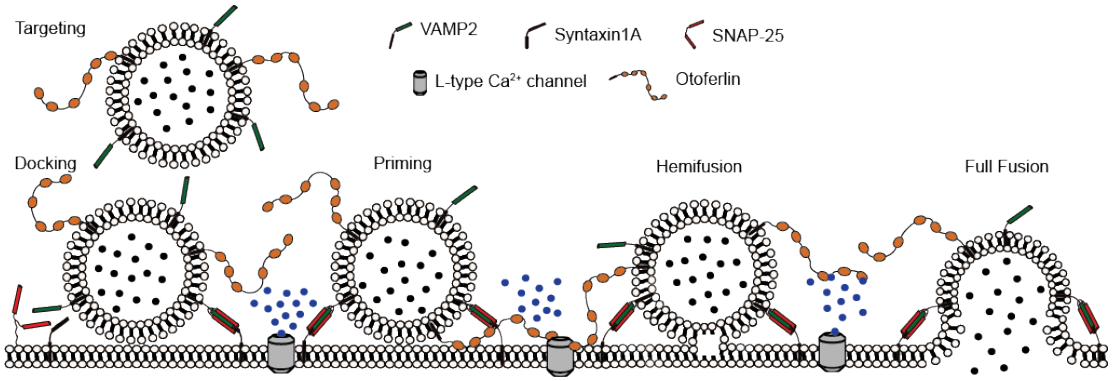

Figure 1.2: Steps of synaptic vesicle fusion
Vesicle fusion is mediated by peripheral and integral membrane proteins that are located on both the plasma membrane and the vesicle. Although each step in the process may not temporally occur as illustrated, all fusion pathways are thought to encompass the same physical mechanism for merging two separate membrane bilayers.

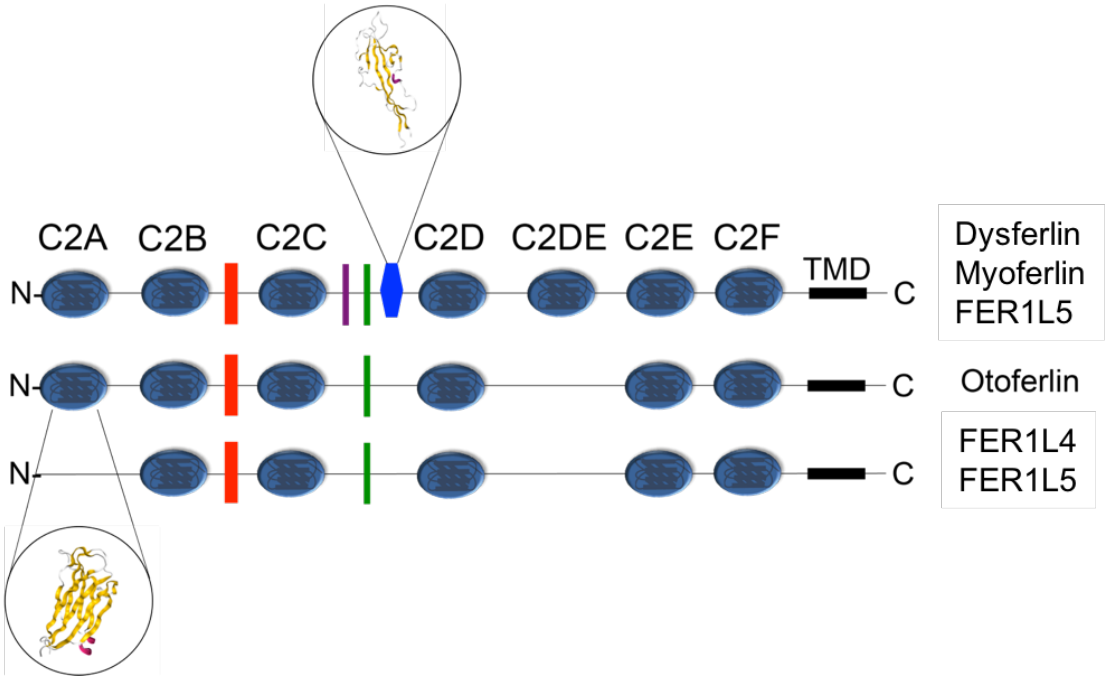

Figure 1.3: Ferlin protein topology
Ferlin proteins contain multiple C2 domains (blue circles). The crystal structure of the otoferlin C2A domain (PBD: 3L9B) shows the canonical C2 domain motif. Mammalian ferlins have a FerI motif (red rectangle) between the C2B and C2C domains and a FerB domain between the C2C and C2D domains. Dysferlin, myoferlin and FR1L5 also have a FerA and DysF (PDB: 4L4H) domain between their C2C and C2D domains.

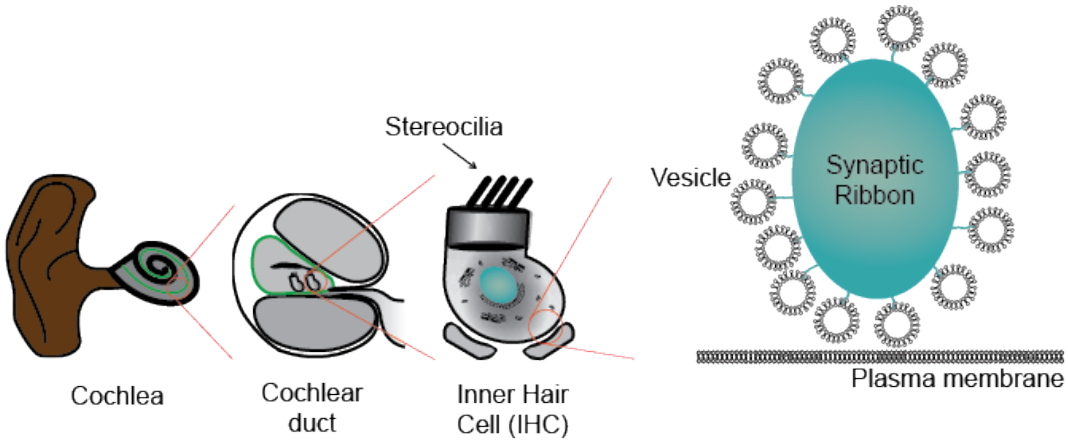

Figure 1.4: IHC plasma membrane
Cartoon illustration of synaptic vesicles tethered to the synaptic ribbon near the plasma membrane of inner hair cells.

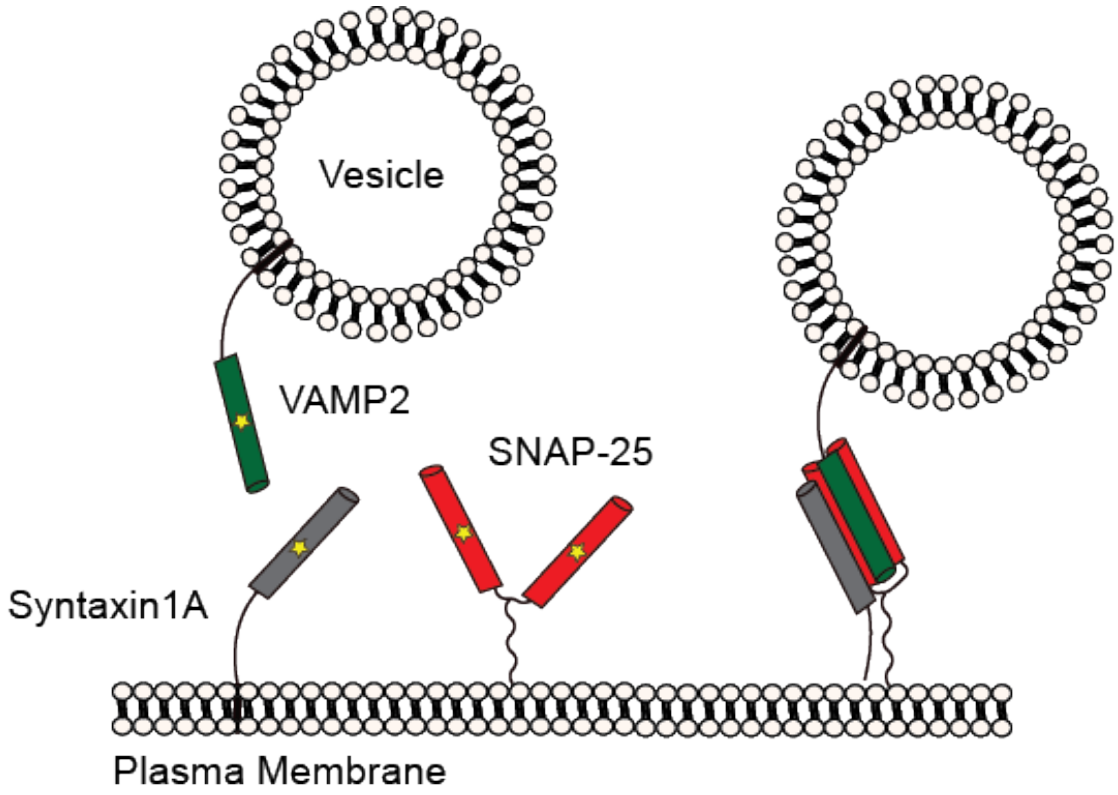

Figure 1.5: Neuronal SNAREs
The neuronal SNAREs syntaxin1A (Qa), SNAP-25 (Qbc) and VAMP-2 (R) form a stable SNAREpin during synaptic vesicle secretion. The helices that contribute to the SNARE core complex are denoted by a yellow star.

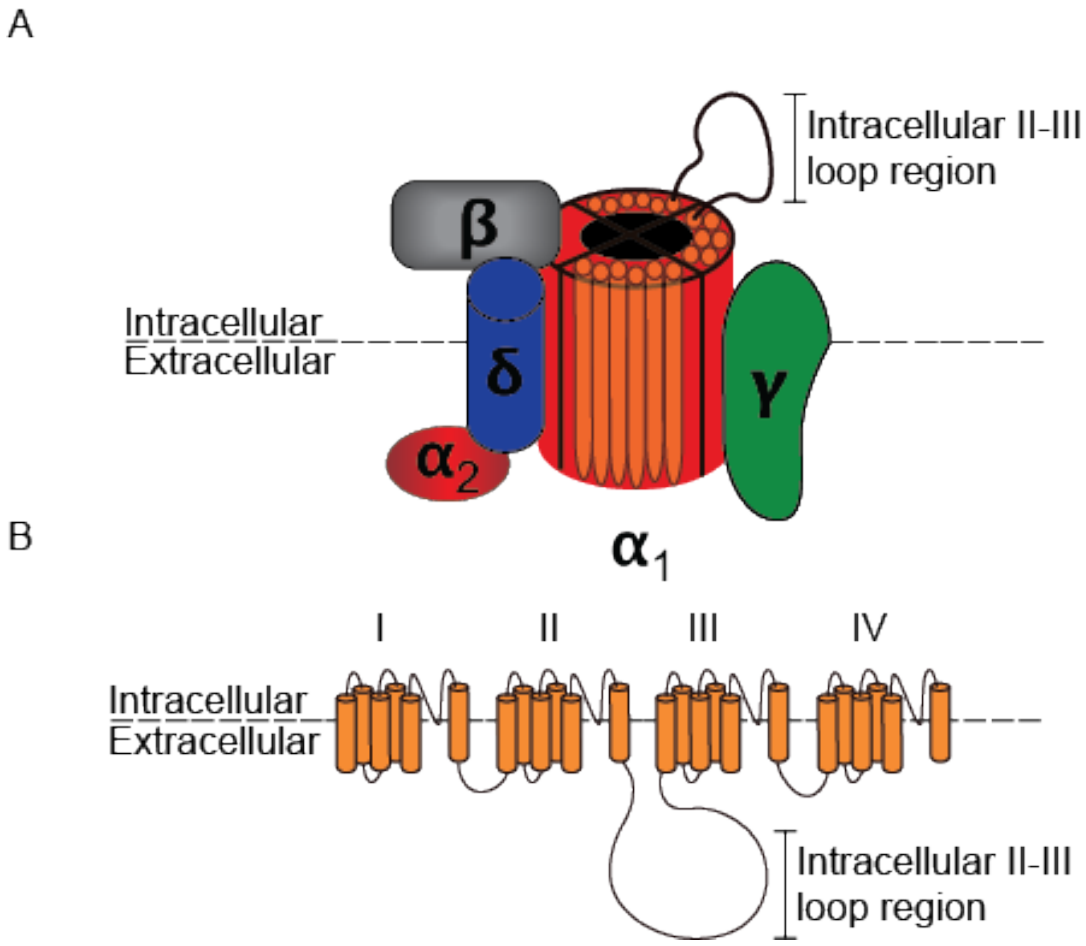

Figure 1.6: Voltage-gated calcium channel
General structure of a voltage gated calcium channel. (A) Schematic showing how all the subunit fit together. (B) Topology of the α1 subunit and their intracellular loops.

Chapter 2

Otoferlin is a multivalent calcium-sensitive scaffold for linking SNAREs and calcium channels

Nicole Hams, Murugesh Padmanarayana, Weihong Qiu, Colin Johnson

Published in *The Proceedings of the National Academy of Sciences* (2017), 114(30), 8023-8028.

© 2017, PNAS.

2.1 Abstract

Sensory hair cells rely on otoferlin as the calcium sensor for exocytosis and encoding of sound preferentially over the neuronal calcium sensor synaptotagmin. Although it is established that synaptotagmin cannot rescue the otoferlin KO phenotype, the large size and low solubility of otoferlin have prohibited direct biochemical comparisons that could establish functional differences between these two proteins. To address this challenge, we have developed a single-molecule colocalization binding titration assay (smCoBRA) that can quantitatively characterize full-length otoferlin from mammalian cell lysate. Using smCoBRA, we found that, although both otoferlin and synaptotagmin bind membrane fusion SNARE proteins, only otoferlin interacts with the L-type calcium channel $Ca_v1.3$, showing a significant difference between the synaptic proteins. Furthermore, otoferlin was found capable of interacting with multiple SNARE and $Ca_v1.3$ proteins simultaneously, forming a heterooligomer complex. We also found that a deafness-causing missense mutation in otoferlin attenuates binding between otoferlin and $Ca_v1.3$, suggesting that deficiencies in this interaction may form the basis for otoferlin-related hearing loss. Based on our results, we propose a model in which otoferlin acts as a calcium-sensitive scaffolding protein, localizing SNARE proteins proximal to the calcium channel so as to synchronize calcium influx with membrane fusion. Our findings also provide a molecular-level explanation for the observation that synaptotagmin and otoferlin are not functionally redundant. This study also validates a generally applicable methodology for quantitatively characterizing large, multivalent membrane proteins.

2.2 Introduction

Sensory hair cells encode sound by converting mechanical motion into chemical signals. Hair cell synapses accommodate this unique functional demand via a set of adaptations that distinguish it from neuronal synapses, including reliance on the L-type calcium channel $Ca_v1.3$ in place of the P- and N-type calcium channels found at most neuronal synapses (Figure 2.1 A and B)[146,234,458,576–578]. During maturation, hair cells also cease expression of the two C2 domain protein synaptotagmin I, which serves as the calcium sensor for neurotransmitter release at neuronal synapses[244]. Although lacking synaptotagmin, mature hair cells express the six C2 domain protein otoferlin, which is proposed to function as the calcium sensor for exocytosis in mature sound-encoding synapses[216]. In agreement with this belief, KO studies have linked

otoferlin to sensory hair cell exocytosis, and in vitro studies on otoferlin have concluded that several C2 domains bind SNARE proteins and stimulate membrane fusion in a calcium-sensitive manner[216,231,234,239]. However, a recent cell-based study concluded that synaptotagmin cannot rescue the otoferlin KO phenotype, arguing against a simple functional redundancy between these C2 domain proteins[250]. The functional differences between synaptotagmin and otoferlin are unclear, however, because of the large size and low solubility of full-length otoferlin, which has prohibited direct comparisons between synaptotagmin and otoferlin. In addition, contradicting conclusions using truncated forms of otoferlin indicate that the activities of the individual domains may not fully recapitulate the activity of the whole protein[233]. A means of functionally characterizing the full-length otoferlin protein as well as conducting more in-depth comparative studies between otoferlin and synaptotagmin would be beneficial to our understanding of the differences between vesicle trafficking events at the synapses of hair cells and neurons.

To address this challenge, we have developed a single-molecule colocalization binding titration assay (smCoBRA) that can quantitatively characterize the entire cytoplasmic region of otoferlin enriched from mammalian cell lysate. Using smCoBRA, we find that both otoferlin and synaptotagmin bind SNARE proteins, with a single otoferlin interacting with up to four SNARE proteins simultaneously. In addition, otoferlin could interact with as many as four $Ca_v1.3$. By contrast, synaptotagmin did not interact with $Ca_v1.3$, highlighting a functional difference between these C2 domain proteins. We also found that otoferlin could interact with both SNARE and $Ca_v1.3$ simultaneously, forming a heterooligomer complex, and that physiologically relevant calcium concentrations alter both the stoichiometry and affinity. Based on our results, we propose a model in which otoferlin, but not synaptotagmin, acts as a calcium-sensitive scaffolding protein that localizes SNARE proteins proximal to the $Ca_v1.3$ calcium channel so as to synchronize calcium influx with membrane fusion.

2.3 Materials and Methods

2.3.1 Plasmid constructs

Mouse otoferlin was provided as a gift from Christine Petit, Institut Pasteur, Paris. Otoferlin amino acids 1–1,885 were amplified via PCR from a PCDNA3 vector and subcloned into the HindIII and BamHI sites of the CKAR vector acquired from Addgene (plasmid 14860). Amino

acids 752–891 of mouse $Ca_v1.3$, corresponding to Loop1.3, were amplified and subcloned into pGEX6p3 (GE Healthcare BioSciences) using restriction sites BamHI and XhoI. Similarly, mCherry-Loop1.3 was created by first subcloning mCherry plus a 30-nt 3′ linker, supplied by Addgene (plasmid 29722), into CKAR via HindIII and KpnI sites and then subsequently subcloning Loop1.3 amino acids 752–891 into the KpnI and XbaI sites via PCR. All constructs were confirmed using DNA sequencing

2.3.2 Protein purification and fluorescent labeling

Both recombinant Loop1.3 and Loop1.3-mCherry were expressed similarly at 18 °C overnight in BL21(DE3) cells after being induced with β-D-1-thiogalactopyranoside (IPTG) at OD_{600} = 0.6. The cells were sonicated on 50% duty cycle for 3 min in Hepes (50 mM Hepes, pH 7.5, 150 mM NaCl), 1 mM PMSF, 1 mM Aprotinin, 1 mM Leupetin, and 0.5% Triton X-100. After centrifugation at 9,000 × g for 20 min at 4 °C, the soluble lysate was incubated for 1 h in GST resin at 4 °C with rotation. Fractions were eluted from the resin using Hepes supplemented with 200 mM reduced glutathione after being washed twice with wash buffer containing Hepes and 2 mM reduced glutathione. The eluted volume was dialyzed overnight at 4 °C in Hepes followed by GST tag cleavage at 4 °C for 2 h with PreScission Protease (GE Healthcare BioSciences) per the manufacturer's instructions. Loop1.3 was collected as flow-through after incubation with GST beads for 1h at 4 °C with rocking. The A_{280} concentration of the protein was measured using a Nanodrop 2000 UV-Vis Spectrophotometer (Thermo) and a predicted extinction coefficient of 2,980 M^{-1} cm^{-1}. AlexaFluor568 or Alexa647 conjugation to Loop1.3, Alexa405 conjugation to the t-SNARE, and Alexa647 conjugation to synaptotagmin were conducted as described previously and directed by the product instructions (Life Technologies)[196]. Degree of labeling was determined as directed by the product instructions. Excess dye was removed via PD-10 desalting columns (GE Healthcare BioSciences), and all fractions were assayed for purity using SDS/PAGE. Pure fractions were stored in small aliquots at −80 °C.

2.3.3 Cell culture and transfection

HEK293 cells were grown in DMEM supplemented with 10% FBS and Pen Strep (5,000 U/mL and 5,000 µg/mL, respectively) and incubated at 37 °C with 5% CO_2. Cells were cultured to 90% confluence (visually verified) before being transfected with 1 µg of YFP-otoferlin or

Loop1.3-mCherry vector. Cells were transfected with calcium chloride in the presence of 50 mM N,N-bis[2-hydroxyethyl]-2-aminoethanesulfonic acid (BES), 280 mM NaCl, and 1.5 mM Na_2HPO_4. Cells were harvested 72 h posttransfection by scraping the culture dish in buffer containing PBS, pH 7.5, 2% octylglucoside, and a protease inhibitor mixture (Roche). The cells were then sonicated for 2 min in 10-s intervals. Soluble protein was recovered via centrifugation at 9,000 × g for 15 min at 4 °C. For coimmunoprecipitation, the lysis buffer lacked octylglucoside and included 50 mM Hepes, 120 mM NaCl, 1% Nonidet P-40, 1 mM EDTA, and a protease inhibitor mixture.

2.3.4 Co-immunoprecipitation

Protein A/G MagBeads (GeneScript) were equilibrated in PBS, pH 7.5, and conjugated to 1 µg of anti-GFP antibody (Abcam) by rotational mixing for 1 h at room temperature. Beads were washed once with PBS to remove excess antibody and washed twice with 0.2 M triethanolamine, pH 8.2. Beads were resuspended in 20 mM dimetyl pimelimidate dihydrochloride in 0.2 M triethanolamine, pH 8.2, and rotated for 30 min at room temperature. To terminate the antibody cross-linking reaction, the beads were suspended in 50 mM Tris · HCl, pH 7.5, and again rotated at room temperature for 30 min. Beads were subsequently washed three times in PBS, pH 7.5. HEK293 cell lysate from one T75 transfected with YFP-otoferlin and mCherry-Loop1.3 was added and left to rotate overnight at 4 °C. The reaction was washed twice in PBS, pH 7.5, to remove nonspecific binding before the beads were suspended in nonreducing sample buffer and incubated at 90 °C for 5 min. Samples were briefly spun down and analyzed using SDS/PAGE.

2.3.5 GST Pulldown

The pGEX6P3 containing GST, GST-Loop1.3, and pMCSG9 vectors containing the otoferlin C2ABC and C2DEF domains were transformed into BL21 Escherichia coli cells. The bacterial culture (OD_{600} = 0.6) was induced for 12 h at 18 °C with 1 mM IPTG. Cells were pelleted at 4,000 rpm and resuspended in lysis buffer containing 40 mM Hepes, pH 7.5, 200 mM NaCl, and 1 mM DTT. The cells were lysed by sonication in lysis buffer containing protease inhibitors (1 mM PMSF, 1–2 µg/mL aprotinin, leupeptin, pepstatin A). The soluble fraction of GST and GST-$Ca_v1.3$ II–III loop lysate was incubated with Glutathione resin for 2h at 4 °C, and the resin was

washed with lysis buffer before the bound protein was eluted with elution buffer containing 40 mM Hepes, pH 7.5, 200 mM NaCl, and 1 and 200 mM reduced glutathione. While MBP-C2ABC and MBP-C2DEF domains of otoferlin lysate were incubated with nickel-nitrilotriacetic acid (Ni-NTA) resin for 2h at 4 °C, the resin was washed with lysis buffer and then eluted with elution buffer containing 40 mM Hepes, pH 7.5, 200 mM NaCl, 1 mM DTT, and 500 mM Imidazole. Purified proteins were extensively dialyzed in buffer containing 40 mM Hepes, pH 7.5, 200 mM NaCl, and 1 mM DTT and concentrated using an Ultrafree-10 centrifugal filter unit (Pall Corporation). Protein concentrations were determined by UV absorbance at 280 nm.

The GST-Loop1.3 and GST protein were incubated with Glutathione-Sepharose beads (50 µL of a 50% slurry) for 1h at 4 °C and washed with lysis buffer (40 mM Hepes, pH 7.5, 150 mM NaCl, 1 mM DTT, protease inhibitor mixture). Then, MBP-C2ABC (5 µM) and C2DEF (5 µM) domains were mixed with washed beads of GST and GST-Loop1.3 and incubated for 2h at 4 °C with either 200 µM EDTA or calcium followed by centrifugation for 2 min at 1,000 × g. The beads were washed three times in the lysis buffer with either 200 µM EDTA or calcium, and the GST-Sepharose beads were heat-denatured at 95 °C for 5 min in SDS sample buffer and analyzed by SDS/PAGE. GST protein was used as a negative control. The amount of MBP-ABC and MBP-DEF domains bound to GST-Loop1.3 loop was quantified by densitometry.

2.3.6 TIRF and photobleaching measurements

Coverslips were functionalized with PEG-Biotin. Flow cells were assembled by attaching a functionalized coverslip to glass slides layered with a 0.24-mm double-sided adhesive sheet (Grace Bio-Labs) and epoxy resin. For all TIRF experiments, biotinylated 6xHis, RFP (Abcam), or YFP antibodies were tethered to coverslips via streptavidin. To accomplish this surface chemistry, flow cells were first hydrated in Hepes for 4 min and then successively incubated for 2 min in 0.1 mg/mL streptavidin and 15 nM biotinylated antibody. After rinsing off excess antibody, HEK293 cell lysate containing otoferlin-YFP was incubated in the flow cells for 2 min before being washed with Hepes buffer supplemented with 0.4% glucose, 45 µg/mL catalase, and 0.2 U glucose oxidase (HOXS buffer). For all smCoBRA measurements, titrant dilutions made in HOXS buffer were flowed over the immobilized protein and allowed to incubate inside the flow chamber for 3 min at room temperature before an image was captured. Single- and multiwavelength TIRF imaging was performed using a Zeiss TIRF3 laser system. To reduce

fluorescent bleed-through, TIRF filter set 46 (Zeiss) was used for YFP imaging, and filter set 72 was used for mCherry and AlexaFluor568 imaging. During measurements, focus was maintained using definite focus provided by Zen Imaging Software (Zeiss). For single-molecule photobleaching experiments, HOXS buffer was omitted, and images were acquired every insert switching time at 85% laser power, resulting in >90% photobleaching within the range of the TIRF field. Three-color colocalization studies were performed with Alexa405-labeled syntaxin 1/SNAP-25 SNAREs, Alexa647-labeled Loop1.3, and otoferlin-YFP.

2.3.7 Analysis of smCoBRA measurements

All TIRF images were analyzed using ImageJ software (NIH). Before analysis, the background was subtracted using the standard background subtraction tool. For each concentration, colocalized puncta were validated using Pearson's coefficient and used to construct a binding saturation curve. Binding affinities, curve fitting, and other statistical analysis were performed using customized Matlab scripts.

2.3.8 Analysis of photobleaching measurements

After background correction, the intensity of the region of interest was calculated frame by frame using ImageJ. Individual photobleaching steps were assigned by visual analysis of graphs representing puncta intensity as a function of time. Total subunit frequencies were fit to both Poisson and binomial distributions.

2.3.9 Circular Dichroism

CD experiments were conducted on a JASCO 715 spectropolarimeter at 25 °C. Before data collection, samples were dialyzed against 10mM potassium phosphate and 100mM sodium fluoride buffer, pH 7.4, and then equilibrated at room temperature for 16h.

2.4 Results

2.4.1 Multiple $Ca_v1.3$ proteins bind otoferlin simultaneously

A recently reported yeast two-hybrid screen suggested that otoferlin may interact with a cytoplasmic loop located between domains II and III of $Ca_v1.3$ composed of amino acids 752–891(referred to as Loop1.3)[234]. To establish whether otoferlin interacts with Loop1.3, we

conducted an immunoprecipitation assay using lysate from HEK293 cells cotransfected with mCherry-Loop1.3 and a YFP-otoferlin (otoferlin amino acids 1–1,885) using an anti-YFP antibody. After first verifying by Western blot that the antiotoferlin antibody specifically immunoprecipitated otoferlin, we subsequently probed immunoprecipitated samples and found that mCherry-Loop1.3 coimmunoprecipitated with YFP-otoferlin (Figure 2.2 A and B). By contrast, mCherry-Loop1.3 did not immunoprecipitate in samples lacking YFP-otoferlin. Furthermore, immunoprecipitation of YFP from cells cotransfected with YFP and mCherry-Loop1.3 did not coimmunoprecipitate mCherry-Loop1.3 (Figure 2.2 A and B). We also tested for otoferlin–Loop1.3 interaction using a GST pulldown assay with otoferlin constructs composed of either the first three C2 domains (C2ABC) or the last three domains (C2DEF). When tested, GST-Loop1.3 was found to bind to both otoferlin constructs, whereas GST alone did not interact with either otoferlin construct (Supplemental Figure 2.1). Based on these results, we conclude that otoferlin specifically interacts with the cytoplasmic loop of $Ca_v1.3$.

2.4.2 Single-molecule studies of otoferlin-Loop1.3 interactions

Although requiring low amounts of sample, coimmunoprecipitation assays and GST pulldowns cannot provide accurate affinity or stoichiometric binding information. By contrast, other more quantitative techniques require prohibitively high sample concentrations. To overcome these challenges, we developed a total internal reflection fluorescence microscopy (TIRFM)-based single-molecule colocalization binding titration method that we applied to quantitatively probe the interaction between Loop1.3 and YFP-otoferlin derived from transfected HEK293 cells. As depicted in Figure 2.2C, the design principle involves immobilizing YFP-otoferlin onto a glass coverslip using a YFP antibody conjugated to a PEG-biotin surface[504,579]. This immobilization scheme orients the protein in a biomimetic manner and leaves the protein free to bind ligands. After extensive washing of the surface to remove nonspecifically bound cell lysate components, fluorescent puncta corresponding to YFP-otoferlin were observed, and subsequent stepwise titration of fluorescently tagged Loop1.3 resulted in colocalized puncta because of interaction between otoferlin and Loop1.3. Given that intracellular calcium concentrations in sensory hair cells can vary from less than 1 to over 30 μM, we conducted Loop1.3 titrations in the presence of 0.1, 1, 15, 30, and 50 μM free calcium. Incubation times adequate for reaching equilibrium were given for each concentration tested as

determined by an invariant number of colocalized puncta over time at a given concentration. When titrated, an increasing number of colocalized Loop1.3-otoferlin puncta were observed that reached a maximum percentage colocalization at Loop1.3 concentrations of 10 μM (Figure 2.2D). At this concentration, >90% of the YFP-otoferlin puncta colocalized with Loop1.3 (Supplemental Figure 2.2). The resulting colocalization data were fit to a Langmuir isotherm equation, and the best fit of the data indicates a 30-fold change in the K_d value (from 0.04 ± 0.02 to 1.14 ± 0.07 μM) when the free calcium concentration increased from 0.1 to 50 μM. Colocalization between otoferlin and Loop1.3 was further verified through calculation of Mander's coefficients, M1 and M2 (Figure 2.2E)[580]. As expected, M1, which represents the analyte (otoferlin) channel colocalization coefficient, was found to increase over the course of the titrations, whereas M2, which represents the colocalization coefficient for the titrant (Loop1.3), remained at ~1 and did not significantly change. To ensure that colocalization was not caused by Loop1.3 interaction with YFP, we immobilized YFP at surface densities similar to YFP-otoferlin surface densities (Supplemental Figure 2.3) and titrated Loop1.3. We found no colocalization between Loop1.3 and YFP to the limit of the Loop1.3 concentrations (50μM) tested.

2.4.3 Synaptotagmin does not interact with the cytoplasmic loop of $Ca_v1.3$

At conventional neuronal presynapses, synaptotagmin I binds both the syntaxin1/SNAP-25 neuronal SNARE heterodimer and the intracellular loop connecting domains II and III of N-type calcium channels, serving as a direct link between calcium influx and neurotransmitter release (Figure 2.1)[146,581]. This region of N-type channels is analogous to Loop1.3. To test whether synaptotagmin interacts with Loop1.3, we immobilized a recombinant form of synaptotagmin at surface densities similar to those of the otoferlin samples (Supplemental Figure 2.3) and titrated fluorescently labeled Loop1.3 (Figure 2.2F). We found that Loop1.3 did not colocalize with synaptotagmin to the limit of the Loop1.3 concentrations tested, regardless of calcium concentration (Figure 2.2F). In agreement with previous studies, however, we found that immobilized synaptotagmin did colocalize with the intracellular loop connecting domains II and III of $Ca_v2.2$ (Figure 2.2G). This interaction was found to be calcium-sensitive, with a K_d of 1.06 ± 0.03 μM at 0.1 μM calcium and 0.10 ± 0.03 μM at 50 μM calcium. Thus, although synaptotagmin binds the loop spanning domains II and III in N-type channels, it does not appear

to interact with the loop connecting domains II and III in L-type channels, suggesting that otoferlin and synaptotagmin differ in their calcium channel binding specificity.

2.4.4 Multiple otoferlin C2 domains mediate interaction with Loop1.3

To determine the stoichiometry of the otoferlin–Loop1.3 interaction, we conducted single-molecule photobleaching assays on heteromers composed of YFP-otoferlin complexed with mCherry-Loop1.3[582]. mCherry is thought to be monomeric, and for our studies, we assume that the mCherry is properly folded and mature. We first measured the bleaching of YFP-otoferlin puncta and found that the majority (60%) of the observed YFP-otoferlin bleaching events were single step. However, a small number of two- and three-step bleaching events was detected, which may represent otoferlin oligomers or closely spaced monomers. To simplify interpretation, we choose only puncta with a single YFP-otoferlin bleaching step for study of otoferlin–Loop1.3 stoichiometry. Analysis of otoferlin–Loop1.3 colocalized puncta revealed one, two, and three Loop1.3 bleaching steps for a given single YFP-otoferlin in the presence of 1 mM EDTA (mean steps = 2.36; SD = 0.76; n = 2,300) and an increase in both the number of four-step bleaching events (mean steps = 2.49; SD = 1.12; n = 2,300) in the presence of 200 μM free calcium (Figure 2.3)[583].

To identify the regions of otoferlin that mediate the interaction with Loop1.3, we repeated the smCoBRA measurements with individual C2 domains of otoferlin fused to YFP (Figure 2.4). We found that YFP-tagged C2C and C2E domains did not colocalize with Loop1.3, regardless of Loop1.3 or calcium concentration. However, YFP-conjugated C2A, C2B, and C2D bound Loop1.3 at all calcium concentrations tested (from 0.1 to 50 μM). Interaction between the C2F domain and Loop1.3-mCherry was only detected in the presence of calcium concentration above 1 μM (Figure 2.4D). To determine the stoichiometry of individual C2 domain–Loop1.3 interactions, we conducted single-molecule photobleaching assays on YFP-C2 domain and Loop1.3-mCherry complexes. Analysis of colocalized puncta revealed a single calcium-independent Loop1.3-mCherry bleaching step per single YFP-C2 domain for C2A, C2B, and C2D and a single calcium-dependent bleaching step for C2F, corroborating our observations of four Loop1.3 bleaching steps with the longer otoferlin construct. We conclude that four C2 domains can interact with Loop1.3, with the C2F domain interacting with Loop1.3 in a calcium-sensitive manner.

2.4.5 Otoferlin can bind Loop1.3 and SNAREs simultaneously

At neuronal presynapses, synaptotagmin I binds the syntaxin1/SNAP-25 neuronal soluble NSF attachment protein receptor (t-SNARE) heterodimer and functions as a calcium sensor for neurotransmitter release[146,231]. Although it is not completely clear which SNAREs drive exocytosis in sensory hair cells, previous studies have shown that the individual C2 domains of otoferlin bind the t-SNARE heterodimer[231,234]. However, no study has tested whether full-length otoferlin can bind multiple t-SNARE heterodimers or whether otoferlin can bind Loop1.3 and SNAREs simultaneously. To address this gap in our knowledge, we first verified the otoferlin–SNARE interaction using smCoBRA. When tested, a fluorescently labeled t-SNARE heterodimer colocalized with surface-immobilized YFP-otoferlin. Binding was determined to be calcium-sensitive, with an apparent K_d of 5.27 ± 0.04 μM at 0.1 μM and 0.17 ± 0.02 μM at 30 μM free calcium based on the best fit to a Langmuir equation (Figure 2.5A). Colocalization between otoferlin and the SNARE heterodimer was validated by calculation of Mander's coefficients M1 and M2 (Figure 2.5B). No significant colocalization was observed between SNARE heterodimer and surface-immobilized YFP, despite similar densities to YFP-otoferlin (Figure 2.5C), suggesting that otoferlin mediates the interaction with the SNARE heterodimer. Analysis of photobleaching measurements on otoferlin–SNARE complexes indicates that one otoferlin interacts with multiple t-SNAREs (Figure 2.5D and E). We also tested for synaptotagmin–t-SNARE interaction and found that, in agreement with previous studies, immobilized synaptotagmin bound t-SNAREs with an affinity of 0.29 μM at 50 μM calcium (Supplemental Figure 2.4), similar to the submicromolar affinity reported previously[584].

To determine the C2 domains of otoferlin responsible for the observed otoferlin–SNARE interaction, the SNARE heterodimer was titrated against each individual YFP-C2 domain. C2A, C2B, C2C, and C2E were found to colocalize with the t-SNARE heterodimer in a calcium-enhanced manner, whereas the C2F domain colocalized with the heterodimer only in the presence of greater than 1 μM free calcium. Best fits to a Langmuir equation yielded binding constants listed in Table 2.1.

Although traditional techniques, including isothermal titration calorimetry and fluorescence anisotropy, can quantitatively characterize interactions in two-component systems, these techniques are not well-suited to measure three-component interactions. The ability to visualize three-color colocalization with smCoBRA distinguishes itself from these more

traditional assays, and having established that otoferlin directly interacts with t-SNAREs and Loop1.3, we next sought to determine if binding occurs simultaneously or competitively through three-color colocalization. To test for simultaneous binding, we titrated Alexa647-Loop1.3 onto complexes composed of immobilized YFP-otoferlin bound to Alexa405 t-SNAREs (Figure 2.6A). Alternatively, we titrated the t-SNARE heterodimer onto complexes composed of immobilized otoferlin bound to Loop1.3 (Figure 2.6B). To ease interpretation, the titrations were conducted with a constant concentration of the ligand that composed the starting complex at near-saturating levels (2 μM Loop1.3 during t-SNARE titrations and 2 μM t-SNARE during Loop1.3 titrations). Regardless of the order, we found that Loop1.3/otoferlin/SNARE complexes could be formed in a dose-dependent manner as determined by colocalization of three distinct fluorophores, indicating that Loop1.3 and SNAREs can bind otoferlin simultaneously. Colocalization was validated by determination of Mander's colocalization coefficients (Supplemental Figure 2.6). To test for calcium sensitivity, titrations were conducted at several calcium concentrations (0.1–50 μM), and the best fit parameters are reported in Table 2.2. No colocalization was detected when Alexa647-Loop1.3 was titrated onto samples containing immobilized Alexa405–t-SNARE, indicating that Loop1.3 does not interact with t-SNAREs. Figure 2.6 shows a comparison of the dissociation constants for ligand binding separately (Figure 2.6C) or simultaneously to otoferlin (Figure 2.6D) as a function of calcium.

2.4.6 The otoferlin L1011P pathogenic point mutation abrogates binding between C2D and Loop1.3

Mutations in otoferlin that prevent neurotransmitter release from sensory hair cells result in a form of nonsyndromic hearing loss known as DFNB9[214,585]. One such pathogenic mutation in humans is L1011P in the C2D domain (L1010P in mouse), which has recently been shown to diminish binding to Loop1.3[234]. To better understand how this mutation affects otoferlin and further test smCoBRA, we used site-directed mutagenesis to introduce the L1010P point mutation into our YFP-otoferlin construct (otoferlin$_{L1010P}$). We found that immobilized otoferlin$_{L1010p}$ required greater concentrations of mCherry-Loop1.3 to reach saturation and bound with diminished affinity relative to WT otoferlin (Figure 2.7A; K_d values are listed in Table 2.2), despite immobilization surfaces densities similar to WT YFP-otoferlin (Supplemental Figure 2.3). In addition, the mean number of mCherry-Loop1.3 photobleaching steps was reduced in

the mutant compared with the WT in EDTA (WT mean = 2.36; SD = 0.76; otoferlin$_{L1010p}$ mean = 1.57; SD = 0.57; $P < 0.01$) and 200 μM free calcium (WT mean = 2.49; SD = 1.12; otoferlin$_{L1010p}$ mean = 1.88; SD = 0.77; $P < 0.01$) (Figure 2.7B and C). We also found that samples composed of otoferlin$_{L1010P}$–t-SNARE complexes had a reduction in the mean number of t-SNARE photobleaching events, indicating that the mutation attenuates SNARE binding (Supplemental Figure 2.7).

The loss in binding affinity and reduction in stoichiometry suggest that the L1010P mutation abrogates the C2D–Loop1.3 interaction. We, therefore, tested a single C2D domain mutant YFP-C2D$_{L1010P}$ for interaction with Loop1.3 or t-SNAREs. When tested, we found that the point mutation abrogated colocalization of the C2D domain with both the Loop1.3 and the t-SNARE heterodimer (Figure 2.7D and E). Lastly, to test whether the L1010P mutation resulted in loss of structure, we collected CD spectra of WT and C2D$_{L1010P}$ constructs (Figure 2.7F). Both spectra displayed a minimum between 200 and 210 nm.

2.5 Discussion

Otoferlin plays an essential role as a calcium-sensitive regulator of exocytosis in sensory hair cells; however, the mechanism of otoferlin activity is currently unknown. The results of our studies indicate that otoferlin is a multivalent protein capable of binding multiple copies of the cytoplasmic loop of $Ca_v1.3$ and SNARE proteins simultaneously (Figure 2.6). This interaction seem to be mediated by the C2 domains of otoferlin. Previous studies that we have conducted showed that the C2 domains of otoferlin bind calcium and PI(4,5)P_2 lipids[47,196,239,455]. We, therefore, propose a model where vesicle-associated otoferlin acts as a scaffolding protein that first targets the presynaptic membrane via interaction with PI(4,5)P2 and subsequently interacts with calcium channels and membrane fusion machinery (one or more SNARE isoforms). The linking of the synaptic vesicle, presynaptic calcium channel, and membrane fusion proteins in close spatial proximity would reduce the "reaction space" and increase the fidelity and precision of exocytosis in response to presynaptic calcium influx. Our observation that multiple C2 domains interact with $Ca_v1.3$ suggests that some C2 domains may be somewhat functionally redundant. Indeed, it was reported that exogenous truncated forms of otoferlin lacking one or more C2 domains could rescue balance and startle reflex in zebrafish lacking endogenous

otoferlin[232]. This observation may be explained if the truncated otoferlin constructs retained at least one C2 domain capable of binding $Ca_v1.3$.

We found that the neuronal synaptic calcium sensor synaptotagmin I interacted with the loop II–III region (synprint) of $Ca_v2.2$, in agreement with previous reports (Figure 2.2G). Unexpectedly, however, synaptotagmin I did not interact with the loop II–III (Loop1.3) region of $Ca_v1.3$ (Figure 2.2F). The loop II–III region of voltage-gated calcium channels is thought to contribute to exo- and endocytotic processes through direct interaction with synaptic proteins. We speculate that the inability of synaptotagmin I to rescue the otoferlin KO phenotype may be caused by the loss of interaction between $Ca_v1.3$ and the synaptic vesicle calcium sensor. Another important distinction between otoferlin and synaptotagmin is that the synaptotagmin–$Ca_v2.2$ interaction is reported to be mediated solely by the C2B domain in a 1:1 ratio, whereas multiple otoferlin C2 domains can interact with the II–III loop region of $Ca_v1.3$ (Figure 2.4). Although it is thought that otoferlin does not influence channel activity, the characteristics of exocytosis proximal to the channel may be influenced by the biophysical properties of a given C2 domain and how many domains are bound to channels. In our studies, we also found that calcium increased the binding affinity of synaptotagmin for the loop region of $Ca_v2.2$, whereas calcium decreased slightly but significantly the affinity between otoferlin and Loop1.3.

In characterizing otoferlin, we developed the smCoBRA method, which quantitatively characterizes multicomponent heteromeric complexes. This method both allows for measurement of the multivalence, stoichiometry, and binding affinities of large multidomain proteins and is compatible with the small amounts of protein produced from mammalian cell culture. A distinguishing capability of smCoBRA is the ability to colocalize three fluorescently conjugated proteins simultaneously, titrate one of the proteins onto a complex of the other two, and obtain dissociation constants. smCoBRA is generally applicable and therefore, a viable method to interrogate proteins that are not obtainable at high concentrations.

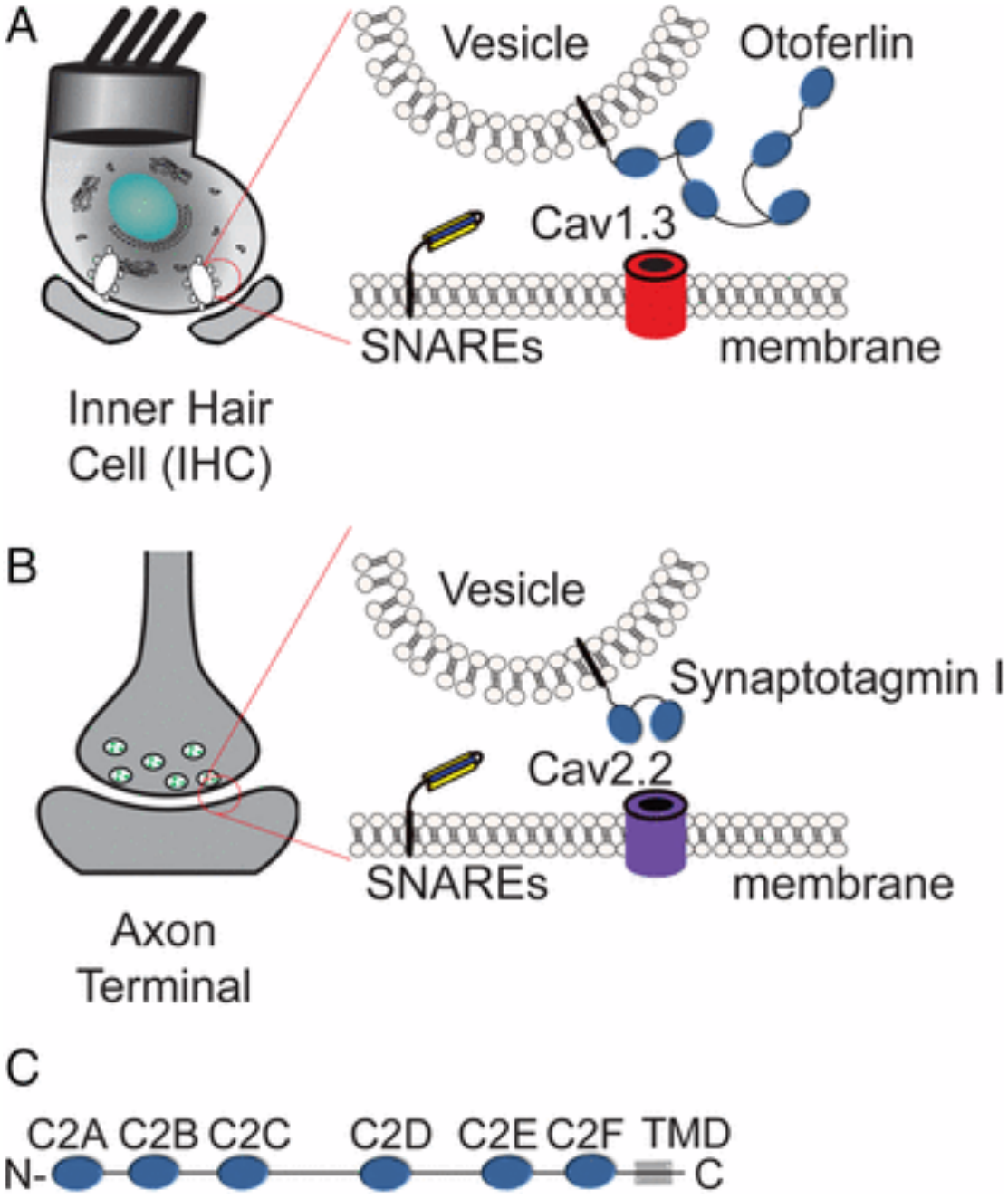

Figure 2.1: Schematic of sensory cell and neuronal presynapses
Schematic of sensory hair cell and neuronal presynapses. (A) Synaptic ribbons within the sensory hair cells of the cochlea position synaptic vesicles proximal to the presynaptic membrane. Otoferlin resides on synaptic vesicles, whereas Cav1.3 localizes to the presynapse. (B) The synaptic vesicles of neurons typically harbor synaptotagmin I/II and an N- or P-type calcium channel (Cav2.1 or Cav2.2). (C) Diagram of otoferlin depicting six C2 domains, labeled C2A–C2F, and the transmembrane domain (TMD).

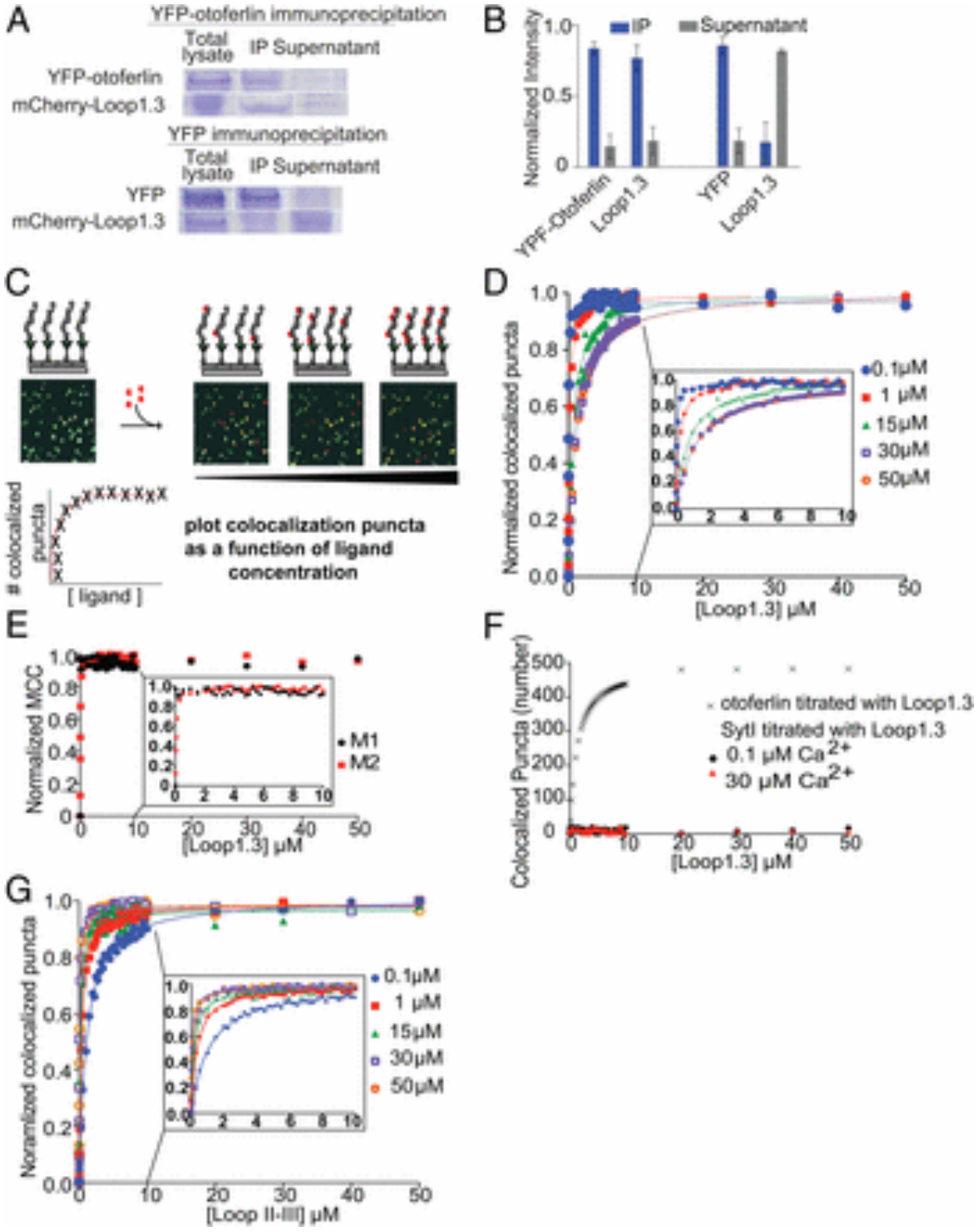

Figure 2.2: Otoferlin Interacts with Loop1.3
Otoferlin interacts with Loop1.3. (A, Upper) Representative SDS/PAGE showing results of immunoprecipitation of otoferlin from lysate of HEK293 cells cotransfected with YFP-otoferlin and mCherry-Loop1.3. Both otoferlin and Loop1.3 precipitate. (A, Lower) Representative SDS/PAGE showing results of immunoprecipitation of YFP from lysate of HEK293

cotransfected with YFP and mCherry-Loop1.3. YFP but not Loop1.3 precipitates. IP, immunoprecipitated pellet; total lysate, lysate before immunoprecipitation. (B) Quantitation of coimmunoprecipitation showing the fraction of each protein in the IP and supernatant (n = 3 biological replicates; error = SE). (C) Cartoon depicting smCoBRA. Titration of a fluorescently labeled ligand onto immobilized YFP-otoferlin results in colocalized fluorescent puncta. The resulting saturation curve is fitted to obtain a dissociation constant K_d. (D) Dose–response for YFP-otoferlin titrated with Loop1.3 at increasing concentrations (0.1–50 μM) of free calcium. Each data point represents the mean of three biological replicates (n = 3). Experimental data are fit with a Langmuir isotherm (solid lines). Inset depicts 0–10 μM for clarity. (E) Determined Mander's colocalization coefficients M1 (black) and M2 (red) for a dose–response of Loop1.3 titrated onto YFP-otoferlin (0.1 μM calcium). Inset depicts 0–10 μM. (F) Dose–response for immobilized synaptotagmin I titrated with Loop1.3 in the presence of 0.1 or 30 μM calcium (n = 3). Colocalization between Loop1.3 and YFP-otoferlin is included for comparison. (G) Dose–response for immobilized synaptotagmin I titrated with the loop II–III region of Cav2.2 in in the presence of 0.1–50 μM calcium (n = 3). Inset depicts 0–10 μM for clarity. MCC, Mander's correlation coefficients.

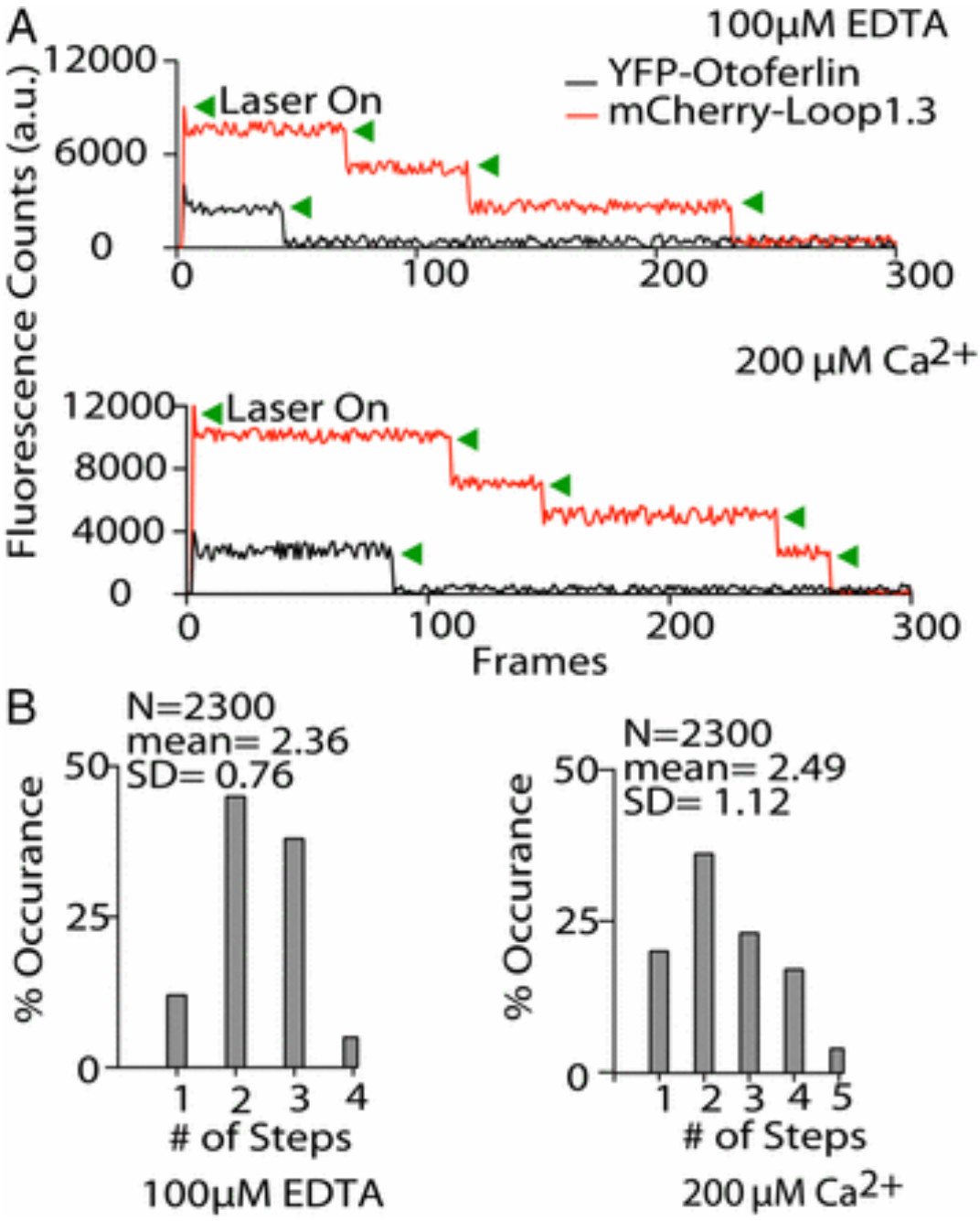

Figure 2.3: Otoferlin binds multiple Loop1.3 molecules
Otoferlin binds multiple Loop1.3 molecules. (A) Representative single-molecule photobleaching traces for Loop1.3-mCherry bound to YFP-otoferlin in the presence of 100 µM EDTA (Upper) and 200 µM calcium (Lower). Green arrowheads denote photobleaching events. (B) Single-molecule photobleaching distributions for EDTA and calcium conditions (n = 2,300).

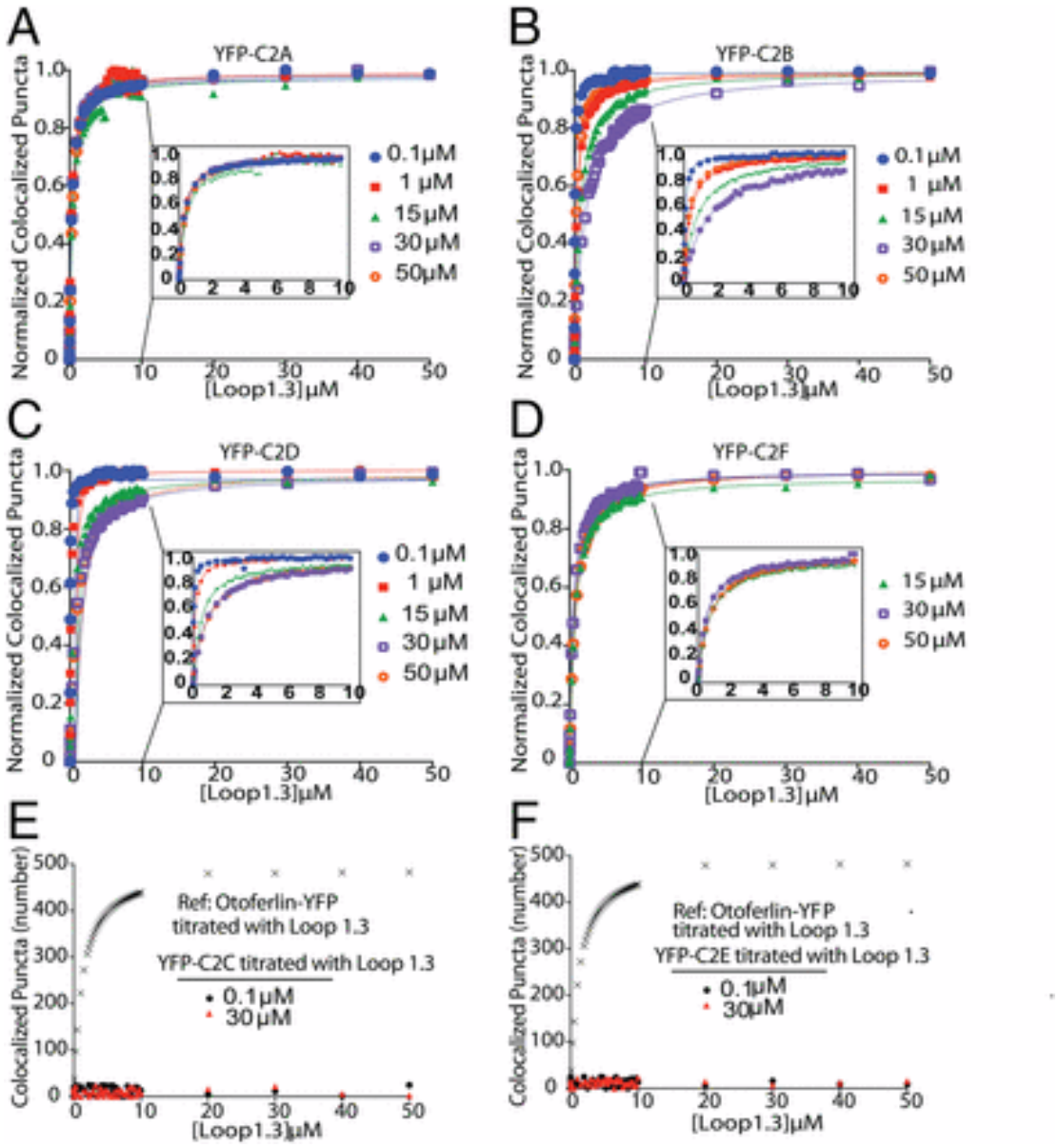

Figure 2.4: Multiple C2 domains mediate otoferlin-Loop1.3 interactions
Multiple C2 domains mediate otoferlin–Loop1.3 interaction. (A–D) Binding curves for immobilized YFP-otoferlin C2A (A), C2B (B), C2D (C), and C2F (D) domains titrated against Loop1.3 at 0.1–50 μM free calcium. Data are fit with a Langmuir isotherm (solid lines). Insets depict 0–10 μM for clarity. Each experimental data point represents the mean value of n = 3. (E and F) Binding curves for immobilized YFP-otoferlin C2C and C2E domains titrated against Loop1.3. Colocalization between Loop1.3 and YFP-otoferlin (otoferlin amino acids 1–1,885) is included for comparison.

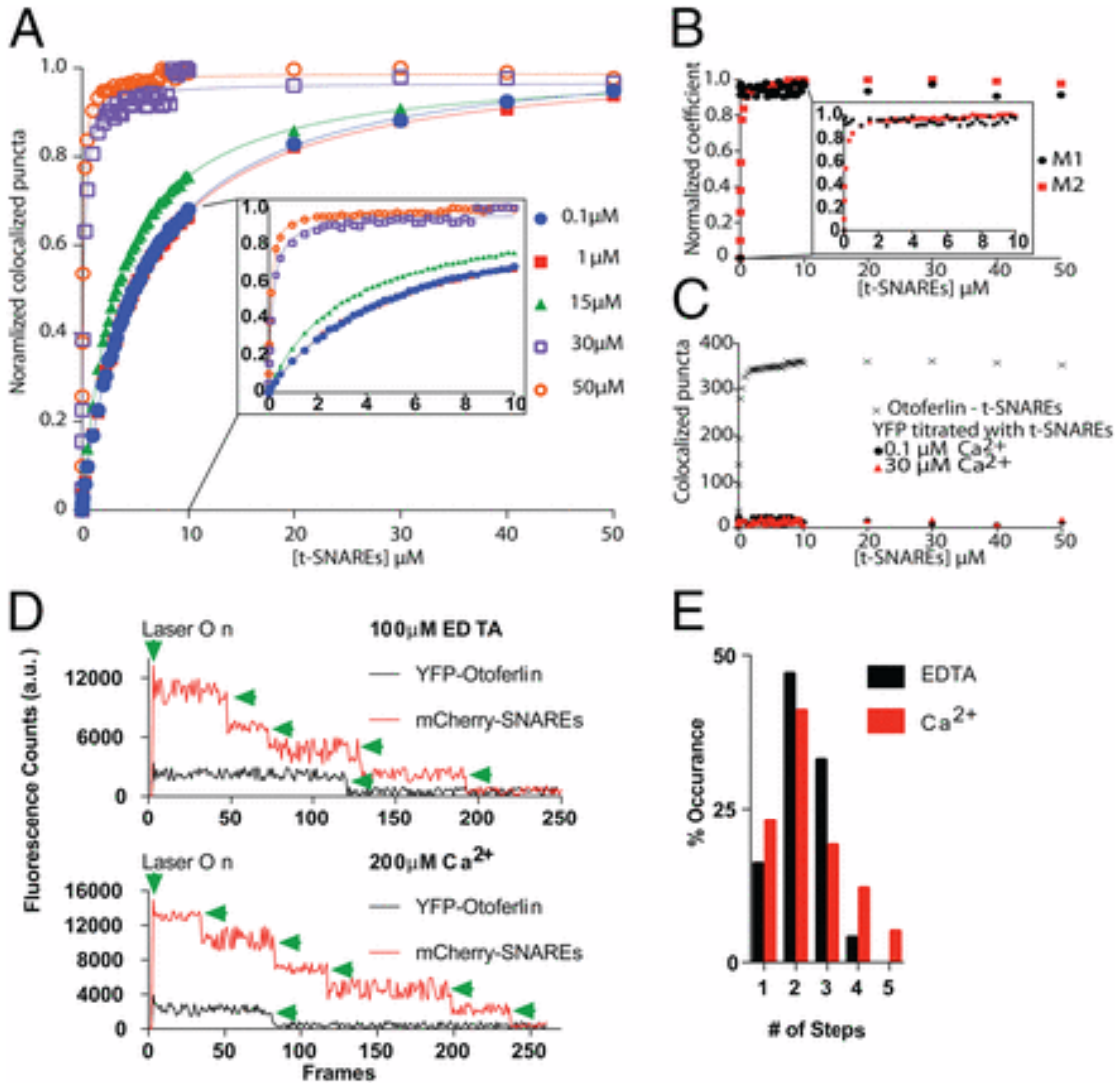

Figure 2.5: Otoferlin binds t-SNAREs.
t-SNARE binding curve in the presence of increasing free calcium concentrations (0.1–50 µM). (A) Experimental data are fit with a Langmuir isotherm (solid lines).Each experimental data point represents the mean value of n = 3. Inset depicts 0–10 µM for clarity. (B) Mander's coefficients M1 (black) and M2 (red) for YFP-otoferlin–t-SNARE colocalization. Inset depicts 0–10 µM for clarity. (C) Titration of t-SNARE with immobilized YFP in the presence of 0.1 or 30 µM free calcium. Each experimental data point represents the mean value of n = 3. (D) Representative single-molecule photobleaching traces for mCherry–t-SNARE bound to YFP-otoferlin in the presence of 100 µM ethylenediaminetetraacetic acid (EDTA) (Upper) and 200 µM calcium (Lower). Green arrowheads denote photobleaching events. a.u., arbitrary units. (E) Single-molecule photobleaching distributions for EDTA and calcium conditions (n = 2,300).

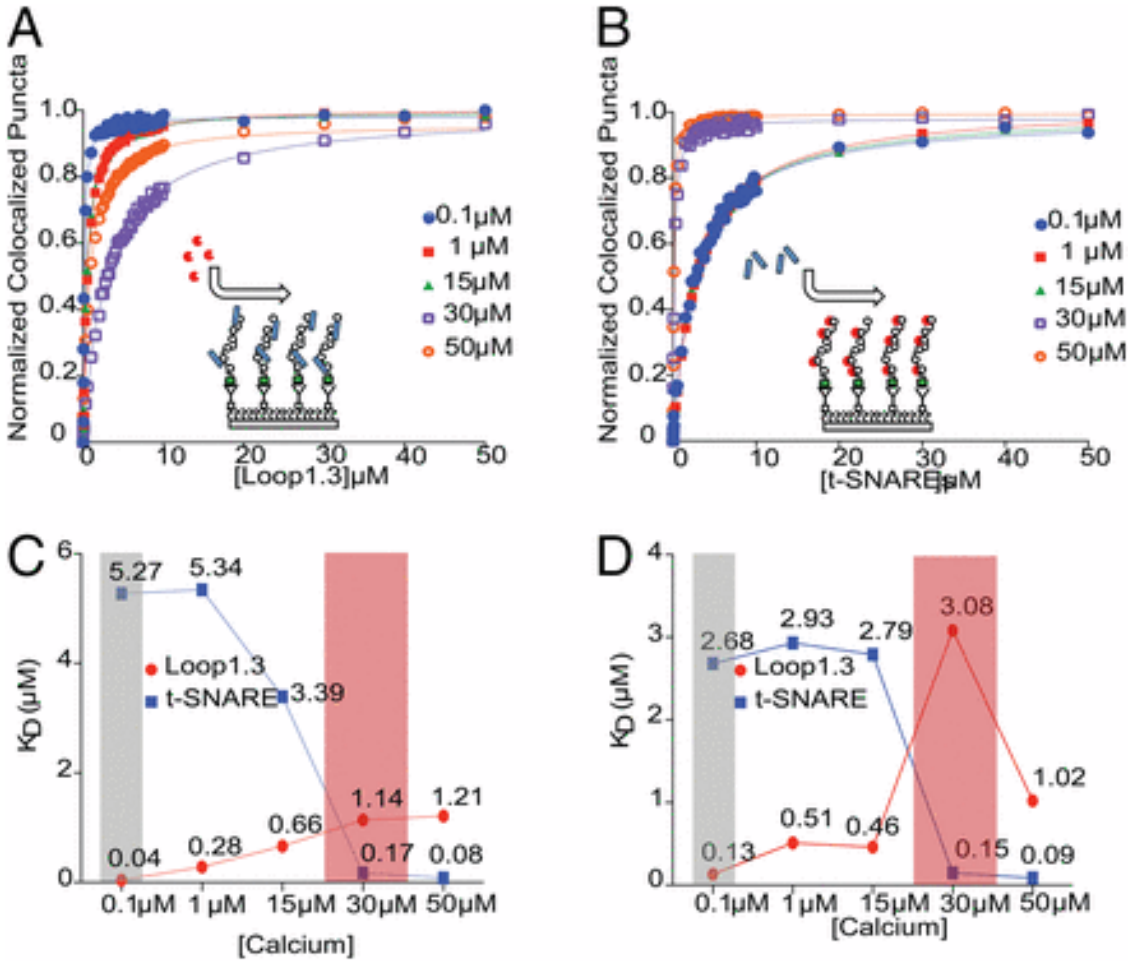

Figure 2.6: Titration of Loop1.3 or t-SNAREs onto heteromeric complexes
(A) Titration of Loop1.3 with immobilized t-SNARE–YFP-otoferlin complexes at indicated calcium concentration (0.1–50 μM). (B) Titration of t-SNARE with immobilized Loop1.3-YFP-otoferlin complexes at indicated calcium concentration (0.1–50 μM). (C) Dissociation constants for YFP-otoferlin binding to either t-SNARE or Loop1.3 individually plotted as a function of calcium. (D) Dissociation constants for YFP-otoferlin heteromeric complex binding to t-SNARE or Loop1.3 plotted as a function of calcium. The shaded gray and red areas represent the calcium concentration ranges of hair cell synapses during inactive and active states, respectively.

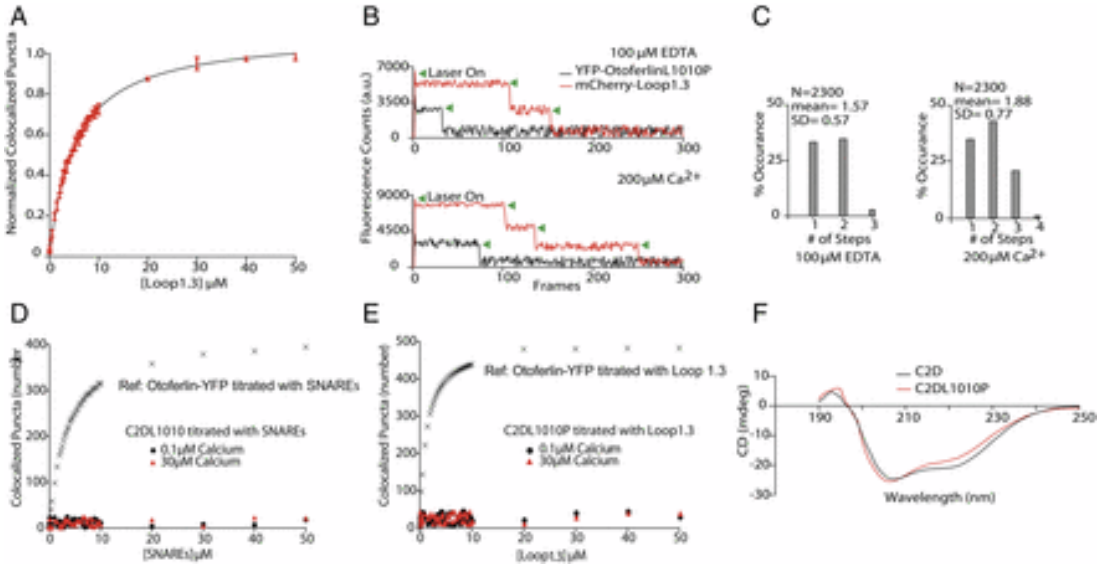

Figure 2.7: The pathogenic mutation L1010P reduces otoferlin-Loop1.3 interaction
(A) Titration curve of Loop1.3 with immobilized YFP-otoferlin$_{L1010P}$ in 50 μM free calcium. (B) Representative photobleaching time course for colocalized YFP-otoferlin$_{L1010P}$-mCherry-Loop1.3 puncta. Green arrowheads represent individual bleaching steps. (C) Photobleaching distributions for YFP-otoferlin$_{L1010P}$-mCherry-Loop1.3 puncta in EDTA and calcium (n =2,300 puncta). (D) Dose–response for immobilized YFP-C2DL1010P titrated with t-SNAREs in the presence of 0.1 or 30 μM calcium (n = 3). Colocalization between t-SNAREs and YFP-otoferlin is included for comparison. (E) Dose–response for immobilized YFP-C2DL1010P titrated with Loop1.3 in the presence of 0.1 or 30 μM calcium (n = 3). Colocalization between Loop1.3 and YFP-otoferlin is included for comparison. (F) CD spectrum for WT C2D and C2DL1010P.

	C2A		C2B		C2C	
	$Loop_{1.3}$ (μM)	SNARES (μM)	$Loop_{1.3}$ (μM)	SNARES (μM)	$Loop_{1.3}$ (μM)	SNARES (μM)
0.1μM Ca^{2+}	0.31± 0.03	0.56± 0.06	0.07± 0.01	1.19± 0.01	-	1.04± 0.04
1μM Ca^{2+}	0.28± 0.02	0.57± 0.07	0.35± 0.04	1.00± 0.01	-	1.24± 0.01
15μM Ca^{2+}	0.44± 0.03	0.46± 0.01	0.80± 0.01	0.09± 0.02	-	0.66± 0.01
30μM Ca^{2+}	0.31± 0.04	0.46± 0.02	1.51± 0.03	0.07± 0.01	-	0.10± 0.01
50μM Ca^{2+}	0.38± 0.04	0.59± 0.02	0.29± 0.03	0.07± 0.01	-	0.15± 0.05

	C2D		C2E		C2F	
	$Loop_{1.3}$ (μM)	SNARES (μM)	$Loop_{1.3}$ (μM)	SNARES (μM)	$Loop_{1.3}$ (μM)	SNARES (μM)
0.1μM Ca^{2+}	0.03± 0.02	-	-	1.17± 0.01	-	-
1μM Ca^{2+}	0.12± 0.02	-	-	1.09± 0.01	-	1.79± 0.03
15μM Ca^{2+}	0.50± 0.08	-	-	0.49± 0.09	0.75± 0.01	0.83± 0.01
30μM Ca^{2+}	0.88± 0.02	-	-	0.30± 0.07	0.51± 0.01	0.05± 0.02
50μM Ca^{2+}	0.90± 0.08	-	-	0.09± 0.01	0.74± 0.05	0.04± 0.02

Table 2.1: Otoferlin C2 domain K_d constants

	Otoferlin						Synaptotagmin-I	
	Wild-Type Separate Titrations		Wild-Type Heterocomplex Titrations		L1010P Separate Titrations		Wild-Type Separate Titrations	
	$Loop_{1.3}$ (μM)	SNAREs (μM)	$Loop_{1.3}$ (μM)	SNAREs (μM)	$Loop_{1.3}$ (μM)	SNAREs (μM)	$Loop_{1.3}$ (μM)	$Loop_{2.2}$ (μM)
0.1μM Ca^{2+}	0.04± 0.02	5.27± 0.03	0.13± 0.03	2.68± 0.06	-	-	-	1.06± 0.03
1μM Ca^{2+}	0.28± 0.01	5.34± 0.05	0.51± 0.06	2.93± 0.02	-	-	-	0.37± 0.01
15μM Ca^{2+}	0.66± 0.02	3.39± 0.03	0.46± 0.05	2.79± 0.02	-	-	-	0.15± 0.02
30μM Ca^{2+}	1.14± 0.07	0.17± 0.01	3.08± 0.05	0.15± 0.04	-	10.15± 0.12	-	0.07± 0.04
50μM Ca^{2+}	1.21± 0.08	0.08± 0.02	1.02± 0.02	0.09± 0.01	5.20± 0.05	7.32± 0.07	-	0.10± 0.03

Table 2.2: Otoferlin-YFP K_d constant

Chapter 3

Acridone as a probe to characterize the membrane dipping properties of otoferlin using smTIRF

Nicole Hams, Shauna Otto, Weihong Qiu, Colin Johnson

3.1 Abstract

Otoferlin is a vesical-associated transmembrane protein consisting of six C2 domains that is proposed to act as a calcium sensor for exocytosis in inner hair cells. It is thought that otoferlin mediates exocytosis by inserting into the plasma membrane in order to bring both it and the vesicle in close juxtaposition to allow for fusion. Indeed, otoferlin has been shown to mediate vesicle fusion but the mechanism of action is poorly understood. Fluorescence studies in which the environmentally sensitive amino acid, acridone, was used to probe membrane insertion using prepared liposomes revealed PI(4,5)P_2 dependent interactions for the otoferlin C2F domain. However, these interactions were shown to be calcium independent despite exocytosis occurring in a calcium-dependent manner. Here, we use C2F-incorporated acridone to assay dipping as a function of adjacent C2 domains. Our results indicate that the C2F domain in the context of the C-terminal doublet (C2EF) construct inserts in a calcium sensitive manner. Based on these results, we propose that the C2F domain targets otoferlin-containing vesicles to the plasma membrane, while the C2E domain confers calcium-sensitivity to the dipping process. Studies conducted with the soluble protein, domains C2ABCDEF support the hypothesis that the remaining domains may act to stabilize membrane dipping at the carbonyl-tail interface of the membrane.

3.2 Materials and Methods

3.2.1 Plasmid constructs

Mouse otoferlin was provided as a gift from Christine Petit, Institut Pasteur, Paris. Otoferlin amino acids corresponding to C2F (1719-1885), C2EF (1479-1885), C2DEF (959-1885) or C2ABCDEF (1-1885) were subcloned into the SspI site of pMCSG9. Mutagenic primers, designed using PrimerX, were used to create a TAG stop codon at F1833 for acridone-2ylalanine (acridone) incorporation.

3.2.2 Protein expression and purification

Otoferlin constructs in pMCSG9 were co-transformed into BL21(ai) cells with a vector containing the tRNA and tRNA synthetase needed to incorporate acridone into the protein. This vector was a gift from Ryan Mehl, Oregon State University, Corvallis. All constructs were expressed into autoinduction media with 1mM acridone using a previously reported

method[586,587]. The acridone was synthesized by E. James Petersson, University of Pennsylvania, Philadelphia. The cells were lysed by sonication in 50mM HEPES pH 7.5, 150mM NaCl and 1mM NaN_3 (lysis buffer) containing 1mM PMSF, 2μg/mL aprotinin, 5μg/mL leupeptin and 1μg/mL peptatin A. After sonication, CHAPS was added to the lysis buffer to a final concentration of 2% and the cells were incubate for 1 hour on ice with rocking followed by centrifugation at 4C for 20 minutes at 15,000x g. The soluable fraction was collected and incubated with Ni-NTA resin for 2-3 hours at 4C. After incubation the bound resin was washed with lysis buffer containing 20mM imidazole before the protein was eluted with lysis buffer containing 500mM imidazole. Purified proteins were dialyzed overnight in lysis buffer before being aliquoted into smaller volumes and flash frozen in lysis buffer containing 7.5% glycerol.

3.2.3 Phospholipid vesicles

All lipids and liposome preparation materials were purchased from Avanti Polar Lipids. SUVs were composed from chloroform suspensions of 25% POPS, 74% POPC and 1% Rhodamine POPE or 25% POPS, 72% POPC, 1% Rhodamine POPE and 2% PI(4,5)P2. Doxyl-5 POPC or Doxyl-12 POPC were incorporated at 10% and subtracted from the concentration of POPC. The chloroform was evaporated under nitrogen gas and the lipids were further dried under vacuum for 3-16 hours. The dried lipids were suspended in 50mM HEPES pH 7.5, 150mM NaCl and incubated at 37C with shaking for 30 minutes before being extruded 60 times through a 100nm filter.

3.2.4 Sedimentation assays

The C2 domains of otoferlin (5μg) were mixed with SUVs (100μg) in buffer composed of 50mM HEPES pH 7.5, 150mM NaCl with calcium (200μM) or EDTA (100μM). After incubation for 1 hour at 37C the mixture was centrifuged at 85,000 xg for 1 hour in a TA-100 ultracentrifuge (Beckmann Instruments). The results were analyzed on a 10% polyacrylamide gel using SDS-PAGE.

3.2.5 TIRF measurements and analysis

Coverslips were functionalized with PEG-Biotin and the otoferlin constructs were immobilized on the coverslips using a biotinylated 6xHis antibody (Abcam ab27025) as

previously reported[588]. All TIRF measurements were ran in 50mM HEPES pH 7.5, 150mM NaCl supplemented with 0.4% glucose, 45μg/mL catalase and 0.2U glucose oxidase. Single- and multiwavelength TIRF imaging was performed using a Zeiss TIRF3 laser system. Acridone was exited using a 405nm laser and detected using filter set 73. Rhodamine was excited using 561nm laser and detected using filter set 77. TIRF intensity data was extracted using ImageJ (NIH) and analyzed using Graphpad Prism software.

3.3 Results

Roughly 360 million people worldwide are affected by hearing impairment. Children account for 10% of those cases and each year approximately 12,000 newborns are diagnosed with congenital deafness. The majority of diagnoses are caused by genetic factors in isolation of any other set of disorders, commonly known as non-syndromic deafness. Mutations in the gene OTOF are the underlying cause of neurosensory nonsyndromic recessive deafness (DFNB9). OTOF encodes for otoferlin, a 240kDa vesicle-associated protein that is required for auditory exocytosis in inner hair cells (IHCs)[214]. In response to calcium, the C2 domains of otoferlin fuse vesicles containing neurotransmitters to the plasma membrane of IHCs for relay to the post-synaptic auditory neuron. In animal models the absence of otoferlin in IHCs results in phenotypes analogous to DFNB9 in humans[216,232,244]. Despite the prevalence of functional data, the mechanisms that otofelrin uses to promote exocytosis have yet to be resolved. The reason for this is partly due to the size and insolubility of otoferlin which has restricted *in vitro* studies to recombinant truncates that incompletely reflect the activity of the protein.

Similar to otoferlin, Synaptotagmin-I (Syt-I) is the calcium-sensor for exocytosis in neurons. Upon calcium influx the C2 domains of Syt-I insert into the plasma membrane bilayer creating local curvature stress[142,144,155]. Remodeling the bilayer is a critical step that brings both membranes into close proximity and lowers the energy barrier for fusion. However, insertion alone is not sufficient to induce membrane bending. Indeed, the C2 domains of PKCα and cPLA2 insert into membrane bilayers but do not promote deformations[589,590]. Syt-I's ability to remodel membranes has been demonstrated using electron microscopy[155]. It was found that insertion closer to the bilayer center coupled with a collective effort between both C2 domains of Syt-I is pivotal to inducing membrane curvature. Although specific C2 domains of otoferlin insert into

membranes, their ability to collectively induce curvature has yet to be tested using electron microscopy due again to its size and insolubility preventing adequate protein purification[239].

To overcome this barrier, we have designed a single-molecule total internal reflection fluorescence microscopy, smTIRFM, assay to measure membrane-penetration depth as a method to infer the ability of a C2 domain to deform bilayers (Figure 3.1A). This assay works by using the parallax method (Eq.5) which describes the distance of a fluorescent probe from the center of the lipid bilayer (Z_{CF}) using membrane embedded quenchers, 5-doxyl-phosphatidylcholine (5-doxyl-PC) and 12-doxyl-phosphatidylcholine (12-doxyl-PC) where L_{C1} is the distance from the bilayer center to 5-doxyl-PC (12.2 Å), C is the mole fraction of the quencher divided by lipid area (70 Å), F_1 and F_2 are the intensity of 5-doxyl-PC and 12-doxyl-PC, respectively, and L is the difference in position of the doxyl group along the acyl chain (0.9 Å per CH_2 group)[152,591].

$$Z_{CF} = L_{C1} + [-\ln(F_1/F_2)/\pi C\text{-}L^2]/2L \qquad \text{(Eq.5)}$$

The fluorescent non-canonical amino acid acridone (Acd) has previously been used as a reporter for the membrane-penetrating phenylalanine 1833 of otoferlin C2F domain[239]. Acd undergoes a reduction in intensity in the presence of shallow (5-doxyl-PC) or deep (12-doxyl-PC) quenchers[587].

To establish whether Acd influences membrane binding interactions, we performed co-sedimentation assays using otoferlin C2F, C2EF or C2DEF harboring either the wild-type phenylalanine ($C2_{WT}$) or Acd ($C2_{Acd}$) at residue 1833. We compared the supernatant (S) and pellet (P) fraction for liposomes composed of phosphatidylserine and phosphatidylcholine (PS-PC) or phosphatidylserine, phosphatidylcholine and phosphatidylinositol 4,5-biphosphate (PS-PC-PI(4,5)P_2) in the presence of either calcium or EDTA (Figure 3.1B). We found that constructs harboring Acd at position 1833 demonstrated the same binding behavior as the WT C2 domains. Based upon these results, we concluded that acridone did not significantly influence interactions between otoferlin and membranes. Further, each of the six constructs had an N-terminal maltose-binding protein (MBP) tag to help increase solubility. When sedimented with liposomes, MBP stayed in the supernatant fraction regardless of lipid composition suggesting that the presence of MBP did not influence membrane interactions, either.

When we applied our smTIRFM assay to $C2_{Acd}$ constructs, we found that C2F insertion only occurred in the presence of PI(4,5)P_2-containing liposome independently of the presence of calcium or the calcium-chelator, EDTA (Figure 3.2A). Intensity measurements were plotted in a histogram format and fit to a Gaussian curve. Goodness of fit for each curve are reported in Supplemental Table 3.1. Fluorescence intensity changes for experiments with PI(4,5)P_2 liposomes revealed that intensity frequency decreased equally between calcium and EDTA experiments as phosphatidylcholine was replaced with either 5-doxyl-PC or 12-doxyl-PC. These results suggest that in the context of PI(4,5)P_2 liposomes, the relative depth of membrane insertion is constant regardless of the presence of calcium or EDTA. We next assayed $C2F_{Acd}$ membrane-insertion in the context of the C2EF doublet and found that Acd intensity only increased when both calcium and PI(4,5)P_2 were present, together (Figure 3.2B). Comparison of $C2EF_{Acd}$ signal in the presence of calcium and PI(4,5)P_2 with $C2F_{Acd}$ in the presence of PI(4,5)P_2 shows that the relative depth of membrane insertion does not change with the addition of the adjacent C2 domain. Taken together, these results promote a model in which the presence of the C2E domains directly confers calcium sensitivity to the C2F membrane-penetration activity.

We further tested whether the presence of adjacent N-terminal C2 domains confer additional membrane-interaction properties using $C2DEF_{Acd}$ and $C2ABCDEF_{Acd}$. Compared to our $C2F_{Acd}$ and $C2EF_{Acd}$ data, no additional shifts in acridone intensity frequencies were observed for either of the longer otoferlin constructs (Figure 3.3A,B). We did however, observed a slight decrease in the frequency of low intensity interactions. These “dipping intermediates” likely represent the C2F loop moving in and out of the membrane. We observed that the frequency of these intermediates decreased as more C2 domains were included in the otoferlin constructs suggesting that additional C2 domains may act to stabilize the C2F interaction with the lipid bilayer (Figure 3.3C). Using the parallax method, we were able to determine the distance of F1833 from the center of the membrane bilayer (Table 3.1). Otoferlin inserts more closely to the bilayer center than either Syt-I C2 domain[61,124].

We have shown the importance of the otoferlin C-terminal domains in mediating membrane-insertion interactions. Further, we have provided a mechanism in which the C2E domain of otoferlin confers calcium-sensitivity onto the C2F domain. In the presence of the C2E domain, C2F inserts into the plasma membrane bilayer and bends it as a method to accelerate auditory exocytosis. In zebrafish, the C-terminal domains of otoferlin are sufficient to rescue

hearing in otoferlin knockdown mutants however the mechanism behind the rescue was not understood[232]. We propose that similar to PI(4,5)P_2 steering Syt-I to the plasma membranes in neurons, PI(4,5)P_2 also works to steer otoferlin to the plasma membrane in IHCs[143]. There, calcium influx initiates the penetration of F1833 into the membrane bilayer. Membrane insertion brings both bilayers into closer opposition thereby allowing SNARE complexes to form in preparation for fusion. We have used the parallax method to determine depth of dipping insertion as a prediction of otoferlin C2F domain ability to induce bilayer remodeling. Insertion closer to the bilayer center causes more bending than shallow insertion and as a result there is more mismatch between the two leaflets. The mismatch exposes hydrophobic areas to an aqueous environment and by destabilizing the top leaflet, making it more prone to merge with another membrane.

How can auditory exocytosis be a calcium-dependent process when the most conserved C2 domain across ferlins, the C2F domain, binds phospholipids independent of calcium? In Syt-I, the presence of the C2A domain is required for regulating C2B domain interactions with membranes[155]. Here, we have shown that the C2EF domains of otoferlin may operate in similar way to Syt-I and in doing so, have demonstrated the importance of studying the entire otoferlin protein instead of truncates. The importance of cross-talk between C2 domains has frequently been demonstrated in Syt-I studies and has only recently been shown to be important for otoferlin[61,124,588,592]. Although truncate studies of otoferlin have highlighted important functional data, it is clear that in order to reconcile mechanistic information, the entire protein must be studied. Here, while we showed that the C2EF domain is the minimum amount of otoferlin needed to induce membrane-insertion, we were also able to confirm the roles of the remaining C2 domains in this process. Further, Syt-I membrane interactions have demonstrated that membrane insertion alone is not sufficient for inducing membrane bending. Membrane deformation has been suggested to result from the coordinated effort of two or more interactions from one protein or a collective effort from multiple copies of a protein. In the case of otoferlin, the presence of multiple copies of different C2 domains may provide the interactions necessary to deform the plasma membrane. We have demonstrated that during the membrane-insertion process, the C2A thru C2D act to stabilize the bilayer interaction.

The importance of the C-terminal domains seems to be a common theme among the ferlin family of proteins. The calcium-dependent protease, calpain-2, has been shown to cleave

otoferlin, myoferlin and dysferlin[173,194,593]. Calpains were first implicated in membrane fusion events when giant squid axons failed to reseal in the presence of the calpain-inhibitor, calpeptin[594]. Later it was shown that calcium-dependent membrane resealing in mammalian cells is abrogated in cells that contain calpain mutants[595]. The cleaveage of otoferlin, dysferlin or myoferlin by calpain-2 releases a "mini-ferlin" composed of C-terminal domain fragments. In general, dysferlin acts as the calcium-sensor at sites of membrane injury. The "mini-dysferlin" resembles a synaptotagmin-like module that acts as a less-regulated calcium sensor that is produced in response to excessive calcium influx, such as severe muscle injury. In the case of myoferlin, the role of the calpain-cleaved product, "mini-myoferlin" is not yet understood. However, full-length myoferlin isoforms harboring the calpain cleavage product have been shown to activate MAPK/ERK signaling pathways. When inappropriately activated, these signaling pathways have been linked to uncontrolled cell growth. Here, we have demonstrated a possible physiological role for the otoferlin calpain-cleavage during synaptic vesicle exocytosis. Therapy options for patients affected with DFNB9 are non-existent due to the size of otoferlin. However, with this work, we have provided a mechanism for why the C-terminal was sufficient for rescuing deaf phenotypes in otofelrin knock-down zebrafish. In doing so, this work lays the foundation for gene therapy options for DFNB9 patients.

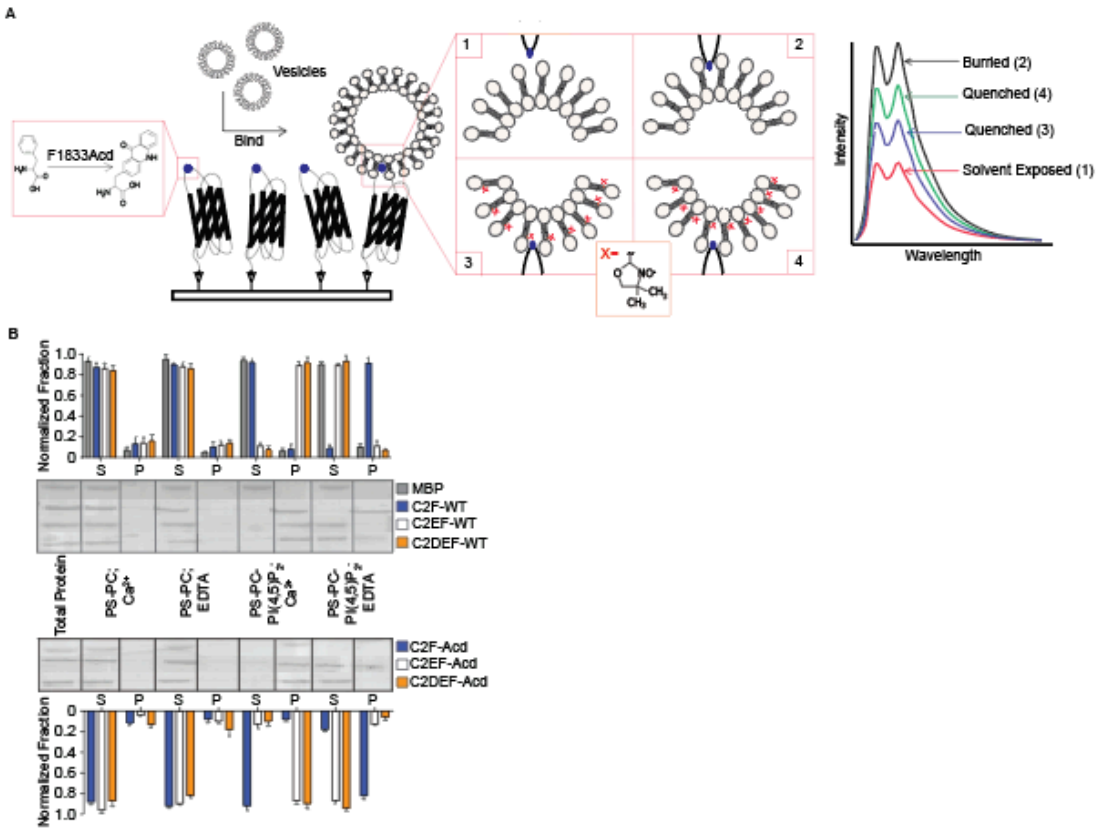

Figure 3.1: (**A**) Co-sedimentation of MBP, otoferlin wild-type C2 domains (top panel) or otoferlin F1833Acd C2 domains (bottom panel) in the presence of calcium or EDTA with vesicles of varying lipid composition. In both instances, the co-sedimentation results are quantified from N=3 replicates. Error bars = std. (**B**) A cartoon depicting the single-molecule dipping assay. Otoferlin C2F domain harboring a F1833Acd mutation is immobilized to coverslip. Vesicles containing PC, PC-Doxyl-5 or PC-Doxyl-12 are flowed over the immobilized protein and allowed to bind. Insertion is measured as a function of fluorescence signal increase, in the case of PC containing vesicles (black line), or quenching, in the case of Doxyl-5 (blue line) or Doxyl-12 (green line) containing vesicles. Events in which little to no protein-lipid interaction occurs exposes acridone to the aqueous environment resulting in greater fluorescence signal quenching (red line).

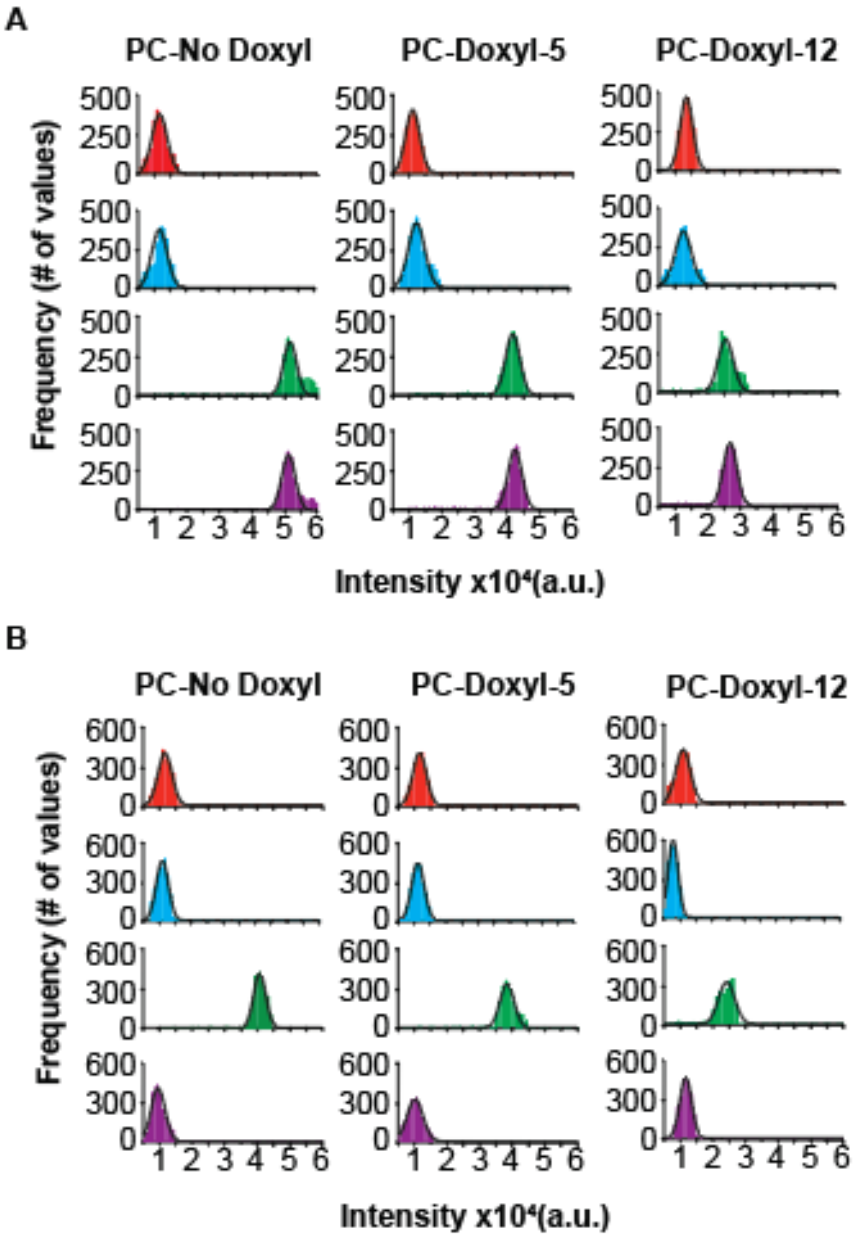

Figure 3.2: Histogram fit with Gaussian distribution of (**A**) otoferlin C2F F1833Acd and (**B**) otoferlin C2EF F1833Acd interacting with liposomes composed of PS-PC with calcium (red), PS-PC with EDTA (blue), PS-PC-PI(4,5)P_2 with calcium (green) or PS-PC-PI(4,5)P_2 with EDTA (purple). The histograms represent N=2300 data points.

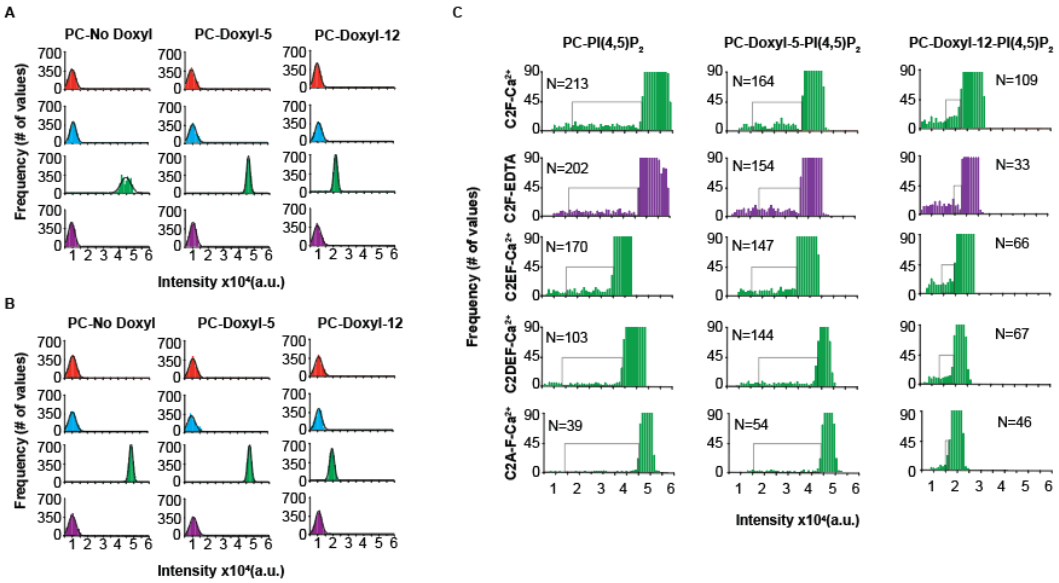

Figure 3.3: Histogram fit with Gaussian distribution of (**A**) otoferlin C2DEF F1833Acd and (**B**) otoferlin C2ABCDEF F1833Acd interacting with liposomes composed of PS-PC with calcium (red), PS-PC with EDTA (blue), PS-PC-PI(4,5)P_2 with calcium (green) or PS-PC-PI(4,5)P_2 with EDTA (purple). The histograms represent N=2300 data points. (**C**) Magnification of select histograms from Figure 2 and Figure 3A and 3B showing low frequency intermediates. The N value represents the total number of intermediates captured in the black square. The lower limit of the black squares was determined by the intensity that resulted in the least non-zero frequency of events that occurred on the right side of the normal distribution for the complementary data set. The upper limit for the black squares was determined by the intensity that resulted in frequencies of 45 events or less for the data set being analyzed.

Distance from bilayer center (Å)

	PS-PC-PI(4,5)P_2; Ca^{2+}	PS-PC-PI(4,5)P_2; EDTA
C2F	8.960 ± 0.010	8.968 ±0.007
C2EF	8.968 ±0.012	
C2DEF	8.914 ±0.008	
C2A-F	8.888 ±0.014	

Table 3.1

Chapter 4
Concluding remarks and future directions for characterizing otoferlin function

Nicole Hams

Hearing loss affects somewhere around 360 million people worldwide. Roughly 10% of those affected are children, and a staggering 7200 newborns per year are diagnosed with congenital hear loss that are a result of genetic factors. These genetic causes can be syndromic, in which its intertwined with another set of disorders or non-syndromic, in which deafness occurs without other associated disorders. Out of those born with non-syndromic deafness, 5-8% are deaf as a result of a mutation to otoferlin[596,597]. To date, over 60 pathogenic mutations range in type from frameshift to single amino acid deletions or substitutions have been found to be associated with otoferlin-related hearing loss[244]. Interdisciplinary studies conducted over the past decade have established that otoferlin is essential for encoding sound at the ribbon synapse of IHCs.

Although my dissertation presents a single-molecule in vitro characterization of otoferlin function in IHC, the exact function of otoferlin in the IHC has yet to be fully characterized. One of the biggest challenges in characterizing otoferlin lays in a lack of structural characterization. Besides the structure of its C2A domain no other structural information exists for otoferlin. Unfortunately, the C2A domain does not bind calcium and thus the structural information that it provides does not help to characterize calcium-dependent interactions. A crystal structure of otoferlin would provide a molecular basis for determining protein and lipid binding sites. For example, a major function of the otoferlin C2 domains is the binding of phospholipid headgroups. However, the inability to resolve a crystal structure of C2 domains in complex with phospholipids has hindered the ability to completely define the membrane-binding mechanism for each domain. Further, a molecular structure would provide insight into how the lysine rich region of the C2C and C2F domains coordinate both a lipid and protein target.

From a functional stand-point, it's also unclear the mechanistic role that otoferlin plays in synaptic vesicle neurotransmission at the IHC synapse. Exocytosis involves vesicle targeting, docking, priming and fusion. Although otoferlin is undoubtedly involved in fusion, the role it plays in the earlier steps is unknown. Identifying otoferlin binding partners via pull-down assays or RNAseq can be invaluable in determining not only otoferlin's role during exocytosis, but also the role and contribution of its associated binding partners. Comparative studies of other ribbon synapses can also provide information about proteins involved in vesicle trafficking at the IHC synapse. The ribbon synapse of retinal bipolar cells, in particular, are an attractive candidate for

such a study given that their large number, similarity and accessibility can allow for a better comparative study of IHC function.

Moving forward, future experiment should include the use of techniques that, at least, include the soluble fraction of otoferlin. My dissertation has highlighted the importance of including the entire soluble fraction of otoferlin by revealing previously unknown functions that would have been impossible to infer using only otoferlin truncates. One promising avenue involves using tetrazine, an unnatural amino acid, to physically tether otoferlin to liposomes. This system would limit the protein's conformation to a more physiologically relevant state. In the case of synaptotagmin, taking into account its physical limitations has led to mechanistic breakthroughs[144,154,518,592]. Another important approach to studying otoferlin should include the use of lipid environments. Supported lipid bilayers and nanodiscs have both been used to study synaptotagmin[142,520]. One primary advantage of using supported lipid bilayers is its compatibility with single-molecule imaging techniques. Additionally, lipid-phase separation allows for the protein-component to partition into the parts of the bilayer that provide a more ideal environment for protein function. Similarly, nanodics provide some of the same advantages of supported lipid bilayers in addition to access to both sides of the membrane and control of oligomerization states.

Finally, reconciliation of otoferlin mechanics in vivo will help correlate molecular events with physiological outcomes. Mice have long been used as animal models for studying otoferlin, due mostly impart to their wide availability and high-sequence identity to human otoferlin. However, zebrafish have more recently been shown to also be a model organism to study otoferlin[232]. Zebrafish express otoferlin, are easy to genetically manipulate and contain a cluster of easily acceptable inner hair cells, called neuromast, in their lateral line. As a result, using zebrafish models potentially provides a new outlook on otoferlin-related research.

References

1. Hedin, L. E., Illergård, K. & Elofsson, A. An introduction to membrane proteins. *J. Proteome Res.* **10,** 3324–3331 (2011).
2. Ingólfsson, H. I. *et al.* Lipid Organization of the Plasma Membrane. *J. Am. Chem. Soc.* **136,** 14554–14559 (2014).
3. Antonny, B. Mechanisms of Membrane Curvature Sensing. *Annu. Rev. Biochem.* **80,** 101–123 (2011).
4. van Meer, G., Voelker, D. R. & Feigenson, G. W. Membrane lipids: where they are and how they behave. *Nat. Rev. Mol. Cell Biol.* **9,** 112–124 (2008).
5. Fadeel, B. & Xue, D. The ins and outs of phospholipid asymmetry in the plasma membrane: roles in health and disease. *Crit. Rev. Biochem. Mol. Biol.* **44,** 264–277 (2009).
6. Bigay, J. & Antonny, B. Curvature, Lipid Packing, and Electrostatics of Membrane Organelles: Defining Cellular Territories in Determining Specificity. *Dev. Cell* **23,** 886–895 (2012).
7. Janmey, P. A. & Kinnunen, P. K. J. Biophysical properties of lipids and dynamic membranes. *Trends Cell Biol.* **16,** 538–546 (2006).
8. van den Brink-van der Laan, E., Antoinette Killian, J. & de Kruijff, B. Nonbilayer lipids affect peripheral and integral membrane proteins via changes in the lateral pressure profile. *Biochim. Biophys. Acta BBA - Biomembr.* **1666,** 275–288 (2004).
9. Jahn, R. & Südhof, T. C. Membrane fusion and exocytosis. *Annu. Rev. Biochem.* **68,** 863–911 (1999).

10. Devaux, P. F. & Morris, R. Transmembrane Asymmetry and Lateral Domains in Biological Membranes. *Traffic* **5,** 241–246 (2004).

11. Daleke, D. L. Phospholipid Flippases. *J. Biol. Chem.* **282,** 821–825 (2007).

12. Fairn, G. D. *et al.* High-resolution mapping reveals topologically distinct cellular pools of phosphatidylserine. *J. Cell Biol.* **194,** 257–275 (2011).

13. Kay, J. G., Koivusalo, M., Ma, X., Wohland, T. & Grinstein, S. Phosphatidylserine dynamics in cellular membranes. *Mol. Biol. Cell* **23,** 2198–2212 (2012).

14. Meer, G. van & Kroon, A. I. P. M. de. Lipid map of the mammalian cell. *J Cell Sci* **124,** 5–8 (2011).

15. Corbalan-Garcia, S. & Gómez-Fernández, J. C. Signaling through C2 domains: More than one lipid target. *Biochim. Biophys. Acta BBA - Biomembr.* **1838,** 1536–1547 (2014).

16. Di Paolo, G. & De Camilli, P. Phosphoinositides in cell regulation and membrane dynamics. *Nature* **443,** 651–657 (2006).

17. Balla, T. Phosphoinositides: tiny lipids with giant impact on cell regulation. *Physiol. Rev.* **93,** 1019–1137 (2013).

18. Mejillano, M. *et al.* Regulation of apoptosis by phosphatidylinositol 4,5-bisphosphate inhibition of caspases, and caspase inactivation of phosphatidylinositol phosphate 5-kinases. *J. Biol. Chem.* **276,** 1865–1872 (2001).

19. Sun, Y. & Drubin, D. G. The functions of anionic phospholipids during clathrin-mediated endocytosis site initiation and vesicle formation. *J Cell Sci* **125,** 6157–6165 (2012).

20. Logan, M. R. & Mandato, C. A. Regulation of the actin cytoskeleton by PIP2 in cytokinesis. *Biol. Cell* **98,** 377–388 (2006).

21. Pitcher, J. A. *et al.* Phosphatidylinositol 4,5-Bisphosphate (PIP2)-enhanced G Protein-coupled Receptor Kinase (GRK) Activity: LOCATION, STRUCTURE, AND REGULATION OF THE PIP2 BINDING SITE DISTINGUISHES THE GRK SUBFAMILIES. *J. Biol. Chem.* **271,** 24907–24913 (1996).

22. Marat, A. L. & Haucke, V. Phosphatidylinositol 3-phosphates—at the interface between cell signalling and membrane traffic. *EMBO J.* **35,** 561–579 (2016).

23. Raiborg, C. *et al.* Hrs sorts ubiquitinated proteins into clathrin-coated microdomains of early endosomes. *Nat. Cell Biol.* **4,** 394–398 (2002).

24. Posor, Y. *et al.* Spatiotemporal control of endocytosis by phosphatidylinositol-3,4-bisphosphate. *Nature* **499,** 233–237 (2013).

25. Mayinger, P. Phosphoinositides and vesicular membrane traffic. *Biochim. Biophys. Acta* **1821,** 1104–1113 (2012).

26. Cantley, L. C. The phosphoinositide 3-kinase pathway. *Science* **296,** 1655–1657 (2002).

27. Vanhaesebroeck, B., Guillermet-Guibert, J., Graupera, M. & Bilanges, B. The emerging mechanisms of isoform-specific PI3K signalling. *Nat. Rev. Mol. Cell Biol.* **11,** 329–341 (2010).

28. Cho, W. & Stahelin, R. V. Membrane binding and subcellular targeting of C2 domains. *Biochim. Biophys. Acta* **1761,** 838–849 (2006).

29. Nishizuka, Y. The molecular heterogeneity of protein kinase C and its implications for cellular regulation. *Nature* **334,** 661–665 (1988).

30. U Kikkawa, A Kishimoto & Nishizuka, and Y. The Protein Kinase C Family: Heterogeneity and its Implications. *Annu. Rev. Biochem.* **58,** 31–44 (1989).

31. Coussens, L. *et al.* Multiple, distinct forms of bovine and human protein kinase C suggest diversity in cellular signaling pathways. *Science* **233,** 859–867 (1986).

32. Knopf, J. L. *et al.* Cloning and expression of multiple protein kinase C cDNAs. *Cell* **46,** 491–502 (1986).

33. Ono, Y. *et al.* Two types of complementary DNAs of rat brain protein kinase C: Heterogeneity determined by alternative splicing. *FEBS Lett.* **206,** 347–352 (1986).

34. Ono, Y. *et al.* Cloning of rat brain protein kinase C complementary DNA. *FEBS Lett.* **203,** 111–115 (1986).

35. Parker, P. J. *et al.* The Complete Primary Structure of Protein Kinase C--the Major Phorbol Ester Receptor. *Science* **233,** 853–859 (1986).

36. Nalefski, E. A. & Falke, J. J. The C2 domain calcium-binding motif: structural and functional diversity. *Protein Sci. Publ. Protein Soc.* **5,** 2375–2390 (1996).

37. Sossin, W. S. & Schwartz, J. H. Ca(2+)-independent protein kinase Cs contain an amino-terminal domain similar to the C2 consensus sequence. *Trends Biochem. Sci.* **18,** 207–208 (1993).

38. Clark, J. D. *et al.* A novel arachidonic acid-selective cytosolic PLA2 contains a Ca2+-dependent translocation domain with homology to PKC and GAP. *Cell* **65,** 1043–1051 (1991).

39. Rhee, S. G., Suh, P. G., Ryu, S. H. & Lee, S. Y. Studies of inositol phospholipid-specific phospholipase C. *Science* **244,** 546–550 (1989).

40. Hiles, I. D. *et al.* Phosphatidylinositol 3-kinase: Structure and expression of the 110 kd catalytic subunit. *Cell* **70,** 419–429 (1992).

41. Trahey, M. *et al.* Molecular cloning of two types of GAP complementary DNA from human placenta. *Science* **242,** 1697–1700 (1988).

42. Plant, P. J., Yeger, H., Staub, O., Howard, P. & Rotin, D. The C2 Domain of the Ubiquitin Protein Ligase Nedd4 Mediates Ca2+-dependent Plasma Membrane Localization. *J. Biol. Chem.* **272,** 32329–32336 (1997).

43. Perin, M. S., Brose, N., Jahn, R. & Südhof, T. C. Domain structure of synaptotagmin (p65). *J. Biol. Chem.* **266,** 623–629 (1991).

44. Shirataki, H. *et al.* Rabphilin-3A, a putative target protein for smg p25A/rab3A p25 small GTP-binding protein related to synaptotagmin. *Mol. Cell. Biol.* **13,** 2061–2068 (1993).

45. Perin, M. S., Fried, V. A., Mignery, G. A., Jahn, R. & Südhof, T. C. Phospholipid binding by a synaptic vesicle protein homologous to the regulatory region of protein kinase C. *Nature* **345,** 260–263 (1990).

46. Wang, Y., Okamoto, M., Schmitz, F., Hofmann, K. & Südhof, T. C. Rim is a putative Rab3 effector in regulating synaptic-vesicle fusion. *Nature* **388,** 593–598 (1997).

47. Marty, N. J., Holman, C. L., Abdullah, N. & Johnson, C. P. The C2 domains of otoferlin, dysferlin, and myoferlin alter the packing of lipid bilayers. *Biochemistry (Mosc.)* **52,** 5585–5592 (2013).

48. Davletov, B. A. & Südhof, T. C. A single C2 domain from synaptotagmin I is sufficient for high affinity Ca2+/phospholipid binding. *J. Biol. Chem.* **268,** 26386–26390 (1993).

49. Chapman, E. R. & Jahn, R. Calcium-dependent interaction of the cytoplasmic region of synaptotagmin with membranes. Autonomous function of a single C2-homologous domain. *J. Biol. Chem.* **269,** 5735–5741 (1994).

50. Lek, A., Lek, M., North, K. N. & Cooper, S. T. Phylogenetic analysis of ferlin genes reveals ancient eukaryotic origins. *BMC Evol. Biol.* **10,** 231 (2010).

51. Martens, S. & McMahon, H. T. Mechanisms of membrane fusion: disparate players and common principles. *Nat. Rev. Mol. Cell Biol.* **9,** 543–556 (2008).

52. Schultz, J., Milpetz, F., Bork, P. & Ponting, C. P. SMART, a simple modular architecture research tool: Identification of signaling domains. *Proc. Natl. Acad. Sci.* **95,** 5857–5864 (1998).

53. Letunic, I. *et al.* SMART 5: domains in the context of genomes and networks. *Nucleic Acids Res.* **34,** D257–D260 (2006).

54. Corbalán-García, S. & Gómez-Fernández, J. C. Protein kinase C regulatory domains: The art of decoding many different signals in membranes. *Biochim. Biophys. Acta BBA - Mol. Cell Biol. Lipids* **1761,** 633–654 (2006).

55. Redpath, G. M. I., Sophocleous, R. A., Turnbull, L., Whitchurch, C. B. & Cooper, S. T. Ferlins Show Tissue-Specific Expression and Segregate as Plasma Membrane/Late Endosomal or Trans-Golgi/Recycling Ferlins. *Traffic Cph. Den.* **17,** 245–266 (2016).

56. Lek, A., Evesson, F. J., Sutton, R. B., North, K. N. & Cooper, S. T. Ferlins: Regulators of Vesicle Fusion for Auditory Neurotransmission, Receptor Trafficking and Membrane Repair. *Traffic* **13,** 185–194 (2012).

57. Rizo, J. & Südhof, T. C. C2-domains, structure and function of a universal Ca2+-binding domain. *J. Biol. Chem.* **273,** 15879–15882 (1998).

58. Essen, L.-O., Perisic, O., Cheung, R., Katan, M. & Williams, R. L. Crystal structure of a mammalian phosphoinositide-specific phospholipase Cδ. *Nature* **380,** 595–602 (1996).

59. Sutton, R. B., Davletov, B. A., Berghuis, A. M., Sudhof, T. C. & Sprang, S. R. Structure of the first C2 domain of synaptotagmin I: A novel Ca2+/phospholipid-binding fold. *Cell* **80,** 929–938 (1995).

60. Herrick, D. Z., Sterbling, S., Rasch, K. A., Hinderliter, A. & Cafiso, D. S. Position of synaptotagmin I at the membrane interface: cooperative interactions of tandem C2 domains. *Biochemistry (Mosc.)* **45,** 9668–9674 (2006).

61. Hui, E., Bai, J. & Chapman, E. R. Ca2+-triggered simultaneous membrane penetration of the tandem C2-domains of synaptotagmin I. *Biophys. J.* **91,** 1767–1777 (2006).

62. Shao, X. *et al.* Synaptotagmin–Syntaxin Interaction: The C2 Domain as a Ca2+-Dependent Electrostatic Switch. *Neuron* **18,** 133–142 (1997).

63. Murray, D. & Honig, B. Electrostatic Control of the Membrane Targeting of C2 Domains. *Mol. Cell* **9,** 145–154 (2002).

64. Verdaguer, N., Corbalan-Garcia, S., Ochoa, W. F., Fita, I. & Gómez-Fernández, J. C. Ca2+ bridges the C2 membrane-binding domain of protein kinase Cα directly to phosphatidylserine. *EMBO J.* **18,** 6329–6338 (1999).

65. Shao, X., Davletov, B. A., Sutton, R. B., Südhof, T. C. & Rizo, J. Bipartite Ca2+-binding motif in C2 domains of synaptotagmin and protein kinase C. *Science* **273,** 248–251 (1996).

66. Grobler, J. A., Essen, L. O., Williams, R. L. & Hurley, J. H. C2 domain conformational changes in phospholipase C-delta 1. *Nat. Struct. Biol.* **3,** 788–795 (1996).

67. Shao, X., Fernandez, I., Südhof, T. C. & Rizo, J. Solution Structures of the Ca2+-free and Ca2+-bound C2A Domain of Synaptotagmin I: Does Ca2+ Induce a Conformational Change? *Biochemistry (Mosc.)* **37,** 16106–16115 (1998).

68. Scott, D. L. *et al.* Interfacial Catalysis: The Mechanism of Phospholipase A2. *Science* **250,** 1541–1546 (1990).

69. Thunnissen, M. M. *et al.* X-ray structure of phospholipase A2 complexed with a substrate-derived inhibitor. *Nature* **347,** 689–691 (1990).

70. Swairjo, M. A., Concha, N. O., Kaetzel, M. A., Dedman, J. R. & Seaton, B. A. Ca(2+)-bridging mechanism and phospholipid head group recognition in the membrane-binding protein annexin V. *Nat. Struct. Biol.* **2,** 968–974 (1995).

71. Medkova, M. & Cho, W. Differential Membrane-Binding and Activation Mechanisms of Protein Kinase C-α and -ε. *Biochemistry (Mosc.)* **37,** 4892–4900 (1998).

72. Perisic, O., Fong, S., Lynch, D. E., Bycroft, M. & Williams, R. L. Crystal Structure of a Calcium-Phospholipid Binding Domain from Cytosolic Phospholipase A2. *J. Biol. Chem.* **273,** 1596–1604 (1998).

73. Fernandez, I. *et al.* Three-dimensional structure of the synaptotagmin 1 C2B-domain: synaptotagmin 1 as a phospholipid binding machine. *Neuron* **32,** 1057–1069 (2001).

74. Wang, P., Wang, C.-T., Bai, J., Jackson, M. B. & Chapman, E. R. Mutations in the effector binding loops in the C2A and C2B domains of synaptotagmin I disrupt exocytosis in a nonadditive manner. *J. Biol. Chem.* **278,** 47030–47037 (2003).

75. Fukuda, M., Kojima, T. & Mikoshiba, K. Phospholipid composition dependence of Ca2+-dependent phospholipid binding to the C2A domain of synaptotagmin IV. *J. Biol. Chem.* **271,** 8430–8434 (1996).

76. Corbalán-García, S., Rodríguez-Alfaro, J. A. & Gómez-Fernández, J. C. Determination of the calcium-binding sites of the C2 domain of protein kinase Calpha that are critical for its translocation to the plasma membrane. *Biochem. J.* **337 (Pt 3),** 513–521 (1999).

77. Nalefski, E. A. *et al.* C2 domains from different Ca2+ signaling pathways display functional and mechanistic diversity. *Biochemistry (Mosc.)* **40,** 3089–3100 (2001).

78. Nalefski, E. A. *et al.* Independent folding and ligand specificity of the C2 calcium-dependent lipid binding domain of cytosolic phospholipase A2. *J. Biol. Chem.* **273,** 1365–1372 (1998).

79. Morita, E. *et al.* Human ESCRT and ALIX proteins interact with proteins of the midbody and function in cytokinesis. *EMBO J.* **26,** 4215–4227 (2007).

80. Engelenburg, S. B. V. *et al.* Distribution of ESCRT Machinery at HIV Assembly Sites Reveals Virus Scaffolding of ESCRT Subunits. *Science* **343,** 653–656 (2014).

81. Mears, J. A. *et al.* Conformational changes in Dnm1 support a contractile mechanism for mitochondrial fission. *Nat. Struct. Mol. Biol.* **18,** 20–26 (2011).

82. Fröhlich, C. *et al.* Structural insights into oligomerization and mitochondrial remodelling of dynamin 1-like protein. *EMBO J.* **32,** 1280–1292 (2013).

83. Hu, J. *et al.* A Class of Dynamin-like GTPases Involved in the Generation of the Tubular ER Network. *Cell* **138,** 549–561 (2009).

84. Lee, C. & Chen, L. B. Dynamic behavior of endoplasmic reticulum in living cells. *Cell* **54,** 37–46 (1988).

85. Conner, S. D. & Schmid, S. L. Regulated portals of entry into the cell. *Nature* **422,** 37–44 (2003).

86. Carlton, J. G. & Martin-Serrano, J. Parallels Between Cytokinesis and Retroviral Budding: A Role for the ESCRT Machinery. *Science* **316,** 1908–1912 (2007).

87. De Robertis, E. & Franchi, C. M. Electron microscope observations on synaptic vesicles in synapses of the retinal rods and cones. *J. Biophys. Biochem. Cytol.* **2,** 307–318 (1956).

88. Di Carlo, V. Ultrastructure of the membrane of synaptic vesicles. *Nature* **213,** 833–835 (1967).

89. Sudhof, T. C. The synaptic vesicle cycle. *Annu. Rev. Neurosci.* **27,** 509–547 (2004).

90. Benfenati, F., Valtorta, F., Bähler, M. & Greengard, P. Synapsin I, a neuron-specific phosphoprotein interacting with small synaptic vesicles and F-actin. *Cell Biol. Int. Rep.* **13,** 1007–1021 (1989).

91. Matthews, G. & Fuchs, P. The diverse roles of ribbon synapses in sensory neurotransmission. *Nat. Rev. Neurosci.* **11,** 812–822 (2010).

92. Vaithianathan, T., Henry, D., Akmentin, W. & Matthews, G. Nanoscale dynamics of synaptic vesicle trafficking and fusion at the presynaptic active zone. *eLife* **5,** (2016).

93. Sigrist, S. J. & Schmitz, D. Structural and functional plasticity of the cytoplasmic active zone. *Curr. Opin. Neurobiol.* **21,** 144–150 (2011).

94. Gundelfinger, E. D. & Fejtova, A. Molecular organization and plasticity of the cytomatrix at the active zone. *Curr. Opin. Neurobiol.* **22,** 423–430 (2012).

95. Hallermann, S. & Silver, R. A. Sustaining rapid vesicular release at active zones: potential roles for vesicle tethering. *Trends Neurosci.* **36,** 185–194 (2013).

96. Meinrenken, C. J., Borst, J. G. G. & Sakmann, B. Local routes revisited: the space and time dependence of the Ca2+ signal for phasic transmitter release at the rat calyx of Held. *J. Physiol.* **547,** 665–689 (2003).

97. Schneggenburger, R. & Neher, E. Presynaptic calcium and control of vesicle fusion. *Curr. Opin. Neurobiol.* **15,** 266–274 (2005).

98. Kyoung, M., Zhang, Y., Diao, J., Chu, S. & Brunger, A. T. Studying calcium triggered vesicle fusion in a single vesicle-vesicle content/lipid mixing system. *Nat. Protoc.* **8,** 1–16 (2013).

99. Ramakrishnan, N. A., Drescher, M. J. & Drescher, D. G. The SNARE complex in neuronal and sensory cells. *Mol. Cell. Neurosci.* **50,** 58–69 (2012).

100. Chernomordik, L. V. & Kozlov, M. M. Protein-lipid interplay in fusion and fission of biological membranes. *Annu. Rev. Biochem.* **72,** 175–207 (2003).

101. Jackson, M. B. & Chapman, E. R. Fusion pores and fusion machines in Ca2+-triggered exocytosis. *Annu. Rev. Biophys. Biomol. Struct.* **35,** 135–160 (2006).

102. Lindau, M. & Almers, W. Structure and function of fusion pores in exocytosis and ectoplasmic membrane fusion. *Curr. Opin. Cell Biol.* **7,** 509–517 (1995).

103. Chanturiya, A., Chernomordik, L. V. & Zimmerberg, J. Flickering fusion pores comparable with initial exocytotic pores occur in protein-free phospholipid bilayers. *Proc. Natl. Acad. Sci.* **94,** 14423–14428 (1997).

104. Cohen, F. S. & Melikyan, G. B. The energetics of membrane fusion from binding, through hemifusion, pore formation, and pore enlargement. *J. Membr. Biol.* **199,** 1–14 (2004).

105. Li, C. *et al.* Ca(2+)-dependent and -independent activities of neural and non-neural synaptotagmins. *Nature* **375,** 594–599 (1995).

106. Craxton, M. Evolutionary genomics of plant genes encoding N-terminal-TM-C2 domain proteins and the similar FAM62 genes and synaptotagmin genes of metazoans. *BMC Genomics* **8,** 259 (2007).

107. Südhof, T. C. Synaptotagmins: why so many? *J. Biol. Chem.* **277,** 7629–7632 (2002).

108. Michaut, M. *et al.* Synaptotagmin VI participates in the acrosome reaction of human spermatozoa. *Dev. Biol.* **235,** 521–529 (2001).

109. Martens, S., Kozlov, M. M. & McMahon, H. T. How synaptotagmin promotes membrane fusion. *Science* **316,** 1205–1208 (2007).

110. Iezzi, M., Kouri, G., Fukuda, M. & Wollheim, C. B. Synaptotagmin V and IX isoforms control Ca2+ -dependent insulin exocytosis. *J. Cell Sci.* **117,** 3119–3127 (2004).

111. Reddy, A., Caler, E. V. & Andrews, N. W. Plasma membrane repair is mediated by Ca(2+)-regulated exocytosis of lysosomes. *Cell* **106,** 157–169 (2001).

112. Sugita, S., Shin, O.-H., Han, W., Lao, Y. & Südhof, T. C. Synaptotagmins form a hierarchy of exocytotic Ca(2+) sensors with distinct Ca(2+) affinities. *EMBO J.* **21,** 270–280 (2002).

113. Augustine, G. J. How does calcium trigger neurotransmitter release? *Curr. Opin. Neurobiol.* **11,** 320–326 (2001).

114. Koh, T. W. & Bellen, H. J. Synaptotagmin I, a Ca2+ sensor for neurotransmitter release. *Trends Neurosci.* **26,** 413–422 (2003).

115. Chapman, E. R. Synaptotagmin: a Ca(2+) sensor that triggers exocytosis? *Nat. Rev. Mol. Cell Biol.* **3,** 498–508 (2002).

116. Fernández-Chacón, R. *et al.* Synaptotagmin I functions as a calcium regulator of release probability. *Nature* **410,** 41–49 (2001).

117. Rhee, J.-S. *et al.* Augmenting neurotransmitter release by enhancing the apparent Ca2+ affinity of synaptotagmin 1. *Proc. Natl. Acad. Sci. U. S. A.* **102,** 18664–18669 (2005).

118. Pang, Z. P., Shin, O.-H., Meyer, A. C., Rosenmund, C. & Südhof, T. C. A gain-of-function mutation in synaptotagmin-1 reveals a critical role of Ca2+-dependent

soluble N-ethylmaleimide-sensitive factor attachment protein receptor complex binding in synaptic exocytosis. *J. Neurosci. Off. J. Soc. Neurosci.* **26,** 12556–12565 (2006).

119. Pang, Z. P., Sun, J., Rizo, J., Maximov, A. & Südhof, T. C. Genetic analysis of synaptotagmin 2 in spontaneous and Ca2+-triggered neurotransmitter release. *EMBO J.* **25,** 2039–2050 (2006).

120. Xu, J., Mashimo, T. & Südhof, T. C. Synaptotagmin-1, -2, and -9: Ca(2+) sensors for fast release that specify distinct presynaptic properties in subsets of neurons. *Neuron* **54,** 567–581 (2007).

121. Zhang, X., Kim-Miller, M. J., Fukuda, M., Kowalchyk, J. A. & Martin, T. F. J. Ca2+-dependent synaptotagmin binding to SNAP-25 is essential for Ca2+-triggered exocytosis. *Neuron* **34,** 599–611 (2002).

122. Bai, J., Wang, C.-T., Richards, D. A., Jackson, M. B. & Chapman, E. R. Fusion pore dynamics are regulated by synaptotagmin*t-SNARE interactions. *Neuron* **41,** 929–942 (2004).

123. Bhalla, A., Tucker, W. C. & Chapman, E. R. Synaptotagmin isoforms couple distinct ranges of Ca2+, Ba2+, and Sr2+ concentration to SNARE-mediated membrane fusion. *Mol. Biol. Cell* **16,** 4755–4764 (2005).

124. Bai, J., Wang, P. & Chapman, E. R. C2A activates a cryptic Ca(2+)-triggered membrane penetration activity within the C2B domain of synaptotagmin I. *Proc. Natl. Acad. Sci. U. S. A.* **99,** 1665–1670 (2002).

125. Vrljic, M. *et al.* Molecular mechanism of the synaptotagmin-SNARE interaction in Ca2+-triggered vesicle fusion. *Nat. Struct. Mol. Biol.* **17,** 325–331 (2010).

126. Sutton, R. B., Ernst, J. A. & Brunger, A. T. Crystal structure of the cytosolic C2A-C2B domains of synaptotagmin III. Implications for Ca(+2)-independent snare complex interaction. *J. Cell Biol.* **147,** 589–598 (1999).

127. Fuson, K. L., Montes, M., Robert, J. J. & Sutton, R. B. Structure of human synaptotagmin 1 C2AB in the absence of Ca2+ reveals a novel domain association. *Biochemistry (Mosc.)* **46,** 13041–13048 (2007).

128. Araç, D. *et al.* Close membrane-membrane proximity induced by Ca(2+)-dependent multivalent binding of synaptotagmin-1 to phospholipids. *Nat. Struct. Mol. Biol.* **13,** 209–217 (2006).

129. Herrick, D. Z. *et al.* Solution and membrane-bound conformations of the tandem C2A and C2B domains of synaptotagmin 1: Evidence for bilayer bridging. *J. Mol. Biol.* **390,** 913–923 (2009).

130. Tucker, W. C., Weber, T. & Chapman, E. R. Reconstitution of Ca2+-regulated membrane fusion by synaptotagmin and SNAREs. *Science* **304,** 435–438 (2004).

131. Zhang, X., Rizo, J. & Südhof, T. C. Mechanism of phospholipid binding by the C2A-domain of synaptotagmin I. *Biochemistry (Mosc.)* **37,** 12395–12403 (1998).

132. Brose, N., Petrenko, A. G., Südhof, T. C. & Jahn, R. Synaptotagmin: a calcium sensor on the synaptic vesicle surface. *Science* **256,** 1021–1025 (1992).

133. Radhakrishnan, A., Stein, A., Jahn, R. & Fasshauer, D. The Ca2+ Affinity of Synaptotagmin 1 Is Markedly Increased by a Specific Interaction of Its C2B Domain with Phosphatidylinositol 4,5-Bisphosphate. *J. Biol. Chem.* **284,** 25749–25760 (2009).

134. Kielian, M. & Rey, F. A. Virus membrane-fusion proteins: more than one way to make a hairpin. *Nat. Rev. Microbiol.* **4,** 67–76 (2006).

135. Markosyan, R. M., Cohen, F. S. & Melikyan, G. B. The lipid-anchored ectodomain of influenza virus hemagglutinin (GPI-HA) is capable of inducing nonenlarging fusion pores. *Mol. Biol. Cell* **11,** 1143–1152 (2000).

136. Safieddine, S., El-Amraoui, A. & Petit, C. The auditory hair cell ribbon synapse: from assembly to function. *Annu. Rev. Neurosci.* **35,** 509–528 (2012).

137. Pang, Z. P. & Südhof, T. C. Cell biology of Ca2+-triggered exocytosis. *Curr. Opin. Cell Biol.* **22,** 496–505 (2010).

138. Davis, A. F. *et al.* Kinetics of synaptotagmin responses to Ca2+ and assembly with the core SNARE complex onto membranes. *Neuron* **24,** 363–376 (1999).

139. Kojima, T., Fukuda, M., Aruga, J. & Mikoshiba, K. Calcium-dependent phospholipid binding to the C2A domain of a ubiquitous form of double C2 protein (Doc2 beta). *J. Biochem. (Tokyo)* **120,** 671–676 (1996).

140. Kozlov, M. M. & Chernomordik, L. V. A mechanism of protein-mediated fusion: coupling between refolding of the influenza hemagglutinin and lipid rearrangements. *Biophys. J.* **75,** 1384–1396 (1998).

141. Kuzmin, P. I., Zimmerberg, J., Chizmadzhev, Y. A. & Cohen, F. S. A quantitative model for membrane fusion based on low-energy intermediates. *Proc. Natl. Acad. Sci. U. S. A.* **98,** 7235–7240 (2001).

142. Chapman, E. R. & Davis, A. F. Direct interaction of a Ca2+-binding loop of synaptotagmin with lipid bilayers. *J. Biol. Chem.* **273,** 13995–14001 (1998).

143. Bai, J., Tucker, W. C. & Chapman, E. R. PIP2 increases the speed of response of synaptotagmin and steers its membrane-penetration activity toward the plasma membrane. *Nat. Struct. Mol. Biol.* **11,** 36–44 (2004).

144. Hui, E. *et al.* Mechanism and function of synaptotagmin-mediated membrane apposition. *Nat. Struct. Mol. Biol.* **18,** 813–821 (2011).

145. Zhang, J. Z., Davletov, B. A., Südhof, T. C. & Anderson, R. G. Synaptotagmin I is a high affinity receptor for clathrin AP-2: implications for membrane recycling. *Cell* **78,** 751–760 (1994).

146. Sheng, Z. H., Yokoyama, C. T. & Catterall, W. A. Interaction of the synprint site of N-type Ca2+ channels with the C2B domain of synaptotagmin I. *Proc. Natl. Acad. Sci. U. S. A.* **94,** 5405–5410 (1997).

147. Chapman, E. R., Desai, R. C., Davis, A. F. & Tornehl, C. K. Delineation of the oligomerization, AP-2 binding, and synprint binding region of the C2B domain of synaptotagmin. *J. Biol. Chem.* **273,** 32966–32972 (1998).

148. Littleton, J. T. *et al.* synaptotagmin mutants reveal essential functions for the C2B domain in Ca2+-triggered fusion and recycling of synaptic vesicles in vivo. *J. Neurosci. Off. J. Soc. Neurosci.* **21,** 1421–1433 (2001).

149. Schiavo, G., Gu, Q. M., Prestwich, G. D., Söllner, T. H. & Rothman, J. E. Calcium-dependent switching of the specificity of phosphoinositide binding to synaptotagmin. *Proc. Natl. Acad. Sci. U. S. A.* **93,** 13327–13332 (1996).

150. Kanaseki, T., Kawasaki, K., Murata, M., Ikeuchi, Y. & Ohnishi, S. Structural features of membrane fusion between influenza virus and liposome as revealed by quick-freezing electron microscopy. *J. Cell Biol.* **137,** 1041–1056 (1997).

151. Han, X., Bushweller, J. H., Cafiso, D. S. & Tamm, L. K. Membrane structure and fusion-triggering conformational change of the fusion domain from influenza hemagglutinin. *Nat. Struct. Mol. Biol.* **8,** nsb0801_715 (2001).

152. Bai, J., Earles, C. A., Lewis, J. L. & Chapman, E. R. Membrane-embedded synaptotagmin penetrates cis or trans target membranes and clusters via a novel mechanism. *J. Biol. Chem.* **275,** 25427–25435 (2000).

153. Chapman, E. R., An, S., Edwardson, J. M. & Jahn, R. A novel function for the second C2 domain of synaptotagmin. Ca2+-triggered dimerization. *J. Biol. Chem.* **271,** 5844–5849 (1996).

154. Chicka, M. C., Hui, E., Liu, H. & Chapman, E. R. Synaptotagmin arrests the SNARE complex before triggering fast, efficient membrane fusion in response to Ca2+. *Nat. Struct. Mol. Biol.* **15,** 827–835 (2008).

155. Hui, E., Johnson, C. P., Yao, J., Dunning, F. M. & Chapman, E. R. Synaptotagmin-mediated bending of the target membrane is a critical step in Ca(2+)-regulated fusion. *Cell* **138,** 709–721 (2009).

156. Tucker, W. C. *et al.* Identification of synaptotagmin effectors via acute inhibition of secretion from cracked PC12 cells. *J. Cell Biol.* **162,** 199–209 (2003).

157. Bhalla, A., Chicka, M. C., Tucker, W. C. & Chapman, E. R. Ca(2+)-synaptotagmin directly regulates t-SNARE function during reconstituted membrane fusion. *Nat. Struct. Mol. Biol.* **13,** 323–330 (2006).

158. Honigmann, A. *et al.* Phosphatidylinositol 4,5-bisphosphate clusters act as molecular beacons for vesicle recruitment. *Nat. Struct. Mol. Biol.* **20,** 679–686 (2013).

159. Li, L. *et al.* Phosphatidylinositol phosphates as co-activators of Ca2+ binding to C2 domains of synaptotagmin 1. *J. Biol. Chem.* **281,** 15845–15852 (2006).

160. Vrljic, M. *et al.* Post-translational modifications and lipid binding profile of insect cell-expressed full-length mammalian synaptotagmin 1. *Biochemistry (Mosc.)* **50,** 9998–10012 (2011).

161. Guillén, J. *et al.* Structural insights into the Ca2+ and PI(4,5)P2 binding modes of the C2 domains of rabphilin 3A and synaptotagmin 1. *Proc. Natl. Acad. Sci.* **110,** 20503–20508 (2013).

162. Bogaart, G. van den, Meyenberg, K., Diederichsen, U. & Jahn, R. Phosphatidylinositol 4,5-bisphosphate increases the Ca2+ affinity of synaptotagmin-1 40-fold. *J. Biol. Chem.* jbc.M112.343418 (2012). doi:10.1074/jbc.M112.343418

163. Park, Y. *et al.* Synaptotagmin-1 binds to PIP(2)-containing membrane but not to SNAREs at physiological ionic strength. *Nat. Struct. Mol. Biol.* **22,** 815–823 (2015).

164. Lu, X., Xu, Y., Zhang, F. & Shin, Y.-K. Synaptotagmin I and Ca(2+) promote half fusion more than full fusion in SNARE-mediated bilayer fusion. *FEBS Lett.* **580,** 2238–2246 (2006).

165. Earles, C. A., Bai, J., Wang, P. & Chapman, E. R. The tandem C2 domains of synaptotagmin contain redundant Ca2+ binding sites that cooperate to engage t-SNAREs and trigger exocytosis. *J. Cell Biol.* **154,** 1117–1123 (2001).

166. Desai, R. C. *et al.* The C2b Domain of Synaptotagmin Is a Ca2+–Sensing Module Essential for Exocytosis. *J. Cell Biol.* **150,** 1125–1136 (2000).

167. Tucker, W. C. & Chapman, E. R. Role of synaptotagmin in Ca2+-triggered exocytosis. *Biochem. J.* **366,** 1–13 (2002).

168. Choi, U. B. *et al.* Single-molecule FRET-derived model of the synaptotagmin 1-SNARE fusion complex. *Nat. Struct. Mol. Biol.* **17,** 318–324 (2010).

169. Tang, J. *et al.* A complexin/synaptotagmin 1 switch controls fast synaptic vesicle exocytosis. *Cell* **126,** 1175–1187 (2006).

170. Chapman, E. R., Hanson, P. I., An, S. & Jahn, R. Ca2+ regulates the interaction between synaptotagmin and syntaxin 1. *J. Biol. Chem.* **270,** 23667–23671 (1995).

171. Brewer, K. D. *et al.* Dynamic binding mode of a Synaptotagmin-1-SNARE complex in solution. *Nat. Struct. Mol. Biol.* **22,** 555–564 (2015).

172. Damer, C. K. & Creutz, C. E. Synergistic membrane interactions of the two C2 domains of synaptotagmin. *J. Biol. Chem.* **269,** 31115–31123 (1994).

173. Piper, A.-K. *et al.* Enzymatic cleavage of myoferlin releases a dual C2-domain module linked to ERK signalling. *Cell. Signal.* **33,** 30–40 (2017).

174. Jiménez, J. L. & Bashir, R. In silico functional and structural characterisation of ferlin proteins by mapping disease-causing mutations and evolutionary information onto three-dimensional models of their C2 domains. *J. Neurol. Sci.* **260,** 114–123 (2007).

175. Shin, O.-H., Han, W., Wang, Y. & Südhof, T. C. Evolutionarily conserved multiple C2 domain proteins with two transmembrane regions (MCTPs) and unusual Ca2+ binding properties. *J. Biol. Chem.* **280,** 1641–1651 (2005).

176. Min, S.-W., Chang, W.-P. & Südhof, T. C. E-Syts, a family of membranous Ca2+-sensor proteins with multiple C2 domains. *Proc. Natl. Acad. Sci. U. S. A.* **104,** 3823–3828 (2007).

177. Yamazaki, T., Takata, N., Uemura, M. & Kawamura, Y. Arabidopsis synaptotagmin SYT1, a type I signal-anchor protein, requires tandem C2 domains for delivery to the plasma membrane. *J. Biol. Chem.* **285,** 23165–23176 (2010).

178. Bashir, R. *et al.* A gene related to Caenorhabditis elegans spermatogenesis factor fer-1 is mutated in limb-girdle muscular dystrophy type 2B. *Nat. Genet.* **20,** 37–42 (1998).

179. Washington, N. L. & Ward, S. FER-1 regulates Ca2+ -mediated membrane fusion during C. elegans spermatogenesis. *J. Cell Sci.* **119,** 2552–2562 (2006).

180. Ohsako, T., Hirai, K. & Yamamoto, M.-T. The Drosophila misfire gene has an essential role in sperm activation during fertilization. *Genes Genet. Syst.* **78,** 253–266 (2003).

181. Smith, M. K. & Wakimoto, B. T. Complex regulation and multiple developmental functions of misfire, the Drosophila melanogaster ferlin gene. *BMC Dev. Biol.* **7,** 21 (2007).

182. Yan, M., Rachubinski, D. A., Joshi, S., Rachubinski, R. A. & Subramani, S. Dysferlin domain-containing proteins, Pex30p and Pex31p, localized to two compartments, control the number and size of oleate-induced peroxisomes in Pichia pastoris. *Mol. Biol. Cell* **19,** 885–898 (2008).

183. Aoki, M. *et al.* Genomic organization of the dysferlin gene and novel mutations in Miyoshi myopathy. *Neurology* **57,** 271–278 (2001).

184. Davis, D. B., Doherty, K. R., Delmonte, A. J. & McNally, E. M. Calcium-sensitive phospholipid binding properties of normal and mutant ferlin C2 domains. *J. Biol. Chem.* **277,** 22883–22888 (2002).

185. Cohn, R. D. & Campbell, K. P. Molecular basis of muscular dystrophies. *Muscle Nerve* **23,** 1456–1471 (2000).

186. Liu, J. *et al.* Dysferlin, a novel skeletal muscle gene, is mutated in Miyoshi myopathy and limb girdle muscular dystrophy. *Nat. Genet.* **20,** 31–36 (1998).

187. Illa, I. *et al.* Distal anterior compartment myopathy: a dysferlin mutation causing a new muscular dystrophy phenotype. *Ann. Neurol.* **49,** 130–134 (2001).

188. Bansal, D. & Campbell, K. P. Dysferlin and the plasma membrane repair in muscular dystrophy. *Trends Cell Biol.* **14,** 206–213 (2004).

189. Selcen, D., Stilling, G. & Engel, A. G. The earliest pathologic alterations in dysferlinopathy. *Neurology* **56,** 1472–1481 (2001).

190. Clarke, M. S., Khakee, R. & McNeil, P. L. Loss of cytoplasmic basic fibroblast growth factor from physiologically wounded myofibers of normal and dystrophic muscle. *J. Cell Sci.* **106 (Pt 1),** 121–133 (1993).

191. Anderson, L. V. B. *et al.* Dysferlin is a Plasma Membrane Protein and is Expressed Early in Human Development. *Hum. Mol. Genet.* **8,** 855–861 (1999).

192. Bansal, D. *et al.* Defective membrane repair in dysferlin-deficient muscular dystrophy. *Nature* **423,** 168–172 (2003).

193. Cai, C. *et al.* Membrane Repair Defects in Muscular Dystrophy Are Linked to Altered Interaction between MG53, Caveolin-3, and Dysferlin. *J. Biol. Chem.* **284,** 15894–15902 (2009).

194. Lek, A. *et al.* Calpains, Cleaved Mini-DysferlinC72, and L-Type Channels Underpin Calcium-Dependent Muscle Membrane Repair. *J. Neurosci.* **33,** 5085–5094 (2013).

195. Lennon, N. J. *et al.* Dysferlin Interacts with Annexins A1 and A2 and Mediates Sarcolemmal Wound-healing. *J. Biol. Chem.* **278,** 50466–50473 (2003).

196. Codding, S. J., Marty, N., Abdullah, N. & Johnson, C. P. Dysferlin Binds SNAREs (Soluble N-Ethylmaleimide-sensitive Factor (NSF) Attachment Protein Receptors) and Stimulates Membrane Fusion in a Calcium-sensitive Manner. *J. Biol. Chem.* **291,** 14575–14584 (2016).

197. Babiychuk, E. B. & Draeger, A. Annexins in Cell Membrane Dynamics: Ca2+-Regulated Association of Lipid Microdomains. *J. Cell Biol.* **150,** 1113–1124 (2000).

198. Lambert, O., Gerke, V., Bader, M.-F., Porte, F. & Brisson, A. Structural analysis of junctions formed between lipid membranes and several annexins by cryo-electron microscopy11Edited by M. F. Moody. *J. Mol. Biol.* **272,** 42–55 (1997).

199. Han, W.-Q. *et al.* Lysosome fusion to the cell membrane is mediated by the dysferlin C2A domain in coronary arterial endothelial cells. *J Cell Sci* **125,** 1225–1234 (2012).

200. McDade, J. R. & Michele, D. E. Membrane damage-induced vesicle-vesicle fusion of dysferlin-containing vesicles in muscle cells requires microtubules and kinesin. *Hum. Mol. Genet.* **23,** 1677–1686 (2014).

201. Defour, A. *et al.* Dysferlin regulates cell membrane repair by facilitating injury-triggered acid sphingomyelinase secretion. *Cell Death Dis.* **5,** e1306 (2014).

202. Han, R. & Campbell, K. P. Dysferlin and muscle membrane repair. *Curr. Opin. Cell Biol.* **19,** 409–416 (2007).

203. Doherty, K. R. *et al.* Normal myoblast fusion requires myoferlin. *Dev. Camb. Engl.* **132,** 5565–5575 (2005).

204. Posey, A. D., Demonbreun, A. & McNally, E. M. Ferlin proteins in myoblast fusion and muscle growth. *Curr. Top. Dev. Biol.* **96,** 203–230 (2011).

205. Normanno, N. *et al.* Epidermal growth factor receptor (EGFR) signaling in cancer. *Gene* **366,** 2–16 (2006).

206. Roberts, P. J. & Der, C. J. Targeting the Raf-MEK-ERK mitogen-activated protein kinase cascade for the treatment of cancer. *Oncogene* **26,** 3291–3310 (2007).

207. Turtoi, A. *et al.* Myoferlin is a key regulator of EGFR activity in breast cancer. *Cancer Res.* **73,** 5438–5448 (2013).

208. Bernatchez, P. N. *et al.* Myoferlin regulates vascular endothelial growth factor receptor-2 stability and function. *J. Biol. Chem.* **282,** 30745–30753 (2007).

209. Bernatchez, P. N., Sharma, A., Kodaman, P. & Sessa, W. C. Myoferlin is critical for endocytosis in endothelial cells. *Am. J. Physiol. Cell Physiol.* **297,** C484-492 (2009).

210. Demonbreun, A. R. *et al.* Myoferlin is required for insulin-like growth factor response and muscle growth. *FASEB J. Off. Publ. Fed. Am. Soc. Exp. Biol.* **24,** 1284–1295 (2010).

211. Fahmy, K. *et al.* Myoferlin plays a key role in VEGFA secretion and impacts tumor-associated angiogenesis in human pancreas cancer. *Int. J. Cancer* **138,** 652–663 (2016).

212. Blomme, A. *et al.* Myoferlin is a novel exosomal protein and functional regulator of cancer-derived exosomes. *Oncotarget* **7,** 83669–83683 (2016).

213. Dulon, D., Safieddine, S., Jones, S. M. & Petit, C. Otoferlin is critical for a highly sensitive and linear calcium-dependent exocytosis at vestibular hair cell ribbon synapses. *J. Neurosci. Off. J. Soc. Neurosci.* **29,** 10474–10487 (2009).

214. Yasunaga, S. *et al.* A mutation in OTOF, encoding otoferlin, a FER-1-like protein, causes DFNB9, a nonsyndromic form of deafness. *Nat. Genet.* **21,** 363–369 (1999).

215. Vogl, C. *et al.* Tryptophan-rich basic protein (WRB) mediates insertion of the tail-anchored protein otoferlin and is required for hair cell exocytosis and hearing. *EMBO J.* **35,** 2536–2552 (2016).

216. Roux, I. *et al.* Otoferlin, defective in a human deafness form, is essential for exocytosis at the auditory ribbon synapse. *Cell* **127,** 277–289 (2006).

217. Beurg, M. *et al.* Calcium- and otoferlin-dependent exocytosis by immature outer hair cells. *J. Neurosci. Off. J. Soc. Neurosci.* **28,** 1798–1803 (2008).

218. Rodríguez-Ballesteros, M. *et al.* Auditory neuropathy in patients carrying mutations in the otoferlin gene (OTOF). *Hum. Mutat.* **22,** 451–456 (2003).

219. Varga, R. *et al.* Non-syndromic recessive auditory neuropathy is the result of mutations in the otoferlin (OTOF) gene. *J. Med. Genet.* **40,** 45–50 (2003).

220. Goutman, J. D. & Glowatzki, E. Time course and calcium dependence of transmitter release at a single ribbon synapse. *Proc. Natl. Acad. Sci. U. S. A.* **104,** 16341–16346 (2007).

221. Varga, R. *et al.* OTOF mutations revealed by genetic analysis of hearing loss families including a potential temperature sensitive auditory neuropathy allele. *J. Med. Genet.* **43,** 576–581 (2006).

222. Wang, D.-Y. *et al.* Screening mutations of OTOF gene in Chinese patients with auditory neuropathy, including a familial case of temperature-sensitive auditory neuropathy. *BMC Med. Genet.* **11,** 79 (2010).

223. Marlin, S. *et al.* Temperature-sensitive auditory neuropathy associated with an otoferlin mutation: Deafening fever! *Biochem. Biophys. Res. Commun.* **394,** 737–742 (2010).

224. Santarelli, R. *et al.* Abnormal cochlear potentials from deaf patients with mutations in the otoferlin gene. *J. Assoc. Res. Otolaryngol. JARO* **10,** 545–556 (2009).

225. Longo-Guess, C., Gagnon, L. H., Bergstrom, D. E. & Johnson, K. R. A missense mutation in the conserved C2B domain of otoferlin causes deafness in a new mouse model of DFNB9. *Hear. Res.* **234,** 21–28 (2007).

226. Mirghomizadeh, F. *et al.* Substitutions in the conserved C2C domain of otoferlin cause DFNB9, a form of nonsyndromic autosomal recessive deafness. *Neurobiol. Dis.* **10,** 157–164 (2002).

227. Tekin, M., Akcayoz, D. & Incesulu, A. A novel missense mutation in a C2 domain of OTOF results in autosomal recessive auditory neuropathy. *Am. J. Med. Genet. A.* **138,** 6–10 (2005).

228. Migliosi, V. *et al.* Q829X, a novel mutation in the gene encoding otoferlin (OTOF), is frequently found in Spanish patients with prelingual non-syndromic hearing loss. *J. Med. Genet.* **39,** 502–506 (2002).

229. Rodríguez-Ballesteros, M. *et al.* A multicenter study on the prevalence and spectrum of mutations in the otoferlin gene (OTOF) in subjects with nonsyndromic hearing impairment and auditory neuropathy. *Hum. Mutat.* **29,** 823–831 (2008).

230. Strenzke, N. *et al.* Hair cell synaptic dysfunction, auditory fatigue and thermal sensitivity in otoferlin Ile515Thr mutants. *EMBO J.* **35,** 2519–2535 (2016).

231. Johnson, C. P. & Chapman, E. R. Otoferlin is a calcium sensor that directly regulates SNARE-mediated membrane fusion. *J. Cell Biol.* **191,** 187–197 (2010).

232. Chatterjee, P. *et al.* Otoferlin deficiency in zebrafish results in defects in balance and hearing: rescue of the balance and hearing phenotype with full-length and truncated forms of mouse otoferlin. *Mol. Cell. Biol.* **35,** 1043–1054 (2015).

233. Pangrsic, T. *et al.* Hearing requires otoferlin-dependent efficient replenishment of synaptic vesicles in hair cells. *Nat. Neurosci.* **13,** 869–876 (2010).

234. Ramakrishnan, N. A., Drescher, M. J. & Drescher, D. G. Direct interaction of otoferlin with syntaxin 1A, SNAP-25, and the L-type voltage-gated calcium channel Cav1.3. *J. Biol. Chem.* **284,** 1364–1372 (2009).

235. Romanos, J. *et al.* Novel OTOF mutations in Brazilian patients with auditory neuropathy. *J. Hum. Genet.* **54,** 382–385 (2009).

236. Matsunaga, T. *et al.* A prevalent founder mutation and genotype-phenotype correlations of OTOF in Japanese patients with auditory neuropathy. *Clin. Genet.* **82,** 425–432 (2012).

237. Chiu, Y.-H. *et al.* Mutations in the OTOF gene in Taiwanese patients with auditory neuropathy. *Audiol. Neurootol.* **15,** 364–374 (2010).

238. Yildirim-Baylan, M. *et al.* Evidence for genotype-phenotype correlation for OTOF mutations. *Int. J. Pediatr. Otorhinolaryngol.* **78,** 950–953 (2014).

239. Padmanarayana, M. *et al.* Characterization of the lipid binding properties of Otoferlin reveals specific interactions between PI(4,5)P2 and the C2C and C2F domains. *Biochemistry (Mosc.)* **53,** 5023–5033 (2014).

240. Helfmann, S. *et al.* The crystal structure of the C_2A domain of otoferlin reveals an unconventional top loop region. *J. Mol. Biol.* **406,** 479–490 (2011).

241. Safieddine, S. & Wenthold, R. J. SNARE complex at the ribbon synapses of cochlear hair cells: analysis of synaptic vesicle- and synaptic membrane-associated proteins. *Eur. J. Neurosci.* **11,** 803–812 (1999).

242. Strenzke, N. *et al.* Complexin-I is required for high-fidelity transmission at the endbulb of Held auditory synapse. *J. Neurosci. Off. J. Soc. Neurosci.* **29,** 7991–8004 (2009).

243. Baig, S. M. *et al.* Loss of Ca(v)1.3 (CACNA1D) function in a human channelopathy with bradycardia and congenital deafness. *Nat. Neurosci.* **14,** 77–84 (2011).

244. Pangršič, T., Reisinger, E. & Moser, T. Otoferlin: a multi-C2 domain protein essential for hearing. *Trends Neurosci.* **35,** 671–680 (2012).

245. Beurg, M. *et al.* Control of exocytosis by synaptotagmins and otoferlin in auditory hair cells. *J. Neurosci. Off. J. Soc. Neurosci.* **30,** 13281–13290 (2010).

246. Bulankina, A. V. & Moser, T. Neural circuit development in the mammalian cochlea. *Physiol. Bethesda Md* **27,** 100–112 (2012).

247. Khimich, D. *et al.* Hair cell synaptic ribbons are essential for synchronous auditory signalling. *Nature* **434,** 889–894 (2005).

248. Grant, L., Yi, E. & Glowatzki, E. Two modes of release shape the postsynaptic response at the inner hair cell ribbon synapse. *J. Neurosci. Off. J. Soc. Neurosci.* **30,** 4210–4220 (2010).

249. Wong, A. B. *et al.* Concurrent maturation of inner hair cell synaptic Ca2+ influx and auditory nerve spontaneous activity around hearing onset in mice. *J. Neurosci. Off. J. Soc. Neurosci.* **33,** 10661–10666 (2013).

250. Reisinger, E. *et al.* Probing the functional equivalence of otoferlin and synaptotagmin 1 in exocytosis. *J. Neurosci. Off. J. Soc. Neurosci.* **31,** 4886–4895 (2011).

251. Johnson, S. L., Forge, A., Knipper, M., Münkner, S. & Marcotti, W. Tonotopic variation in the calcium dependence of neurotransmitter release and vesicle pool replenishment at mammalian auditory ribbon synapses. *J. Neurosci. Off. J. Soc. Neurosci.* **28,** 7670–7678 (2008).

252. Heidrych, P. *et al.* Otoferlin interacts with myosin VI: implications for maintenance of the basolateral synaptic structure of the inner hair cell. *Hum. Mol. Genet.* **18,** 2779–2790 (2009).

253. Roux, I. *et al.* Myosin VI is required for the proper maturation and function of inner hair cell ribbon synapses. *Hum. Mol. Genet.* **18,** 4615–4628 (2009).

254. Heidrych, P. *et al.* Rab8b GTPase, a protein transport regulator, is an interacting partner of otoferlin, defective in a human autosomal recessive deafness form. *Hum. Mol. Genet.* **17,** 3814–3821 (2008).

255. Fuchs, P. A., Glowatzki, E. & Moser, T. The afferent synapse of cochlear hair cells. *Curr. Opin. Neurobiol.* **13,** 452–458 (2003).

256. Moser, T., Neef, A. & Khimich, D. Mechanisms underlying the temporal precision of sound coding at the inner hair cell ribbon synapse. *J. Physiol.* **576,** 55–62 (2006).

257. Vincent, P. F. Y. *et al.* Different CaV1.3 Channel Isoforms Control Distinct Components of the Synaptic Vesicle Cycle in Auditory Inner Hair Cells. *J. Neurosci.* **37,** 2960–2975 (2017).

258. Roberts, W. M., Jacobs, R. A. & Hudspeth, A. J. Colocalization of ion channels involved in frequency selectivity and synaptic transmission at presynaptic active zones of hair cells. *J. Neurosci.* **10,** 3664–3684 (1990).

259. Schmitt, R. O., Dev, P. & Smith, B. H. Electrotonic processing of information by brain cells. *Science* **193,** 114–120 (1976).

260. Kreft, M., Krizaj, D., Grilc, S. & Zorec, R. Properties of exocytotic response in vertebrate photoreceptors. *J. Neurophysiol.* **90,** 218–225 (2003).

261. Parsons, T. D., Lenzi, D., Almers, W. & Roberts, W. M. Calcium-triggered exocytosis and endocytosis in an isolated presynaptic cell: capacitance measurements in saccular hair cells. *Neuron* **13,** 875–883 (1994).

262. Nouvian, R., Beutner, D., Parsons, T. D. & Moser, T. Structure and function of the hair cell ribbon synapse. *J. Membr. Biol.* **209,** 153–165 (2006).

263. Kim, M.-H., Li, G.-L. & von Gersdorff, H. Single Ca2+ channels and exocytosis at sensory synapses. *J. Physiol.* **591,** 3167–3178 (2013).

264. Ohn, T.-L. *et al.* Hair cells use active zones with different voltage dependence of Ca2+ influx to decompose sounds into complementary neural codes. *Proc. Natl. Acad. Sci. U. S. A.* **113,** E4716-4725 (2016).

265. Liberman, M. C. Auditory-nerve response from cats raised in a low-noise chamber. *J. Acoust. Soc. Am.* **63,** 442–455 (1978).

266. Kiang, N. Y., Pfeiffer, R. R., Warr, W. B. & Backus, A. S. Stimulus coding in the cochlear nucleus. *Trans. Am. Otol. Soc.* **53,** 35–58 (1965).

267. Wen, B., Wang, G. I., Dean, I. & Delgutte, B. Dynamic range adaptation to sound level statistics in the auditory nerve. *J. Neurosci. Off. J. Soc. Neurosci.* **29,** 13797–13808 (2009).

268. Geisler, C. D. *From Sound to Synapse: Physiology of the Mammalian Ear*. (Oxford University Press, 1998).

269. Jung, S. *et al.* Disruption of adaptor protein 2μ (AP-2μ) in cochlear hair cells impairs vesicle reloading of synaptic release sites and hearing. *EMBO J.* **34,** 2686–2702 (2015).

270. Dodge, F. A. & Rahamimoff, R. Co-operative action a calcium ions in transmitter release at the neuromuscular junction. *J. Physiol.* **193,** 419–432 (1967).

271. Schmitz, F., Königstorfer, A. & Südhof, T. C. RIBEYE, a component of synaptic ribbons: a protein's journey through evolution provides insight into synaptic ribbon function. *Neuron* **28,** 857–872 (2000).

272. LoGiudice, L. & Matthews, G. The role of ribbons at sensory synapses. *Neurosci. Rev. J. Bringing Neurobiol. Neurol. Psychiatry* **15,** 380–391 (2009).

273. Heidelberger, R., Thoreson, W. B. & Witkovsky, P. Synaptic transmission at retinal ribbon synapses. *Prog. Retin. Eye Res.* **24,** 682–720 (2005).

274. Lenzi, D., Runyeon, J. W., Crum, J., Ellisman, M. H. & Roberts, W. M. Synaptic vesicle populations in saccular hair cells reconstructed by electron tomography. *J. Neurosci. Off. J. Soc. Neurosci.* **19,** 119–132 (1999).

275. Jackman, S. L. *et al.* Role of the synaptic ribbon in transmitting the cone light response. *Nat. Neurosci.* **12,** 303–310 (2009).

276. Reim, K. *et al.* Aberrant function and structure of retinal ribbon synapses in the absence of complexin 3 and complexin 4. *J. Cell Sci.* **122,** 1352–1361 (2009).

277. Bruckner, J. J. *et al.* Fife, a Drosophila Piccolo-RIM homolog, promotes active zone organization and neurotransmitter release. *J. Neurosci. Off. J. Soc. Neurosci.* **32,** 17048–17058 (2012).

278. Wong, A. B. *et al.* Developmental refinement of hair cell synapses tightens the coupling of Ca2+ influx to exocytosis. *EMBO J.* **33,** 247–264 (2014).

279. Dick, O. *et al.* Localization of the presynaptic cytomatrix protein Piccolo at ribbon and conventional synapses in the rat retina: comparison with Bassoon. *J. Comp. Neurol.* **439,** 224–234 (2001).

280. Buran, B. N. *et al.* Onset coding is degraded in auditory nerve fibers from mutant mice lacking synaptic ribbons. *J. Neurosci. Off. J. Soc. Neurosci.* **30,** 7587–7597 (2010).

281. Regus-Leidig, H. *et al.* Identification and immunocytochemical characterization of Piccolino, a novel Piccolo splice variant selectively expressed at sensory ribbon synapses of the eye and ear. *PloS One* **8,** e70373 (2013).

282. tom Dieck, S. *et al.* Molecular dissection of the photoreceptor ribbon synapse: physical interaction of Bassoon and RIBEYE is essential for the assembly of the ribbon complex. *J. Cell Biol.* **168,** 825–836 (2005).

283. Regus-Leidig, H. & Brandstätter, J. H. Structure and function of a complex sensory synapse. *Acta Physiol. Oxf. Engl.* **204,** 479–486 (2012).

284. Muresan, V., Lyass, A. & Schnapp, B. J. The kinesin motor KIF3A is a component of the presynaptic ribbon in vertebrate photoreceptors. *J. Neurosci. Off. J. Soc. Neurosci.* **19,** 1027–1037 (1999).

285. Graf, E. R. *et al.* RIM promotes calcium channel accumulation at active zones of the Drosophila neuromuscular junction. *J. Neurosci. Off. J. Soc. Neurosci.* **32,** 16586–16596 (2012).

286. Schmitz, F. The making of synaptic ribbons: how they are built and what they do. *Neurosci. Rev. J. Bringing Neurobiol. Neurol. Psychiatry* **15,** 611–624 (2009).

287. Jin, Y. & Garner, C. C. Molecular mechanisms of presynaptic differentiation. *Annu. Rev. Cell Dev. Biol.* **24,** 237–262 (2008).

288. Zhai, R. G. & Bellen, H. J. The architecture of the active zone in the presynaptic nerve terminal. *Physiol. Bethesda Md* **19,** 262–270 (2004).

289. Sterling, P. & Matthews, G. Structure and function of ribbon synapses. *Trends Neurosci.* **28,** 20–29 (2005).

290. Liberman, M. C., Dodds, L. W. & Pierce, S. Afferent and efferent innervation of the cat cochlea: quantitative analysis with light and electron microscopy. *J. Comp. Neurol.* **301,** 443–460 (1990).

291. Sobkowicz, H. M., Rose, J. E., Scott, G. L. & Levenick, C. V. Distribution of synaptic ribbons in the developing organ of Corti. *J. Neurocytol.* **15,** 693–714 (1986).

292. Regus-Leidig, H. *et al.* In vivo knockdown of Piccolino disrupts presynaptic ribbon morphology in mouse photoreceptor synapses. *Front. Cell. Neurosci.* **8,** 259 (2014).

293. Mennerick, S. & Matthews, G. Ultrafast exocytosis elicited by calcium current in synaptic terminals of retinal bipolar neurons. *Neuron* **17,** 1241–1249 (1996).

294. von Gersdorff, H. & Matthews, G. Depletion and replenishment of vesicle pools at a ribbon-type synaptic terminal. *J. Neurosci. Off. J. Soc. Neurosci.* **17,** 1919–1927 (1997).

295. Rizzoli, S. O. & Betz, W. J. The structural organization of the readily releasable pool of synaptic vesicles. *Science* **303,** 2037–2039 (2004).

296. Vaithianathan, T. & Matthews, G. Visualizing synaptic vesicle turnover and pool refilling driven by calcium nanodomains at presynaptic active zones of ribbon synapses. *Proc. Natl. Acad. Sci. U. S. A.* **111,** 8655–8660 (2014).

297. Beaumont, V., Llobet, A. & Lagnado, L. Expansion of calcium microdomains regulates fast exocytosis at a ribbon synapse. *Proc. Natl. Acad. Sci. U. S. A.* **102,** 10700–10705 (2005).

298. Sabatini, B. L. & Regehr, W. G. Timing of synaptic transmission. *Annu. Rev. Physiol.* **61,** 521–542 (1999).

299. Robertson, D. & Paki, B. Role of L-type Ca2+ channels in transmitter release from mammalian inner hair cells. II. Single-neuron activity. *J. Neurophysiol.* **87,** 2734–2740 (2002).

300. Platzer, J. *et al.* Congenital deafness and sinoatrial node dysfunction in mice lacking class D L-type Ca2+ channels. *Cell* **102,** 89–97 (2000).

301. Rodriguez-Contreras, A. & Yamoah, E. N. Direct measurement of single-channel Ca(2+) currents in bullfrog hair cells reveals two distinct channel subtypes. *J. Physiol.* **534,** 669–689 (2001).

302. Fettiplace, R. & Fuchs, P. A. Mechanisms of hair cell tuning. *Annu. Rev. Physiol.* **61,** 809–834 (1999).

303. Gomis, A., Burrone, J. & Lagnado, L. Two actions of calcium regulate the supply of releasable vesicles at the ribbon synapse of retinal bipolar cells. *J. Neurosci. Off. J. Soc. Neurosci.* **19,** 6309–6317 (1999).

304. von Gersdorff, H., Vardi, E., Matthews, G. & Sterling, P. Evidence that vesicles on the synaptic ribbon of retinal bipolar neurons can be rapidly released. *Neuron* **16,** 1221–1227 (1996).

305. Moser, T. & Beutner, D. Kinetics of exocytosis and endocytosis at the cochlear inner hair cell afferent synapse of the mouse. *Proc. Natl. Acad. Sci. U. S. A.* **97,** 883–888 (2000).

306. von Gersdorff, H. & Matthews, G. Dynamics of synaptic vesicle fusion and membrane retrieval in synaptic terminals. *Nature* **367,** 735–739 (1994).

307. Mennerick, S. & Matthews, G. Ultrafast exocytosis elicited by calcium current in synaptic terminals of retinal bipolar neurons. *Neuron* **17,** 1241–1249 (1996).

308. von Gersdorff, H., Sakaba, T., Berglund, K. & Tachibana, M. Submillisecond kinetics of glutamate release from a sensory synapse. *Neuron* **21,** 1177–1188 (1998).

309. Burrone, J. & Lagnado, L. Synaptic depression and the kinetics of exocytosis in retinal bipolar cells. *J. Neurosci. Off. J. Soc. Neurosci.* **20,** 568–578 (2000).

310. Burrone, J., Neves, G., Gomis, A., Cooke, A. & Lagnado, L. Endogenous calcium buffers regulate fast exocytosis in the synaptic terminal of retinal bipolar cells. *Neuron* **33,** 101–112 (2002).

311. Singer, J. H. & Diamond, J. S. Sustained Ca2+ entry elicits transient postsynaptic currents at a retinal ribbon synapse. *J. Neurosci. Off. J. Soc. Neurosci.* **23,** 10923–10933 (2003).

312. Singer, J. H. & Diamond, J. S. Vesicle depletion and synaptic depression at a mammalian ribbon synapse. *J. Neurophysiol.* **95,** 3191–3198 (2006).

313. Snellman, J., Zenisek, D. & Nawy, S. Switching between transient and sustained signalling at the rod bipolar-AII amacrine cell synapse of the mouse retina. *J. Physiol.* **587,** 2443–2455 (2009).

314. Snellman, J. *et al.* Acute destruction of the synaptic ribbon reveals a role for the ribbon in vesicle priming. *Nat. Neurosci.* **14,** 1135–1141 (2011).

315. Spassova, M. A. *et al.* Evidence that rapid vesicle replenishment of the synaptic ribbon mediates recovery from short-term adaptation at the hair cell afferent synapse. *J. Assoc. Res. Otolaryngol. JARO* **5,** 376–390 (2004).

316. Edmonds, B. W., Gregory, F. D. & Schweizer, F. E. Evidence that fast exocytosis can be predominantly mediated by vesicles not docked at active zones in frog saccular hair cells. *J. Physiol.* **560,** 439–450 (2004).

317. Brandt, A., Khimich, D. & Moser, T. Few CaV1.3 channels regulate the exocytosis of a synaptic vesicle at the hair cell ribbon synapse. *J. Neurosci. Off. J. Soc. Neurosci.* **25,** 11577–11585 (2005).

318. Miller, M. R. & Beck, J. Auditory hair cell innervational patterns in lizards. *J. Comp. Neurol.* **271,** 604–628 (1988).

319. Kiang, N. Y., Rho, J. M., Northrop, C. C., Liberman, M. C. & Ryugo, D. K. Hair-cell innervation by spiral ganglion cells in adult cats. *Science* **217,** 175–177 (1982).

320. Sun, J.-Y., Wu, X.-S. & Wu, L.-G. Single and multiple vesicle fusion induce different rates of endocytosis at a central synapse. *Nature* **417,** 555–559 (2002).

321. Marcotti, W., Johnson, S. L., Holley, M. C. & Kros, C. J. Developmental changes in the expression of potassium currents of embryonic, neonatal and mature mouse inner hair cells. *J. Physiol.* **548,** 383–400 (2003).

322. Duncker, S. V. *et al.* Otoferlin couples to clathrin-mediated endocytosis in mature cochlear inner hair cells. *J. Neurosci. Off. J. Soc. Neurosci.* **33,** 9508–9519 (2013).

323. Jahn, R. & Scheller, R. H. SNAREs — engines for membrane fusion. *Nat. Rev. Mol. Cell Biol.* **7,** 631–643 (2006).

324. Ostrowicz, C. W., Meiringer, C. T. A. & Ungermann, C. Yeast vacuole fusion: a model system for eukaryotic endomembrane dynamics. *Autophagy* **4,** 5–19 (2008).

325. McNew, J. A. *et al.* Compartmental specificity of cellular membrane fusion encoded in SNARE proteins. *Nature* **407,** 153–159 (2000).

326. Fukuda, R. *et al.* Functional architecture of an intracellular membrane t-SNARE. *Nature* **407,** 198–202 (2000).

327. Jahn, R., Lang, T. & Südhof, T. C. Membrane fusion. *Cell* **112,** 519–533 (2003).

328. Li, F. *et al.* Energetics and dynamics of SNAREpin folding across lipid bilayers. *Nat. Struct. Mol. Biol.* **14,** 890–896 (2007).

329. Kesavan, J., Borisovska, M. & Bruns, D. v-SNARE actions during Ca(2+)-triggered exocytosis. *Cell* **131,** 351–363 (2007).

330. McNew, J. A., Weber, T., Engelman, D. M., Söllner, T. H. & Rothman, J. E. The length of the flexible SNAREpin juxtamembrane region is a critical determinant of SNARE-dependent fusion. *Mol. Cell* **4,** 415–421 (1999).

331. Condliffe, S. B., Corradini, I., Pozzi, D., Verderio, C. & Matteoli, M. Endogenous SNAP-25 regulates native voltage-gated calcium channels in glutamatergic neurons. *J. Biol. Chem.* **285,** 24968–24976 (2010).

332. Gonzalo, S., Greentree, W. K. & Linder, M. E. SNAP-25 is targeted to the plasma membrane through a novel membrane-binding domain. *J. Biol. Chem.* **274,** 21313–21318 (1999).

333. Takamori, S. *et al.* Molecular anatomy of a trafficking organelle. *Cell* **127,** 831–846 (2006).

334. Schoch, S. *et al.* SNARE function analyzed in synaptobrevin/VAMP knockout mice. *Science* **294,** 1117–1122 (2001).

335. Fasshauer, D. Structural insights into the SNARE mechanism. *Biochim. Biophys. Acta* **1641,** 87–97 (2003).

336. Sutton, R. B., Fasshauer, D., Jahn, R. & Brunger, A. T. Crystal structure of a SNARE complex involved in synaptic exocytosis at 2.4 A resolution. *Nature* **395,** 347–353 (1998).

337. Weber, T. *et al.* SNAREpins: minimal machinery for membrane fusion. *Cell* **92,** 759–772 (1998).

338. Poirier, M. A. *et al.* The synaptic SNARE complex is a parallel four-stranded helical bundle. *Nat. Struct. Biol.* **5,** 765–769 (1998).

339. Katz, L., Hanson, P. I., Heuser, J. E. & Brennwald, P. Genetic and morphological analyses reveal a critical interaction between the C-termini of two SNARE proteins and a parallel four helical arrangement for the exocytic SNARE complex. *EMBO J.* **17,** 6200–6209 (1998).

340. Lin, R. C. & Scheller, R. H. Structural organization of the synaptic exocytosis core complex. *Neuron* **19,** 1087–1094 (1997).

341. Poirier, M. A. *et al.* Protease resistance of syntaxin.SNAP-25.VAMP complexes. Implications for assembly and structure. *J. Biol. Chem.* **273,** 11370–11377 (1998).

342. Fasshauer, D., Otto, H., Eliason, W. K., Jahn, R. & Brünger, A. T. Structural changes are associated with soluble N-ethylmaleimide-sensitive fusion protein attachment protein receptor complex formation. *J. Biol. Chem.* **272,** 28036–28041 (1997).

343. Fasshauer, D., Sutton, R. B., Brunger, A. T. & Jahn, R. Conserved structural features of the synaptic fusion complex: SNARE proteins reclassified as Q- and R-SNAREs. *Proc. Natl. Acad. Sci. U. S. A.* **95,** 15781–15786 (1998).

344. Brunger, A. T. Structure and function of SNARE and SNARE-interacting proteins. *Q. Rev. Biophys.* **38,** 1–47 (2005).

345. Söllner, T. *et al.* SNAP receptors implicated in vesicle targeting and fusion. *Nature* **362,** 318–324 (1993).

346. McMahon, H. T. & Südhof, T. C. Synaptic core complex of synaptobrevin, syntaxin, and SNAP25 forms high affinity alpha-SNAP binding site. *J. Biol. Chem.* **270,** 2213–2217 (1995).

347. Bock, J. B., Matern, H. T., Peden, A. A. & Scheller, R. H. A genomic perspective on membrane compartment organization. *Nature* **409,** 839–841 (2001).

348. Terrian, D. M. & White, M. K. Phylogenetic analysis of membrane trafficking proteins: a family reunion and secondary structure predictions. *Eur. J. Cell Biol.* **73,** 198–204 (1997).

349. Weimbs, T. *et al.* A conserved domain is present in different families of vesicular fusion proteins: a new superfamily. *Proc. Natl. Acad. Sci. U. S. A.* **94,** 3046–3051 (1997).

350. Weimbs, T., Mostov, K., Low, S. H. & Hofmann, K. A model for structural similarity between different SNARE complexes based on sequence relationships. *Trends Cell Biol.* **8,** 260–262 (1998).

351. Fasshauer, D., Antonin, W., Margittai, M., Pabst, S. & Jahn, R. Mixed and non-cognate SNARE complexes. Characterization of assembly and biophysical properties. *J. Biol. Chem.* **274,** 15440–15446 (1999).

352. Yang, B. *et al.* SNARE interactions are not selective. Implications for membrane fusion specificity. *J. Biol. Chem.* **274,** 5649–5653 (1999).

353. Calakos, N., Bennett, M. K., Peterson, K. E. & Scheller, R. H. Protein-protein interactions contributing to the specificity of intracellular vesicular trafficking. *Science* **263,** 1146–1149 (1994).

354. Foster, L. J. *et al.* Binary interactions of the SNARE proteins syntaxin-4, SNAP23, and VAMP-2 and their regulation by phosphorylation. *Biochemistry (Mosc.)* **37,** 11089–11096 (1998).

355. Südhof, T. C. & Rothman, J. E. Membrane fusion: grappling with SNARE and SM proteins. *Science* **323,** 474–477 (2009).

356. Hanson, P. I., Roth, R., Morisaki, H., Jahn, R. & Heuser, J. E. Structure and conformational changes in NSF and its membrane receptor complexes visualized by quick-freeze/deep-etch electron microscopy. *Cell* **90,** 523–535 (1997).

357. Hua, S. Y. & Charlton, M. P. Activity-dependent changes in partial VAMP complexes during neurotransmitter release. *Nat. Neurosci.* **2,** 1078–1083 (1999).

358. Xu, T. *et al.* Inhibition of SNARE complex assembly differentially affects kinetic components of exocytosis. *Cell* **99,** 713–722 (1999).

359. Chen, Y. A., Scales, S. J. & Scheller, R. H. Sequential SNARE assembly underlies priming and triggering of exocytosis. *Neuron* **30,** 161–170 (2001).

360. Melia, T. J. *et al.* Regulation of membrane fusion by the membrane-proximal coil of the t-SNARE during zippering of SNAREpins. *J. Cell Biol.* **158,** 929–940 (2002).

361. Pobbati, A. V., Stein, A. & Fasshauer, D. N- to C-terminal SNARE complex assembly promotes rapid membrane fusion. *Science* **313,** 673–676 (2006).

362. Gipson, P. *et al.* Morphologies of synaptic protein membrane fusion interfaces. *Proc. Natl. Acad. Sci. U. S. A.* **114,** 9110–9115 (2017).

363. Kozlovsky, Y. & Kozlov, M. M. Stalk model of membrane fusion: solution of energy crisis. *Biophys. J.* **82,** 882–895 (2002).

364. Rothman, J. E. Mechanisms of intracellular protein transport. *Nature* **372,** 55–63 (1994).

365. Whiteheart, S. W. *et al.* N-ethylmaleimide-sensitive fusion protein: a trimeric ATPase whose hydrolysis of ATP is required for membrane fusion. *J. Cell Biol.* **126,** 945–954 (1994).

366. Nagiec, E. E., Bernstein, A. & Whiteheart, S. W. Each domain of the N-ethylmaleimide-sensitive fusion protein contributes to its transport activity. *J. Biol. Chem.* **270,** 29182–29188 (1995).

367. Morgan, A., Dimaline, R. & Burgoyne, R. D. The ATPase activity of N-ethylmaleimide-sensitive fusion protein (NSF) is regulated by soluble NSF attachment proteins. *J. Biol. Chem.* **269,** 29347–29350 (1994).

368. Hohl, T. M. *et al.* Arrangement of subunits in 20 S particles consisting of NSF, SNAPs, and SNARE complexes. *Mol. Cell* **2,** 539–548 (1998).

369. Verhage, M. *et al.* Synaptic assembly of the brain in the absence of neurotransmitter secretion. *Science* **287,** 864–869 (2000).

370. Barclay, J. W. *et al.* Phosphorylation of Munc18 by protein kinase C regulates the kinetics of exocytosis. *J. Biol. Chem.* **278,** 10538–10545 (2003).

371. Dulubova, I. *et al.* A conformational switch in syntaxin during exocytosis: role of munc18. *EMBO J.* **18,** 4372–4382 (1999).

372. Augustin, I., Rosenmund, C., Südhof, T. C. & Brose, N. Munc13-1 is essential for fusion competence of glutamatergic synaptic vesicles. *Nature* **400,** 457–461 (1999).

373. Richmond, J. E., Weimer, R. M. & Jorgensen, E. M. An open form of syntaxin bypasses the requirement for UNC-13 in vesicle priming. *Nature* **412,** 338–341 (2001).

374. Ma, C., Su, L., Seven, A. B., Xu, Y. & Rizo, J. Reconstitution of the vital functions of Munc18 and Munc13 in neurotransmitter release. *Science* **339,** 421–425 (2013).

375. Smyth, A. M., Duncan, R. R. & Rickman, C. Munc18-1 and syntaxin1: unraveling the interactions between the dynamic duo. *Cell. Mol. Neurobiol.* **30,** 1309–1313 (2010).

376. Shi, L., Kümmel, D., Coleman, J., Melia, T. J. & Giraudo, C. G. Dual roles of Munc18-1 rely on distinct binding modes of the central cavity with Stx1A and SNARE complex. *Mol. Biol. Cell* **22,** 4150–4160 (2011).

377. Lai, Y. *et al.* Molecular Mechanisms of Synaptic Vesicle Priming by Munc13 and Munc18. *Neuron* **95,** 591–607.e10 (2017).

378. Bracher, A., Kadlec, J., Betz, H. & Weissenhorn, W. X-ray structure of a neuronal complexin-SNARE complex from squid. *J. Biol. Chem.* **277,** 26517–26523 (2002).

379. Chen, X. *et al.* Three-dimensional structure of the complexin/SNARE complex. *Neuron* **33,** 397–409 (2002).

380. Giraudo, C. G., Eng, W. S., Melia, T. J. & Rothman, J. E. A clamping mechanism involved in SNARE-dependent exocytosis. *Science* **313,** 676–680 (2006).

381. Schaub, J. R., Lu, X., Doneske, B., Shin, Y.-K. & McNew, J. A. Hemifusion arrest by complexin is relieved by Ca2+-synaptotagmin I. *Nat. Struct. Mol. Biol.* **13,** 748–750 (2006).

382. Saisu, H., Ibaraki, K., Yamaguchi, T., Sekine, Y. & Abe, T. Monoclonal antibodies immunoprecipitating omega-conotoxin-sensitive calcium channel molecules recognize two novel proteins localized in the nervous system. *Biochem. Biophys. Res. Commun.* **181,** 59–66 (1991).

383. Bennett, M. K., Calakos, N. & Scheller, R. H. Syntaxin: a synaptic protein implicated in docking of synaptic vesicles at presynaptic active zones. *Science* **257,** 255–259 (1992).

384. Yoshida, A. *et al.* HPC-1 is associated with synaptotagmin and omega-conotoxin receptor. *J. Biol. Chem.* **267,** 24925–24928 (1992).

385. Leveque, C. *et al.* Interaction of cysteine string proteins with the alpha1A subunit of the P/Q-type calcium channel. *J. Biol. Chem.* **273,** 13488–13492 (1998).

386. Sheng, Z. H., Rettig, J., Takahashi, M. & Catterall, W. A. Identification of a syntaxin-binding site on N-type calcium channels. *Neuron* **13,** 1303–1313 (1994).

387. Rettig, J. *et al.* Isoform-specific interaction of the alpha1A subunits of brain Ca2+ channels with the presynaptic proteins syntaxin and SNAP-25. *Proc. Natl. Acad. Sci. U. S. A.* **93,** 7363–7368 (1996).

388. Wiser, O., Bennett, M. K. & Atlas, D. Functional interaction of syntaxin and SNAP-25 with voltage-sensitive L- and N-type Ca2+ channels. *EMBO J.* **15,** 4100–4110 (1996).

389. Zhong, H., Yokoyama, C. T., Scheuer, T. & Catterall, W. A. Reciprocal regulation of P/Q-type Ca2+ channels by SNAP-25, syntaxin and synaptotagmin. *Nat. Neurosci.* **2,** 939–941 (1999).

390. Magga, J. M., Jarvis, S. E., Arnot, M. I., Zamponi, G. W. & Braun, J. E. Cysteine string protein regulates G protein modulation of N-type calcium channels. *Neuron* **28,** 195–204 (2000).

391. Coppola, T. *et al.* Direct interaction of the Rab3 effector RIM with Ca2+ channels, SNAP-25, and synaptotagmin. *J. Biol. Chem.* **276,** 32756–32762 (2001).

392. Hibino, H. *et al.* RIM binding proteins (RBPs) couple Rab3-interacting molecules (RIMs) to voltage-gated Ca(2+) channels. *Neuron* **34,** 411–423 (2002).

393. Wiser, O. *et al.* The voltage sensitive Lc-type Ca2+ channel is functionally coupled to the exocytotic machinery. *Proc. Natl. Acad. Sci. U. S. A.* **96,** 248–253 (1999).

394. Catterall, W. A. Voltage-Gated Calcium Channels. *Cold Spring Harb. Perspect. Biol.* **3,** a003947 (2011).

395. Yang, S.-N. & Berggren, P.-O. The role of voltage-gated calcium channels in pancreatic beta-cell physiology and pathophysiology. *Endocr. Rev.* **27,** 621–676 (2006).

396. Reuter, H. Properties of two inward membrane currents in the heart. *Annu. Rev. Physiol.* **41,** 413–424 (1979).

397. Tsien, R. W. Calcium channels in excitable cell membranes. *Annu. Rev. Physiol.* **45,** 341–358 (1983).

398. Bers, D. M. Cardiac excitation-contraction coupling. *Nature* **415,** 198–205 (2002).

399. Catterall, W. A. Excitation-contraction coupling in vertebrate skeletal muscle: a tale of two calcium channels. *Cell* **64,** 871–874 (1991).

400. Tanabe, T. *et al.* Structure and function of voltage-dependent calcium channels from muscle. *Ann. N. Y. Acad. Sci.* **707,** 81–86 (1993).

401. Catterall, W. A. & Few, A. P. Calcium channel regulation and presynaptic plasticity. *Neuron* **59,** 882–901 (2008).

402. Tsien, R. W., Lipscombe, D., Madison, D. V., Bley, K. R. & Fox, A. P. Multiple types of neuronal calcium channels and their selective modulation. *Trends Neurosci.* **11,** 431–438 (1988).

403. Dunlap, K., Luebke, J. I. & Turner, T. J. Exocytotic Ca2+ channels in mammalian central neurons. *Trends Neurosci.* **18,** 89–98 (1995).

404. Pumplin, D. W., Reese, T. S. & Llinás, R. Are the presynaptic membrane particles the calcium channels? *Proc. Natl. Acad. Sci. U. S. A.* **78,** 7210–7213 (1981).

405. Tanabe, T. *et al.* Primary structure of the receptor for calcium channel blockers from skeletal muscle. *Nature* **328,** 313–318 (1987).

406. Takahashi, M., Seagar, M. J., Jones, J. F., Reber, B. F. & Catterall, W. A. Subunit structure of dihydropyridine-sensitive calcium channels from skeletal muscle. *Proc. Natl. Acad. Sci. U. S. A.* **84,** 5478–5482 (1987).

407. Ertel, E. A. *et al.* Nomenclature of voltage-gated calcium channels. *Neuron* **25,** 533–535 (2000).

408. Snutch, T. P. & Reiner, P. B. Ca2+ channels: diversity of form and function. *Curr. Opin. Neurobiol.* **2,** 247–253 (1992).

409. Perez-Reyes, E. *et al.* Molecular characterization of a neuronal low-voltage-activated T-type calcium channel. *Nature* **391,** 896–900 (1998).

410. Hockerman, G. H. *et al.* Construction of a high-affinity receptor site for dihydropyridine agonists and antagonists by single amino acid substitutions in a non-L-type Ca2+ channel. *Proc. Natl. Acad. Sci. U. S. A.* **94,** 14906–14911 (1997).

411. De Jongh, K. S., Warner, C. & Catterall, W. A. Subunits of purified calcium channels. Alpha 2 and delta are encoded by the same gene. *J. Biol. Chem.* **265,** 14738–14741 (1990).

412. Jay, S. D. *et al.* Primary structure of the gamma subunit of the DHP-sensitive calcium channel from skeletal muscle. *Science* **248,** 490–492 (1990).

413. Gurnett, C. A., De Waard, M. & Campbell, K. P. Dual function of the voltage-dependent Ca2+ channel alpha 2 delta subunit in current stimulation and subunit interaction. *Neuron* **16,** 431–440 (1996).

414. Davies, A. *et al.* The alpha2delta subunits of voltage-gated calcium channels form GPI-anchored proteins, a posttranslational modification essential for function. *Proc. Natl. Acad. Sci. U. S. A.* **107,** 1654–1659 (2010).

415. Cole, R. L. *et al.* Differential distribution of voltage-gated calcium channel alpha-2 delta (alpha2delta) subunit mRNA-containing cells in the rat central nervous system and the dorsal root ganglia. *J. Comp. Neurol.* **491,** 246–269 (2005).

416. Letts, V. A. *et al.* The mouse stargazer gene encodes a neuronal Ca2+-channel gamma subunit. *Nat. Genet.* **19,** 340–347 (1998).

417. Ruth, P. *et al.* Primary structure of the beta subunit of the DHP-sensitive calcium channel from skeletal muscle. *Science* **245,** 1115–1118 (1989).

418. Atlas, D., Wiser, O. & Trus, M. The voltage-gated Ca2+ channel is the Ca2+ sensor of fast neurotransmitter release. *Cell. Mol. Neurobiol.* **21,** 717–731 (2001).

419. Atlas, D. Functional and physical coupling of voltage-sensitive calcium channels with exocytotic proteins: ramifications for the secretion mechanism. *J. Neurochem.* **77,** 972–985 (2001).

420. Hagiwara, S., Ozawa, S. & Sand, O. Voltage clamp analysis of two inward current mechanisms in the egg cell membrane of a starfish. *J. Gen. Physiol.* **65,** 617–644 (1975).

421. Carbone, E. & Lux, H. D. A low voltage-activated, fully inactivating Ca channel in vertebrate sensory neurones. *Nature* **310,** 501–502 (1984).

422. Fedulova, S. A., Kostyuk, P. G. & Veselovsky, N. S. Two types of calcium channels in the somatic membrane of new-born rat dorsal root ganglion neurones. *J. Physiol.* **359,** 431–446 (1985).

423. Nowycky, M. C., Fox, A. P. & Tsien, R. W. Three types of neuronal calcium channel with different calcium agonist sensitivity. *Nature* **316,** 440–443 (1985).

424. Robitaille, R., Adler, E. M. & Charlton, M. P. Strategic location of calcium channels at transmitter release sites of frog neuromuscular synapses. *Neuron* **5,** 773–779 (1990).

425. Westenbroek, R. E. *et al.* Biochemical properties and subcellular distribution of an N-type calcium channel alpha 1 subunit. *Neuron* **9,** 1099–1115 (1992).

426. Westenbroek, R. E. *et al.* Immunochemical identification and subcellular distribution of the alpha 1A subunits of brain calcium channels. *J. Neurosci. Off. J. Soc. Neurosci.* **15,** 6403–6418 (1995).

427. Mintz, I. M., Sabatini, B. L. & Regehr, W. G. Calcium control of transmitter release at a cerebellar synapse. *Neuron* **15,** 675–688 (1995).

428. Randall, A. & Tsien, R. W. Pharmacological dissection of multiple types of Ca2+ channel currents in rat cerebellar granule neurons. *J. Neurosci. Off. J. Soc. Neurosci.* **15,** 2995–3012 (1995).

429. Beutner, D. & Moser, T. The presynaptic function of mouse cochlear inner hair cells during development of hearing. *J. Neurosci. Off. J. Soc. Neurosci.* **21,** 4593–4599 (2001).

430. Glowatzki, E. & Fuchs, P. A. Transmitter release at the hair cell ribbon synapse. *Nat. Neurosci.* **5,** 147–154 (2002).

431. Johnson, S. L., Marcotti, W. & Kros, C. J. Increase in efficiency and reduction in Ca2+ dependence of exocytosis during development of mouse inner hair cells. *J. Physiol.* **563,** 177–191 (2005).

432. Inoue, A., Obata, K. & Akagawa, K. Cloning and sequence analysis of cDNA for a neuronal cell membrane antigen, HPC-1. *J. Biol. Chem.* **267,** 10613–10619 (1992).

433. Martin-Moutot, N. *et al.* Interaction of SNARE complexes with P/Q-type calcium channels in rat cerebellar synaptosomes. *J. Biol. Chem.* **271,** 6567–6570 (1996).

434. Charvin, N. *et al.* Direct interaction of the calcium sensor protein synaptotagmin I with a cytoplasmic domain of the alpha1A subunit of the P/Q-type calcium channel. *EMBO J.* **16,** 4591–4596 (1997).

435. Young, S. M. & Neher, E. Synaptotagmin has an essential function in synaptic vesicle positioning for synchronous release in addition to its role as a calcium sensor. *Neuron* **63,** 482–496 (2009).

436. Mochida, S., Sheng, Z. H., Baker, C., Kobayashi, H. & Catterall, W. A. Inhibition of neurotransmission by peptides containing the synaptic protein interaction site of N-type Ca2+ channels. *Neuron* **17,** 781–788 (1996).

437. Yokoyama, C. T., Sheng, Z. H. & Catterall, W. A. Phosphorylation of the synaptic protein interaction site on N-type calcium channels inhibits interactions with SNARE proteins. *J. Neurosci. Off. J. Soc. Neurosci.* **17,** 6929–6938 (1997).

438. Bezprozvanny, I., Scheller, R. H. & Tsien, R. W. Functional impact of syntaxin on gating of N-type and Q-type calcium channels. *Nature* **378,** 623–626 (1995).

439. Kaneko, S. *et al.* Identification and Characterization of Novel Human Cav2.2 (α1B) Calcium Channel Variants Lacking the Synaptic Protein Interaction Site. *J. Neurosci.* **22,** 82–92 (2002).

440. Szabo, Z., Obermair, G. J., Cooper, C. B., Zamponi, G. W. & Flucher, B. E. Role of the synprint site in presynaptic targeting of the calcium channel CaV2.2 in hippocampal neurons. *Eur. J. Neurosci.* **24,** 709–718 (2006).

441. Brandt, A., Striessnig, J. & Moser, T. CaV1.3 channels are essential for development and presynaptic activity of cochlear inner hair cells. *J. Neurosci. Off. J. Soc. Neurosci.* **23,** 10832–10840 (2003).

442. Rutherford, M. A., Chapochnikov, N. M. & Moser, T. Spike encoding of neurotransmitter release timing by spiral ganglion neurons of the cochlea. *J. Neurosci. Off. J. Soc. Neurosci.* **32,** 4773–4789 (2012).

443. Zenisek, D., Davila, V., Wan, L. & Almers, W. Imaging calcium entry sites and ribbon structures in two presynaptic cells. *J. Neurosci. Off. J. Soc. Neurosci.* **23,** 2538–2548 (2003).

444. Stanley, E. F. Single calcium channels and acetylcholine release at a presynaptic nerve terminal. *Neuron* **11,** 1007–1011 (1993).

445. Schroeder, T. J., Jankowski, J. A., Senyshyn, J., Holz, R. W. & Wightman, R. M. Zones of exocytotic release on bovine adrenal medullary cells in culture. *J. Biol. Chem.* **269,** 17215–17220 (1994).

446. Bokvist, K., Eliasson, L., Ammälä, C., Renström, E. & Rorsman, P. Co-localization of L-type Ca2+ channels and insulin-containing secretory granules and its

significance for the initiation of exocytosis in mouse pancreatic B-cells. *EMBO J.* **14,** 50–57 (1995).

447. Robinson, I. M., Finnegan, J. M., Monck, J. R., Wightman, R. M. & Fernandez, J. M. Colocalization of calcium entry and exocytotic release sites in adrenal chromaffin cells. *Proc. Natl. Acad. Sci. U. S. A.* **92,** 2474–2478 (1995).

448. Elhamdani, A., Zhou, Z. & Artalejo, C. R. Timing of dense-core vesicle exocytosis depends on the facilitation L-type Ca channel in adrenal chromaffin cells. *J. Neurosci. Off. J. Soc. Neurosci.* **18,** 6230–6240 (1998).

449. Macleod, G. T., Gan, J. & Bennett, M. R. Vesicle-associated proteins and quantal release at single active zones of amphibian (Bufo marinus) motor-nerve terminals. *J. Neurophysiol.* **82,** 1133–1146 (1999).

450. Finnegan, J. M. *et al.* Vesicular quantal size measured by amperometry at chromaffin, mast, pheochromocytoma, and pancreatic beta-cells. *J. Neurochem.* **66,** 1914–1923 (1996).

451. Lewis, R. S. & Hudspeth, A. J. Voltage- and ion-dependent conductances in solitary vertebrate hair cells. *Nature* **304,** 538–541 (1983).

452. Art, J. J. & Fettiplace, R. Variation of membrane properties in hair cells isolated from the turtle cochlea. *J. Physiol.* **385,** 207–242 (1987).

453. Zenisek, D., Horst, N. K., Merrifield, C., Sterling, P. & Matthews, G. Visualizing synaptic ribbons in the living cell. *J. Neurosci. Off. J. Soc. Neurosci.* **24,** 9752–9759 (2004).

454. Frank, T., Khimich, D., Neef, A. & Moser, T. Mechanisms contributing to synaptic Ca2+ signals and their heterogeneity in hair cells. *Proc. Natl. Acad. Sci.* **106,** 4483–4488 (2009).

455. Zampini, V. *et al.* Elementary properties of CaV1.3 Ca(2+) channels expressed in mouse cochlear inner hair cells. *J. Physiol.* **588,** 187–199 (2010).

456. Issa, N. P. & Hudspeth, A. J. Clustering of Ca2+ channels and Ca(2+)-activated K+ channels at fluorescently labeled presynaptic active zones of hair cells. *Proc. Natl. Acad. Sci. U. S. A.* **91,** 7578–7582 (1994).

457. Martinez-Dunst, C., Michaels, R. L. & Fuchs, P. A. Release sites and calcium channels in hair cells of the chick's cochlea. *J. Neurosci. Off. J. Soc. Neurosci.* **17,** 9133–9144 (1997).

458. Sheets, L., Kindt, K. S. & Nicolson, T. Presynaptic CaV1.3 channels regulate synaptic ribbon size and are required for synaptic maintenance in sensory hair cells. *J. Neurosci. Off. J. Soc. Neurosci.* **32,** 17273–17286 (2012).

459. Bollmann, J. H., Sakmann, B. & Borst, J. G. G. Calcium Sensitivity of Glutamate Release in a Calyx-Type Terminal. *Science* **289,** 953–957 (2000).

460. Schneggenburger, R. & Neher, E. Intracellular calcium dependence of transmitter release rates at a fast central synapse. *Nature* **406,** 35022702 (2000).

461. Torrecillas, A., Laynez, J., Menéndez, M., Corbalán-García, S. & Gómez-Fernández, J. C. Calorimetric study of the interaction of the C2 domains of classical protein kinase C isoenzymes with Ca2+ and phospholipids. *Biochemistry (Mosc.)* **43,** 11727–11739 (2004).

462. Balkema, G. W. A synaptic antigen (B16) is localized in retinal synaptic ribbons. *J. Comp. Neurol.* **312,** 573–583 (1991).

463. Frank, T. *et al.* Bassoon and the synaptic ribbon organize Ca^2+ channels and vesicles to add release sites and promote refilling. *Neuron* **68,** 724–738 (2010).

464. Zampini, V. *et al.* Burst activity and ultrafast activation kinetics of CaV1.3 Ca^{2+} channels support presynaptic activity in adult gerbil hair cell ribbon synapses. *J. Physiol.* **591,** 3811–3820 (2013).

465. Dixon, R. E., Yuan, C., Cheng, E. P., Navedo, M. F. & Santana, L. F. Ca2+ signaling amplification by oligomerization of L-type Cav1.2 channels. *Proc. Natl. Acad. Sci. U. S. A.* **109,** 1749–1754 (2012).

466. Calin-Jageman, I. & Lee, A. Ca(v)1 L-type Ca2+ channel signaling complexes in neurons. *J. Neurochem.* **105,** 573–583 (2008).

467. Meinrenken, C. J., Borst, J. G. G. & Sakmann, B. Calcium secretion coupling at calyx of Held governed by nonuniform channel-vesicle topography. *J. Neurosci. Off. J. Soc. Neurosci.* **22,** 1648–1667 (2002).

468. Bucurenciu, I., Kulik, A., Schwaller, B., Frotscher, M. & Jonas, P. Nanodomain coupling between Ca2+ channels and Ca2+ sensors promotes fast and efficient transmitter release at a cortical GABAergic synapse. *Neuron* **57,** 536–545 (2008).

469. Borst, J. G. & Sakmann, B. Calcium influx and transmitter release in a fast CNS synapse. *Nature* **383,** 431–434 (1996).

470. Roberts, W. M. Localization of calcium signals by a mobile calcium buffer in frog saccular hair cells. *J. Neurosci. Off. J. Soc. Neurosci.* **14,** 3246–3262 (1994).

471. Tucker, T. & Fettiplace, R. Confocal imaging of calcium microdomains and calcium extrusion in turtle hair cells. *Neuron* **15,** 1323–1335 (1995).

472. Li, G.-L., Keen, E., Andor-Ardó, D., Hudspeth, A. J. & von Gersdorff, H. The unitary event underlying multiquantal EPSCs at a hair cell's ribbon synapse. *J. Neurosci. Off. J. Soc. Neurosci.* **29,** 7558–7568 (2009).

473. Schnee, M. E., Lawton, D. M., Furness, D. N., Benke, T. A. & Ricci, A. J. Auditory hair cell-afferent fiber synapses are specialized to operate at their best frequencies. *Neuron* **47,** 243–254 (2005).

474. Graydon, C. W., Cho, S., Li, G.-L., Kachar, B. & von Gersdorff, H. Sharp Ca^{2+} nanodomains beneath the ribbon promote highly synchronous multivesicular release at hair cell synapses. *J. Neurosci. Off. J. Soc. Neurosci.* **31,** 16637–16650 (2011).

475. Keen, E. C. & Hudspeth, A. J. Transfer characteristics of the hair cell's afferent synapse. *Proc. Natl. Acad. Sci. U. S. A.* **103,** 5537–5542 (2006).

476. Russell, I. J. & Sellick, P. M. Intracellular studies of hair cells in the mammalian cochlea. *J. Physiol.* **284,** 261–290 (1978).

477. Meyer, A. C. & Moser, T. Structure and function of cochlear afferent innervation. *Curr. Opin. Otolaryngol. Head Neck Surg.* **18,** 441–446 (2010).

478. Eggermann, E., Bucurenciu, I., Goswami, S. P. & Jonas, P. Nanodomain coupling between Ca^{2+} channels and sensors of exocytosis at fast mammalian synapses. *Nat. Rev. Neurosci.* **13,** 7–21 (2011).

479. Matveev, V., Bertram, R. & Sherman, A. Calcium cooperativity of exocytosis as a measure of Ca^{2}+ channel domain overlap. *Brain Res.* **1398,** 126–138 (2011).

480. Augustine, G. J., Adler, E. M. & Charlton, M. P. The calcium signal for transmitter secretion from presynaptic nerve terminals. *Ann. N. Y. Acad. Sci.* **635,** 365–381 (1991).

481. Weber, A. M. *et al.* N-type Ca2+ channels carry the largest current: implications for nanodomains and transmitter release. *Nat. Neurosci.* **13,** 1348–1350 (2010).

482. Schneckenburger, H. Total internal reflection fluorescence microscopy: technical innovations and novel applications. *Curr. Opin. Biotechnol.* **16,** 13–18 (2005).

483. Persson, F., Barkefors, I. & Elf, J. Single molecule methods with applications in living cells. *Curr. Opin. Biotechnol.* **24,** 737–744 (2013).

484. Cornish, P. V. & Ha, T. A survey of single-molecule techniques in chemical biology. *ACS Chem. Biol.* **2,** 53–61 (2007).

485. Thompson, N. L. & Lagerholm, B. C. Total internal reflection fluorescence: applications in cellular biophysics. *Curr. Opin. Biotechnol.* **8,** 58–64 (1997).

486. Mattheyses, A. L., Simon, S. M. & Rappoport, J. Z. Imaging with total internal reflection fluorescence microscopy for the cell biologist. *J. Cell Sci.* **123,** 3621–3628 (2010).

487. Axelrod, D. Total internal reflection fluorescence microscopy in cell biology. *Traffic Cph. Den.* **2,** 764–774 (2001).

488. Mortensen, K. I., Churchman, L. S., Spudich, J. A. & Flyvbjerg, H. Optimized localization analysis for single-molecule tracking and super-resolution microscopy. *Nat. Methods* **7,** 377–381 (2010).

489. Ritort, F. Single-molecule experiments in biological physics: methods and applications. *J. Phys. Condens. Matter Inst. Phys. J.* **18,** R531-583 (2006).

490. Martin-Fernandez, M. L., Tynan, C. J. & Webb, S. E. D. A ‘pocket guide’ to total internal reflection fluorescence. *J. Microsc.* **252,** 16–22 (2013).

491. Mattheyses, A. L., Shaw, K. & Axelrod, D. Effective elimination of laser interference fringing in fluorescence microscopy by spinning azimuthal incidence angle. *Microsc. Res. Tech.* **69,** 642–647 (2006).

492. Barak, L. S. & Webb, W. W. Diffusion of low density lipoprotein-receptor complex on human fibroblasts. *J. Cell Biol.* **95,** 846–852 (1982).

493. Yildiz, A. *et al.* Myosin V walks hand-over-hand: single fluorophore imaging with 1.5-nm localization. *Science* **300,** 2061–2065 (2003).

494. Okten, Z., Churchman, L. S., Rock, R. S. & Spudich, J. A. Myosin VI walks hand-over-hand along actin. *Nat. Struct. Mol. Biol.* **11,** 884–887 (2004).

495. Axelrod, D., Burghardt, T. P. & Thompson, N. L. Total internal reflection fluorescence. *Annu. Rev. Biophys. Bioeng.* **13,** 247–268 (1984).

496. Sako, Y., Minoghchi, S. & Yanagida, T. Single-molecule imaging of EGFR signalling on the surface of living cells. *Nat. Cell Biol.* **2,** ncb0300_168 (2000).

497. Hellen, E. H. & Axelrod, D. Kinetics of epidermal growth factor/receptor binding on cells measured by total internal reflection/fluorescence recovery after photobleaching. *J. Fluoresc.* **1,** 113–128 (1991).

498. Tokunaga, M., Kitamura, K., Saito, K., Iwane, A. H. & Yanagida, T. Single Molecule Imaging of Fluorophores and Enzymatic Reactions Achieved by Objective-Type Total Internal Reflection Fluorescence Microscopy. *Biochem. Biophys. Res. Commun.* **235,** 47–53 (1997).

499. Huang, Z. & Thompson, N. L. Imaging fluorescence correlation spectroscopy: nonuniform IgE distributions on planar membranes. *Biophys. J.* **70,** 2001–2007 (1996).

500. Wang, M. D. & Axelrod, D. Time-lapse total internal reflection fluorescence video of acetylcholine receptor cluster formation on myotubes. *Dev. Dyn. Off. Publ. Am. Assoc. Anat.* **201,** 29–40 (1994).

501. Sund, S. E. & Axelrod, D. Actin dynamics at the living cell submembrane imaged by total internal reflection fluorescence photobleaching. *Biophys. J.* **79,** 1655–1669 (2000).

502. Omann, G. M. & Axelrod, D. Membrane-proximal calcium transients in stimulated neutrophils detected by total internal reflection fluorescence. *Biophys. J.* **71,** 2885–2891 (1996).

503. Sailer, R. *et al.* Plasma membrane associated location of sulfonated meso-tetraphenylporphyrins of different hydrophilicity probed by total internal reflection fluorescence spectroscopy. *Photochem. Photobiol.* **71,** 460–465 (2000).

504. Jain, A., Liu, R., Xiang, Y. K. & Ha, T. Single-molecule pull-down for studying protein interactions. *Nat. Protoc.* **7,** 445–452 (2012).

505. Haugh, J. M., Codazzi, F., Teruel, M. & Meyer, T. Spatial sensing in fibroblasts mediated by 3' phosphoinositides. *J. Cell Biol.* **151,** 1269–1280 (2000).

506. Dyachok, O., Isakov, Y., Sågetorp, J. & Tengholm, A. Oscillations of cyclic AMP in hormone-stimulated insulin-secreting beta-cells. *Nature* **439,** 349–352 (2006).

507. Luik, R. M., Wu, M. M., Buchanan, J. & Lewis, R. S. The elementary unit of store-operated Ca2+ entry: local activation of CRAC channels by STIM1 at ER-plasma membrane junctions. *J. Cell Biol.* **174,** 815–825 (2006).

508. Rappoport, J. Z. & Simon, S. M. Real-time analysis of clathrin-mediated endocytosis during cell migration. *J. Cell Sci.* **116,** 847–855 (2003).

509. Rappoport, J. Z., Taha, B. W., Lemeer, S., Benmerah, A. & Simon, S. M. The AP-2 complex is excluded from the dynamic population of plasma membrane-associated clathrin. *J. Biol. Chem.* **278,** 47357–47360 (2003).

510. Rappoport, J. Z., Benmerah, A. & Simon, S. M. Analysis of the AP-2 adaptor complex and cargo during clathrin-mediated endocytosis. *Traffic Cph. Den.* **6,** 539–547 (2005).

511. Rappoport, J. Z., Kemal, S., Benmerah, A. & Simon, S. M. Dynamics of clathrin and adaptor proteins during endocytosis. *Am. J. Physiol. Cell Physiol.* **291,** C1072-1081 (2006).

512. Merrifield, C. J., Feldman, M. E., Wan, L. & Almers, W. Imaging actin and dynamin recruitment during invagination of single clathrin-coated pits. *Nat. Cell Biol.* **4,** 691–698 (2002).

513. Schmoranzer, J. & Simon, S. M. Role of microtubules in fusion of post-Golgi vesicles to the plasma membrane. *Mol. Biol. Cell* **14,** 1558–1569 (2003).

514. Lang, T. *et al.* Ca2+-triggered peptide secretion in single cells imaged with green fluorescent protein and evanescent-wave microscopy. *Neuron* **18,** 857–863 (1997).

515. Allersma, M. W., Bittner, M. A., Axelrod, D. & Holz, R. W. Motion matters: secretory granule motion adjacent to the plasma membrane and exocytosis. *Mol. Biol. Cell* **17,** 2424–2438 (2006).

516. Jaiswal, J. K., Fix, M., Takano, T., Nedergaard, M. & Simon, S. M. Resolving vesicle fusion from lysis to monitor calcium-triggered lysosomal exocytosis in astrocytes. *Proc. Natl. Acad. Sci. U. S. A.* **104,** 14151–14156 (2007).

517. Yoon, T.-Y. *et al.* Complexin and Ca2+ stimulate SNARE-mediated membrane fusion. *Nat. Struct. Mol. Biol.* **15,** 707–713 (2008).

518. Lee, H.-K. *et al.* Dynamic Ca2+-dependent stimulation of vesicle fusion by membrane-anchored synaptotagmin 1. *Science* **328,** 760–763 (2010).

519. Lai, Y. *et al.* Fusion pore formation and expansion induced by Ca2+ and synaptotagmin 1. *Proc. Natl. Acad. Sci. U. S. A.* **110,** 1333–1338 (2013).

520. Lou, X., Shin, J., Yang, Y., Kim, J. & Shin, Y.-K. Synaptotagmin-1 is an antagonist for Munc18-1 in SNARE zippering. *J. Biol. Chem.* **290,** 10535–10543 (2015).

521. Lou, X. & Shin, Y.-K. SNARE zippering. *Biosci. Rep.* **36,** (2016).

522. Demuro, A. & Parker, I. Imaging the activity and localization of single voltage-gated Ca(2+) channels by total internal reflection fluorescence microscopy. *Biophys. J.* **86,** 3250–3259 (2004).

523. Krylyshkina, O. *et al.* Nanometer targeting of microtubules to focal adhesions. *J. Cell Biol.* **161,** 853–859 (2003).

524. Kaksonen, M., Toret, C. P. & Drubin, D. G. A modular design for the clathrin- and actin-mediated endocytosis machinery. *Cell* **123,** 305–320 (2005).

525. Kuhn, J. R. & Pollard, T. D. Real-time measurements of actin filament polymerization by total internal reflection fluorescence microscopy. *Biophys. J.* **88,** 1387–1402 (2005).

526. Lieto, A. M., Cush, R. C. & Thompson, N. L. Ligand-Receptor Kinetics Measured by Total Internal Reflection with Fluorescence Correlation Spectroscopy. *Biophys. J.* **85,** 3294–3302 (2003).

527. Tanimoto, S. & Kitano, H. Binding kinetics of antibody to hapten-doped lipid monolayers as studied by multiple internal reflection fluorescence method. *Colloids Surf. B Biointerfaces* **4,** 259–265 (1995).

528. Hsieh, H. V. & Thompson, N. L. Dissociation kinetics between a mouse Fc receptor (Fc gamma RII) and IgG: measurement by total internal reflection with fluorescence photobleaching recovery. *Biochemistry (Mosc.)* **34,** 12481–12488 (1995).

529. Pfaff, M. *et al.* Selective recognition of cyclic RGD peptides of NMR defined conformation by alpha IIb beta 3, alpha V beta 3, and alpha 5 beta 1 integrins. *J. Biol. Chem.* **269,** 20233–20238 (1994).

530. Stout, A. L. & Axelrod, D. Reversible binding kinetics of a cytoskeletal protein at the erythrocyte submembrane. *Biophys. J.* **67,** 1324–1334 (1994).

531. Hinterdorfer, P., Baber, G. & Tamm, L. K. Reconstitution of membrane fusion sites. A total internal reflection fluorescence microscopy study of influenza hemagglutinin-mediated membrane fusion. *J. Biol. Chem.* **269,** 20360–20368 (1994).

532. Kelm, R. J., Swords, N. A., Orfeo, T. & Mann, K. G. Osteonectin in matrix remodeling. A plasminogen-osteonectin-collagen complex. *J. Biol. Chem.* **269,** 30147–30153 (1994).

533. Riven, I., Kalmanzon, E., Segev, L. & Reuveny, E. Conformational rearrangements associated with the gating of the G protein-coupled potassium channel revealed by FRET microscopy. *Neuron* **38,** 225–235 (2003).

534. Lipman, E. A., Schuler, B., Bakajin, O. & Eaton, W. A. Single-Molecule Measurement of Protein Folding Kinetics. *Science* **301,** 1233–1235 (2003).

535. Schuler, B., Lipman, E. A. & Eaton, W. A. Probing the free-energy surface for protein folding with single-molecule fluorescence spectroscopy. *Nature* **419,** 743–747 (2002).

536. Hoffmann, A. *et al.* Quantifying heterogeneity and conformational dynamics from single molecule FRET of diffusing molecules: recurrence analysis of single particles (RASP). *Phys. Chem. Chem. Phys. PCCP* **13,** 1857–1871 (2011).

537. Chung, H. S. *et al.* Extracting rate coefficients from single-molecule photon trajectories and FRET efficiency histograms for a fast-folding protein. *J. Phys. Chem. A* **115,** 3642–3656 (2011).

538. Gopich, I. V. & Szabo, A. FRET efficiency distributions of multistate single molecules. *J. Phys. Chem. B* **114,** 15221–15226 (2010).

539. Götz, M., Wortmann, P., Schmid, S. & Hugel, T. A Multicolor Single-Molecule FRET Approach to Study Protein Dynamics and Interactions Simultaneously. *Methods Enzymol.* **581,** 487–516 (2016).

540. Teramura, Y. *et al.* Single-molecule analysis of epidermal growth factor binding on the surface of living cells. *EMBO J.* **25,** 4215–4222 (2006).

541. Kasai, R. S. *et al.* Full characterization of GPCR monomer-dimer dynamic equilibrium by single molecule imaging. *J. Cell Biol.* **192,** 463–480 (2011).

542. Hern, J. A. *et al.* Formation and dissociation of M1 muscarinic receptor dimers seen by total internal reflection fluorescence imaging of single molecules. *Proc. Natl. Acad. Sci. U. S. A.* **107,** 2693–2698 (2010).

543. Park, H. Y. *et al.* Visualization of dynamics of single endogenous mRNA labeled in live mouse. *Science* **343,** 422–424 (2014).

544. Suzuki, K. G. N. *et al.* Transient GPI-anchored protein homodimers are units for raft organization and function. *Nat. Chem. Biol.* **8,** 774–783 (2012).

545. Trabesinger, W., Schütz, G. J., Gruber, H. J., Schindler, H. & Schmidt, T. Detection of individual oligonucleotide pairing by single-molecule microscopy. *Anal. Chem.* **71,** 279–283 (1999).

546. Yamamura, H., Ikeda, C., Suzuki, Y., Ohya, S. & Imaizumi, Y. Molecular assembly and dynamics of fluorescent protein-tagged single KCa1.1 channel in expression system and vascular smooth muscle cells. *Am. J. Physiol. Cell Physiol.* **302,** C1257-1268 (2012).

547. Schindl, R. *et al.* The first ankyrin-like repeat is the minimum indispensable key structure for functional assembly of homo- and heteromeric TRPC4/TRPC5 channels. *Cell Calcium* **43,** 260–269 (2008).

548. Staruschenko, A., Jeske, N. A. & Akopian, A. N. Contribution of TRPV1-TRPA1 interaction to the single channel properties of the TRPA1 channel. *J. Biol. Chem.* **285,** 15167–15177 (2010).

549. Suzuki, Y., Yamamura, H., Ohya, S. & Imaizumi, Y. Caveolin-1 facilitates the direct coupling between large conductance Ca2+-activated K+ (BKCa) and Cav1.2 Ca2+ channels and their clustering to regulate membrane excitability in vascular myocytes. *J. Biol. Chem.* **288,** 36750–36761 (2013).

550. Riven, I., Iwanir, S. & Reuveny, E. GIRK Channel Activation Involves a Local Rearrangement of a Preformed G Protein Channel Complex. *Neuron* **51,** 561–573 (2006).

551. Fowler, C. E., Aryal, P., Suen, K. F. & Slesinger, P. A. Evidence for association of GABA(B) receptors with Kir3 channels and regulators of G protein signalling (RGS4) proteins. *J. Physiol.* **580,** 51–65 (2007).

552. Bal, M., Zaika, O., Martin, P. & Shapiro, M. S. Calmodulin binding to M-type K+ channels assayed by TIRF/FRET in living cells. *J. Physiol.* **586,** 2307–2320 (2008).

553. Bal, M., Zhang, J., Hernandez, C. C., Zaika, O. & Shapiro, M. S. Ca2+/calmodulin disrupts AKAP79/150 interactions with KCNQ (M-Type) K+ channels. *J. Neurosci. Off. J. Soc. Neurosci.* **30,** 2311–2323 (2010).

554. Kobrinsky, E. *et al.* Effect of Cavβ Subunits on Structural Organization of Cav1.2 Calcium Channels. *PLOS ONE* **4,** e5587 (2009).

555. Xie, L. *et al.* RalA GTPase tethers insulin granules to L- and R-type calcium channels through binding α2 δ-1 subunit. *Traffic Cph. Den.* **14,** 428–439 (2013).

556. Kasai, R. S. & Kusumi, A. Single-molecule imaging revealed dynamic GPCR dimerization. *Curr. Opin. Cell Biol.* **27,** 78–86 (2014).

557. Gebhardt, J. C. M. *et al.* Single-molecule imaging of transcription factor binding to DNA in live mammalian cells. *Nat. Methods* **10,** 421–426 (2013).

558. Nagata, K. O., Nakada, C., Kasai, R. S., Kusumi, A. & Ueda, K. ABCA1 dimer-monomer interconversion during HDL generation revealed by single-molecule imaging. *Proc. Natl. Acad. Sci. U. S. A.* **110,** 5034–5039 (2013).

559. Suzuki, K. G. N. *et al.* GPI-anchored receptor clusters transiently recruit Lyn and G alpha for temporary cluster immobilization and Lyn activation: single-molecule tracking study 1. *J. Cell Biol.* **177,** 717–730 (2007).

560. Low-Nam, S. T. *et al.* ErbB1 dimerization is promoted by domain co-confinement and stabilized by ligand binding. *Nat. Struct. Mol. Biol.* **18,** 1244–1249 (2011).

561. Veliz, L. A. *et al.* Near-membrane dynamics and capture of TRPM8 channels within transient confinement domains. *PloS One* **5,** e13290 (2010).

562. Ulbrich, M. H. & Isacoff, E. Y. Subunit counting in membrane-bound proteins. *Nat. Methods* **4,** 319–321 (2007).

563. Kim, E. Y. *et al.* Multiple C-terminal tail Ca(2+)/CaMs regulate Ca(V)1.2 function but do not mediate channel dimerization. *EMBO J.* **29,** 3924–3938 (2010).

564. Nakajo, K., Ulbrich, M. H., Kubo, Y. & Isacoff, E. Y. Stoichiometry of the KCNQ1 - KCNE1 ion channel complex. *Proc. Natl. Acad. Sci. U. S. A.* **107,** 18862–18867 (2010).

565. Penna, A. *et al.* The CRAC channel consists of a tetramer formed by Stim-induced dimerization of Orai dimers. *Nature* **456,** 116–120 (2008).

566. Bartoi, T., Augustinowski, K., Polleichtner, G., Gründer, S. & Ulbrich, M. H. Acid-sensing ion channel (ASIC) 1a/2a heteromers have a flexible 2:1/1:2 stoichiometry. *Proc. Natl. Acad. Sci. U. S. A.* **111,** 8281–8286 (2014).

567. Yu, Y. *et al.* Molecular mechanism of the assembly of an acid-sensing receptor ion channel complex. *Nat. Commun.* **3,** 1252 (2012).

568. Bharill, S., Fu, Z., Palty, R. & Isacoff, E. Y. Stoichiometry and specific assembly of Best ion channels. *Proc. Natl. Acad. Sci. U. S. A.* **111,** 6491–6496 (2014).

569. Durisic, N. *et al.* Stoichiometry of the human glycine receptor revealed by direct subunit counting. *J. Neurosci. Off. J. Soc. Neurosci.* **32,** 12915–12920 (2012).

570. Tombola, F., Ulbrich, M. H. & Isacoff, E. Y. The Voltage-Gated Proton Channel Hv1 Has Two Pores, Each Controlled by One Voltage Sensor. *Neuron* **58,** 546–556 (2008).

571. Demuro, A. *et al.* Subunit stoichiometry of human Orai1 and Orai3 channels in closed and open states. *Proc. Natl. Acad. Sci. U. S. A.* **108,** 17832–17837 (2011).

572. Ji, W. *et al.* Functional stoichiometry of the unitary calcium-release-activated calcium channel. *Proc. Natl. Acad. Sci. U. S. A.* **105,** 13668–13673 (2008).

573. Haggie, P. M. & Verkman, A. S. Monomeric CFTR in plasma membranes in live cells revealed by single molecule fluorescence imaging. *J. Biol. Chem.* **283,** 23510–23513 (2008).

574. Bankston, J. R. *et al.* Structure and stoichiometry of an accessory subunit TRIP8b interaction with hyperpolarization-activated cyclic nucleotide-gated channels. *Proc. Natl. Acad. Sci. U. S. A.* **109,** 7899–7904 (2012).

575. Yu, Y. *et al.* Structural and molecular basis of the assembly of the TRPP2/PKD1 complex. *Proc. Natl. Acad. Sci. U. S. A.* **106,** 11558–11563 (2009).

576. Jing, Z. *et al.* Disruption of the presynaptic cytomatrix protein bassoon degrades ribbon anchorage, multiquantal release, and sound encoding at the hair cell afferent synapse. *J. Neurosci. Off. J. Soc. Neurosci.* **33,** 4456–4467 (2013).

577. Vincent, P. F. Y., Bouleau, Y., Safieddine, S., Petit, C. & Dulon, D. Exocytotic machineries of vestibular type I and cochlear ribbon synapses display similar intrinsic

otoferlin-dependent Ca2+ sensitivity but a different coupling to Ca2+ channels. *J. Neurosci. Off. J. Soc. Neurosci.* **34,** 10853–10869 (2014).

578. Vincent, P. F., Bouleau, Y., Petit, C. & Dulon, D. A synaptic F-actin network controls otoferlin-dependent exocytosis in auditory inner hair cells. *eLife* **4,** (2015).

579. Jain, A. *et al.* Probing cellular protein complexes using single-molecule pull-down. *Nature* **473,** 484–488 (2011).

580. Adler, J. & Parmryd, I. Quantifying colocalization by correlation: the Pearson correlation coefficient is superior to the Mander's overlap coefficient. *Cytom. Part J. Int. Soc. Anal. Cytol.* **77,** 733–742 (2010).

581. Chapman, E. R. How does synaptotagmin trigger neurotransmitter release? *Annu. Rev. Biochem.* **77,** 615–641 (2008).

582. Gordon, M. P., Ha, T. & Selvin, P. R. Single-molecule high-resolution imaging with photobleaching. *Proc. Natl. Acad. Sci. U. S. A.* **101,** 6462–6465 (2004).

583. Hines, K. E. Inferring subunit stoichiometry from single molecule photobleaching. *J. Gen. Physiol.* **141,** 737–746 (2013).

584. Zhou, A., Brewer, K. D. & Rizo, J. Analysis of SNARE complex/synaptotagmin-1 interactions by one-dimensional NMR spectroscopy. *Biochemistry (Mosc.)* **52,** 3446–3456 (2013).

585. Choi, B. Y. *et al.* Identities and frequencies of mutations of the otoferlin gene (OTOF) causing DFNB9 deafness in Pakistan. *Clin. Genet.* **75,** 237–243 (2009).

586. Hammill, J. T., Miyake-Stoner, S., Hazen, J. L., Jackson, J. C. & Mehl, R. A. Preparation of site-specifically labeled fluorinated proteins for 19F-NMR structural characterization. *Nat. Protoc.* **2,** 2601–2607 (2007).

587. Speight, L. C. *et al.* Efficient synthesis and in vivo incorporation of acridon-2-ylalanine, a fluorescent amino acid for lifetime and Förster resonance energy transfer/luminescence resonance energy transfer studies. *J. Am. Chem. Soc.* **135,** 18806–18814 (2013).

588. Hams, N., Padmanarayana, M., Qiu, W. & Johnson, C. P. Otoferlin is a multivalent calcium-sensitive scaffold linking SNAREs and calcium channels. *Proc. Natl. Acad. Sci.* **114,** 8023–8028 (2017).

589. Landgraf, K. E., Malmberg, N. J. & Falke, J. J. Effect of PIP2 Binding on the Membrane Docking Geometry of PKCα C2 Domain: An EPR Site-Directed Spin-Labeling and Relaxation Study. *Biochemistry (Mosc.)* **47,** 8301–8316 (2008).

590. Bittova, L., Sumandea, M. & Cho, W. A structure-function study of the C2 domain of cytosolic phospholipase A2. Identification of essential calcium ligands and hydrophobic membrane binding residues. *J. Biol. Chem.* **274,** 9665–9672 (1999).

591. Abrams, F. S., Chattopadhyay, A. & London, E. Determination of the location of fluorescent probes attached to fatty acids using parallax analysis of fluorescence quenching: effect of carboxyl ionization state and environment on depth. *Biochemistry (Mosc.)* **31,** 5322–5327 (1992).

592. Bai, H. *et al.* Different states of synaptotagmin regulate evoked versus spontaneous release. *Nat. Commun.* **7,** 10971 (2016).

593. Redpath, G. M. I. *et al.* Calpain cleavage within dysferlin exon 40a releases a synaptotagmin-like module for membrane repair. *Mol. Biol. Cell* **25,** 3037–3048 (2014).

594. Godell, C. M. *et al.* Calpain activity promotes the sealing of severed giant axons. *Proc. Natl. Acad. Sci. U. S. A.* **94,** 4751–4756 (1997).

595. Mellgren, R. L. *et al.* Calcium-dependent plasma membrane repair requires m- or mu-calpain, but not calpain-3, the proteasome, or caspases. *Biochim. Biophys. Acta* **1793,** 1886–1893 (2009).

596. Shearer, A. E. & Smith, R. J. OTOF-Related Deafness. in *GeneReviews®* (eds. Adam, M. P. et al.) (University of Washington, Seattle, 1993).

597. Reference, G. H. OTOF gene. *Genetics Home Reference* Available at: https://ghr.nlm.nih.gov/gene/OTOF. (Accessed: 7th January 2018)

Appendix

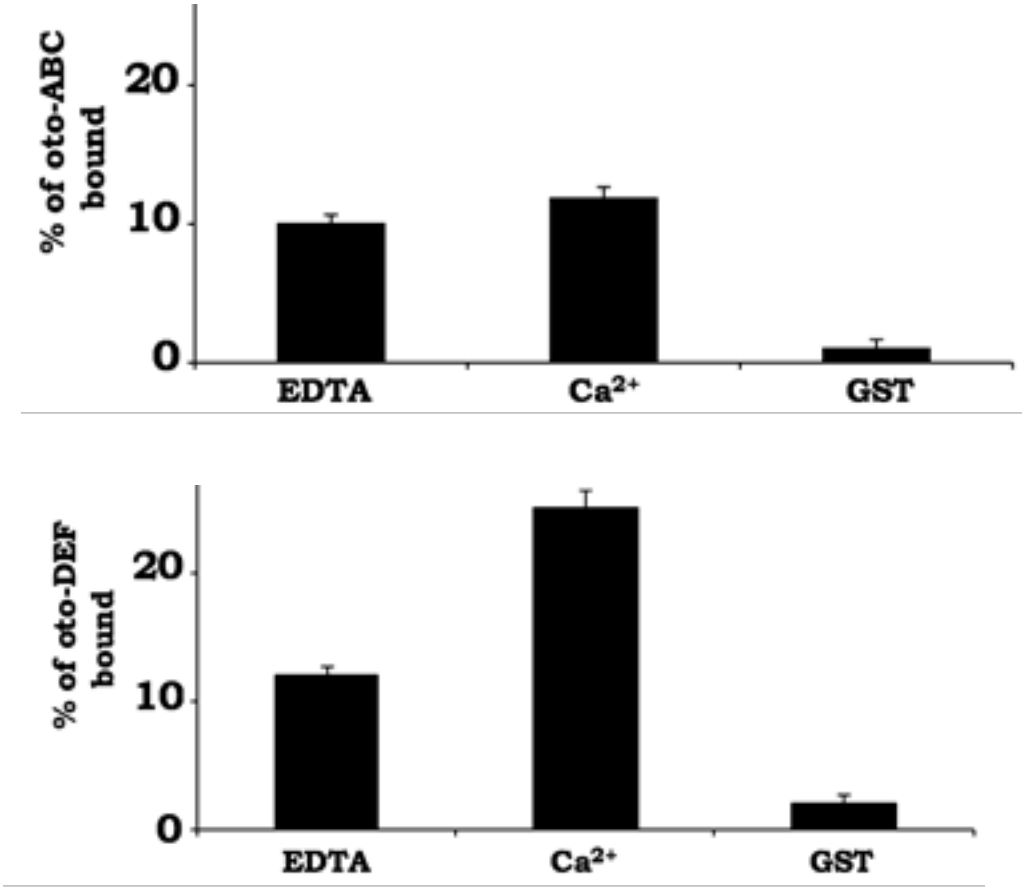

Supplemental Figure 2.1: Loop1.3 GST-pulldowns
Loop1.3 interacts with regions of the N and C termini of otoferlin. Bead-immobilized GST-Loop1.3 cosedimented with recombinant forms of otoferlin composed of the first three C2 domains (C2ABC; Upper) or the last three domains (C2DEF; Lower). Bead-immobilized GST served as a control. Results represent the mean of three sample preparations (n = 3). Error = SEM.

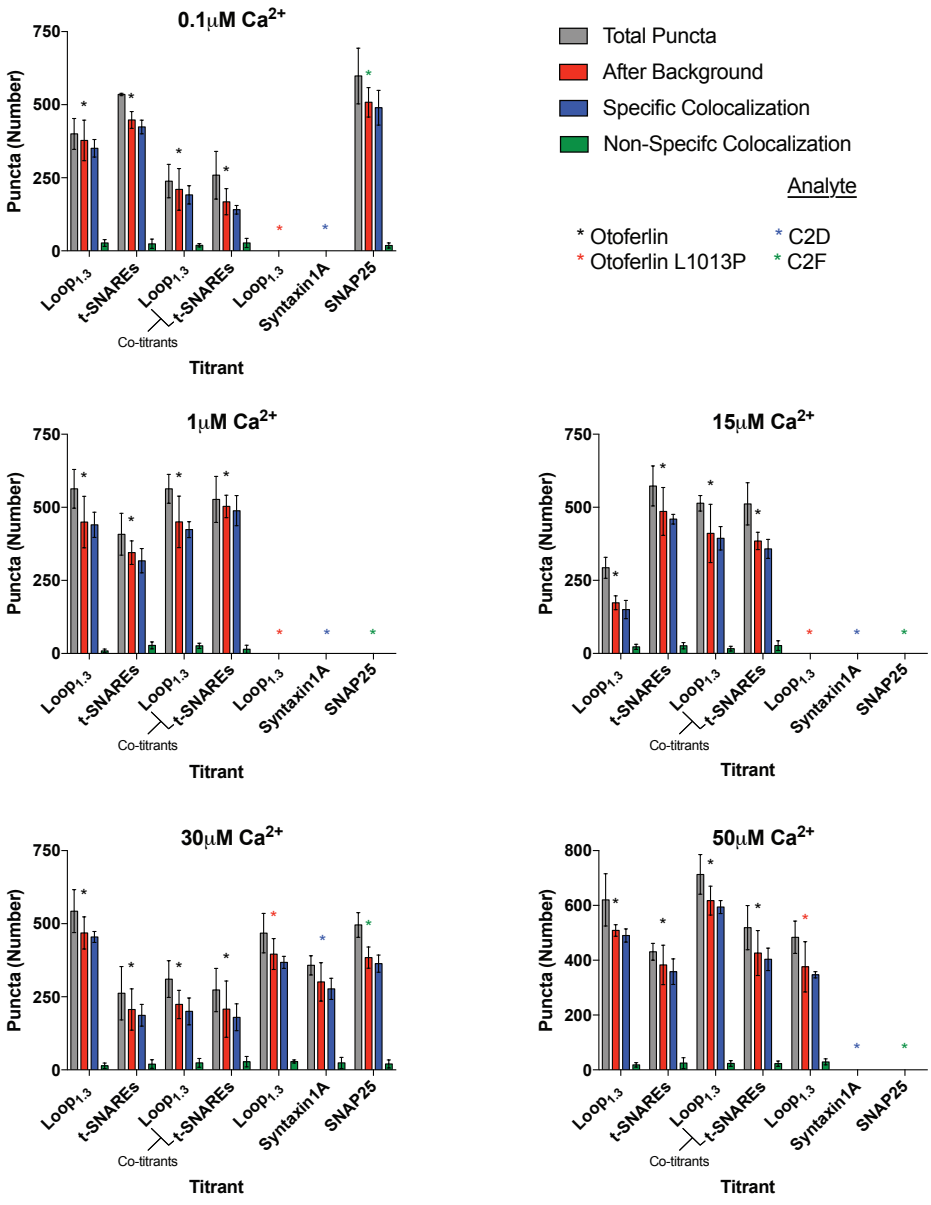

Supplemental Figure 2.2: Number of colocalized and noncolocalized titrant puncta Gray and red bars represent the numbers of puncta before and after background subtraction, respectively. Blue bars represent specific colocalized puncta after background subtraction, and green bars represent the number of Loop1.3 or t-SNARE puncta that do not colocalize with the immobilized YFP-tagged protein after background subtraction. Cotitrants represent puncta numbers from results shown in Fig. 7. Data represent mean and SEM from three separate coverslip samples (n = 3).

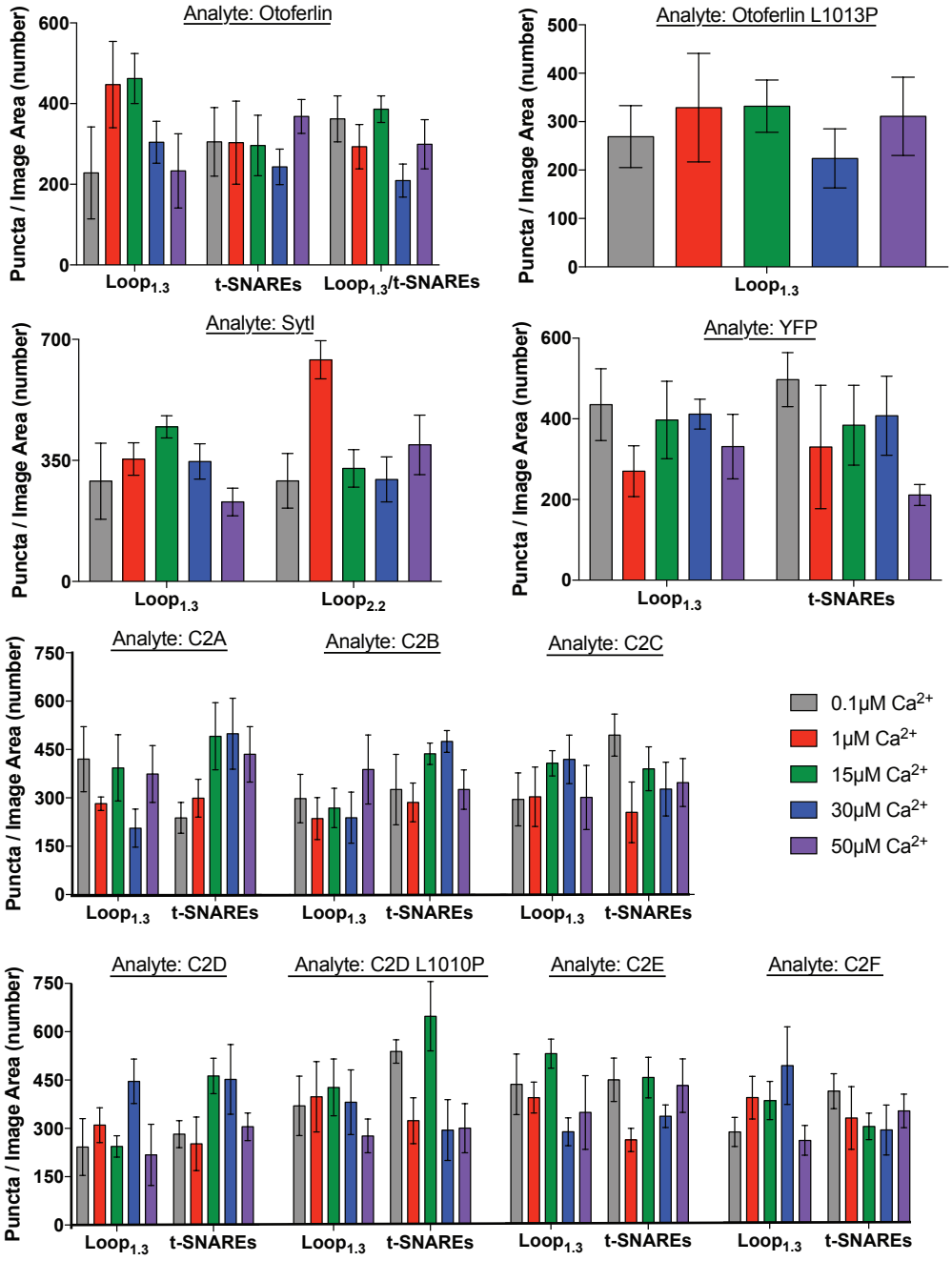

Supplemental Figure 2.3: Mean number of colocalized puncta per viewing area
Error represents SEM from three separate coverslip samples (n = 3).

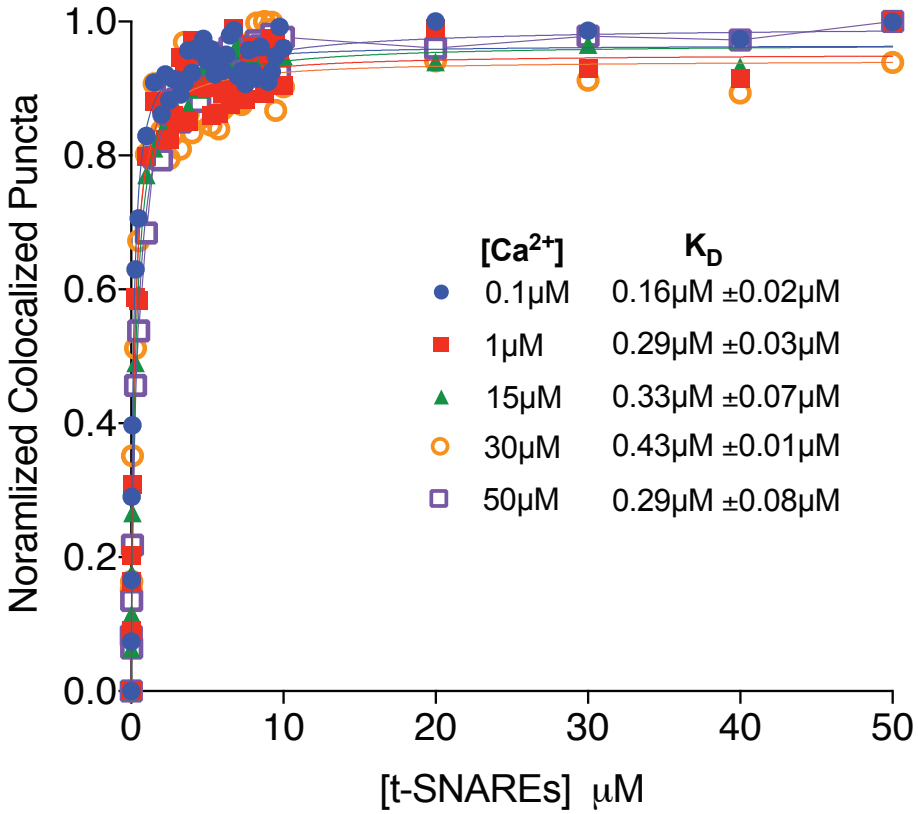

Supplemental Figure 2.4: Syt-I smCoBRA curve with t-SNAREs
Binding curves for immobilized synaptotagmin I titrated with t-SNARE dimer at indicated calcium concentration. Each experimental data point represents the mean value of n = 3 sample preparations.

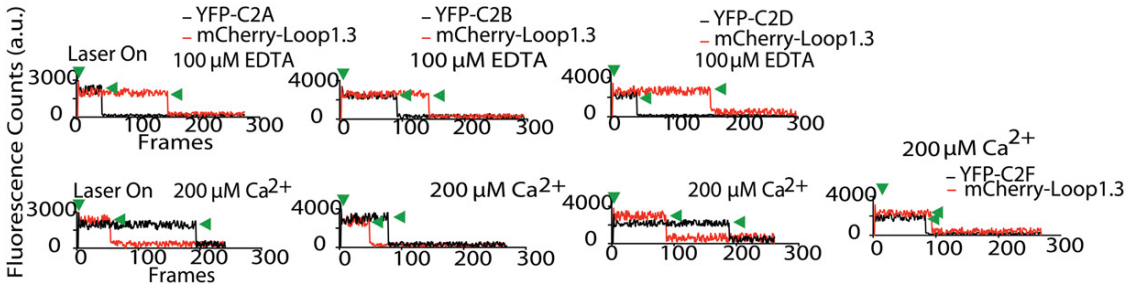

Supplemental Figure 2.5: Otoferlin C2 domain single-molecule photobleaching with Loop1.3

Representative single-molecule photobleaching traces for Loop1.3 bound to YFP-otoferlin C2A, C2B, C2D, and C2F domains in the presence of 100µM EDTA (Top) or 200µM free calcium (Bottom).

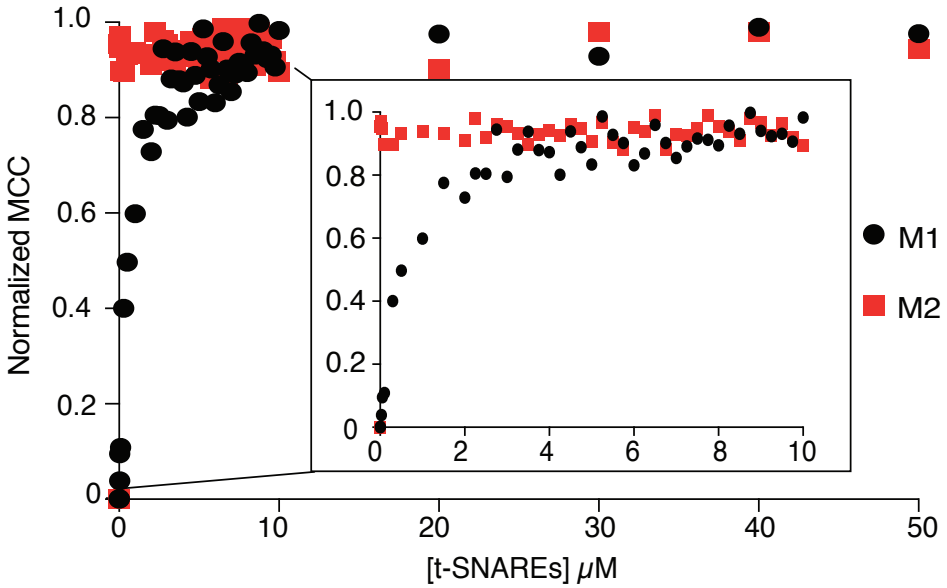

Supplemental Figure 2.6: Manders plot for otoferlin/tSNARE interactions with Loop1.3
Mander's colocalization coefficients associated with Fig. 2.6. M1 (black) represents the fraction of analyte prebound complex (otoferlin with t-SNARE dimer) colocalized with the titrant (Loop1.3). Colocalization coefficient M2 (red) represents the fraction of Loop1.3 titrant colocalized with the analyte prebound complex. Results depicted are in the presence of 1 μM calcium. Normalized MCC refers to the normalized Mander's correlation coefficient. Inset depicts 0–10μM for clarity.

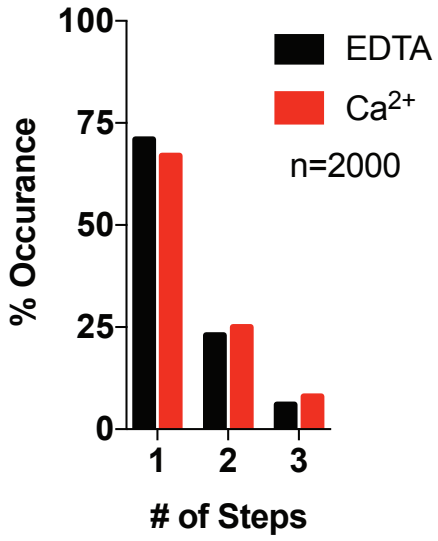

Supplemental Figure 2.7: smPhotobleaching distribution for tSNAREs and otoferlin L1010P mutant

Single-molecule photobleaching distribution for t-SNAREs–mCherry bound to YFP-otoferlinL1010P in the presence of 100 μM EDTA and 200 μM free calcium.

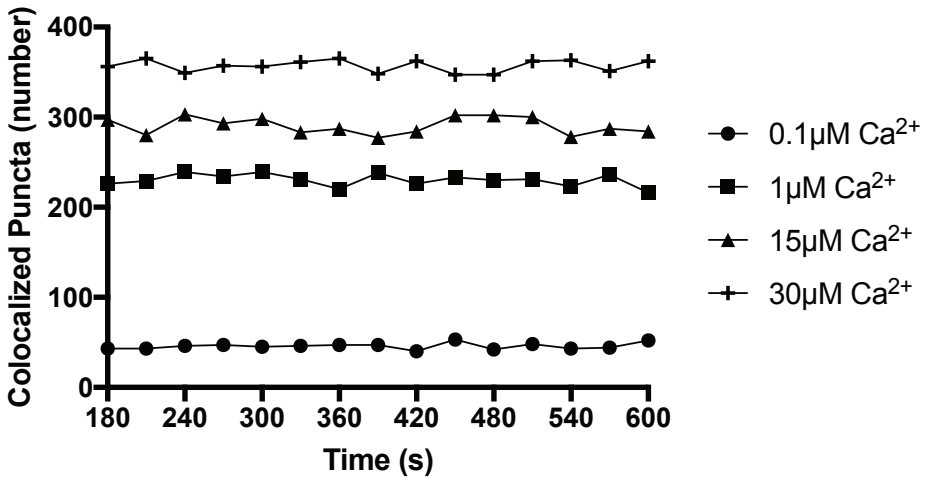

Supplemental Figure 2.8: Binding time course measurements
Time course measurement of C2D-YFP bound to Loop1.3 in the presence of calcium. Changes in colocalization were measured every 30 seconds for 10 minutes starting at 3 minutes.

PC

	PS-PC; Ca^{2+}		PS-PC; EDTA		PS-PC-PI(4,5)P_2; Ca^{2+}		PS-PC-PI(4,5)P_2; EDTA	
	Mean ± Std Dev	R^2 of fit	Mean ± Std Dev	R^2 of fit	Mean ± Std Dev	R^2 of fit	Mean ± Std Dev	R^2 of fit
C2F	11481 ±2400	0.974	11479 ±2428	0.966	51613 ±2034	0.876	51175 ±2113	0.935
C2EF	11470 ±2204	0.984	10393 ±1952	0.981	39316 ±2087	0.977	9466 ±2162	0.950
C2DEF	9408 ±2254	0.985	10230 ±2020	0.990	44763 ±3294	0.865	8884 ±2059	0.987
C2A-F	10048 ±2426	0.991	9896 ±2433	0.982	48528 ±1265	0.989	9862 ±2363	0.980

PC-Doxyl-5

	PS-PC; Ca^{2+}		PS-PC; EDTA		PS-PC-PI(4,5)P_2; Ca^{2+}		PS-PC-PI(4,5)P_2; EDTA	
	Mean ± Std Dev	R^2 of fit	Mean ± Std Dev	R^2 of fit	Mean ± Std Dev	R^2 of fit	Mean ± Std Dev	R^2 of fit
C2F	10919 ±2188	0.995	11902 ±2626	0.958	41884 ±2250	0.984	42335 ±2196	0.969
C2EF	11275 ±2141	0.991	10359 ±2005	0.993	38208 ±2183	0.961	9717 ±2484	0.993
C2DEF	8765 ±2389	0.980	9897 ±2339	0.982	46460 ±1228	0.998	9944 ±2059	0.983
C2A-F	9969 ±2401	0.986	9500 ±2527	0.961	47509 ±1267	0.997	10396 ±2325	0.992

PC-Doxyl-12

	PS-PC; Ca^{2+}		PS-PC; EDTA		PS-PC-PI(4,5)P_2; Ca^{2+}		PS-PC-PI(4,5)P_2; EDTA	
	Mean ± Std Dev	R^2 of fit	Mean ± Std Dev	R^2 of fit	Mean ± Std Dev	R^2 of fit	Mean ± Std Dev	R^2 of fit
C2F	12553 ±2017	0.990	12468 ±2590	0.958	25246 ±2385	0.905	26685 ±2101	0.980
C2EF	10624 ±2275	0.972	7616 ±1587	0.980	24001 ±2518	0.913	11358 ±1854	0.987
C2DEF	9225 ±2053	0.991	10221 ±2181	0.985	21531 ±1252	0.997	9215 ±2342	0.986
C2A-F	10008 ±2398	0.983	10459 ±2111	0.973	18975 ±1531	0.993	10391 ±2072	0.987

Supplemental Table 3.1